High Harmonic Generation from Transiently Aligned Molecules in a Hollow-core Waveguide

A Dissertation
Presented to
the faculty of the School of Engineering and Applied Science
University of Virginia

In Partial Fulfillment
of the requirements for the Degree
Doctor of Philosophy Engineering Physics

by

Brett Allen Sickmiller

B.A., Whittier College, 2002

December 2008

Abstract

A coherent VUV source, based on optical high harmonic generation (HHG) of intense ultrashort laser pulses in atomic and molecular gases, has been developed at the University of Virginia. Experiments performed with this source have focused on using emission to better understand molecular dynamics in intense laser fields and on exploiting these dynamics to enhance the harmonic emission.

HHG is the process in which coherent vacuum ultraviolet radiation is produced by focusing intense, short laser pulses into a gas medium. The source developed as part of this dissertation research utilizes a hollow-core waveguide to increase the VUV yield and enable better control over its macroscopic coherence properties. The new source was used for several atomic and molecular physics experiments.

First, molecular alignment-dependent harmonic yields from CO and N_2 were measured at room temperature. These are the first reported measurements of harmonics generated in transiently aligned molecules in a hollow-core waveguide. From these alignment signals, a functional form for the HHG angular dependence was determined by fitting the data to simulated alignment parameters. In particular, the contrast ratio of the harmonic yield from molecules perfectly aligned parallel vs. perpendicular to the generating laser polarization was extracted. The ellipticity dependence of the harmonic yield was measured for different molecular alignments in N_2. This allowed us to eliminate returning electron flux as an important variable in the HHG yield measurements from aligned molecules. In a second line of experiments, the effect of molecular alignment on the macroscopic propagation properties of the medium was examined. First at higher harmonic orders, a reversal in the time-dependent variation in the HHG yield was observed. Previously, this reversal was explained in terms of the single atom response. However, simulations indicate that this reversal is due to the increased ionization from aligned molecules which affects the phase matching properties of the medium and shifts the optimum phase matched pressure to higher values. This result illustrates that both the single molecule response

and the macroscopic propagation properties of the medium contribute to the alignment-dependent variation in the HHG yield. As a technical improvement, a liquid nitrogen cooled fiber was constructed to reduce the gas temperature from 300 K to 150 K and improve the degree of alignment in the fiber. The third and final group of experiments focused on the use of quasi-phase matching (QPM) techniques to enhance the overall harmonic output. Counter-propagating (CP) control and signal pulses were utilized in a QPM scheme. First, long ($\tau > 1.6$ ps) CP pulses were used to probe the macroscopic non-linear-optical properties of gaseous media. Then, short ($\tau \sim 100$ fs) control pulses were used to transiently align diatomic molecules inside the waveguide, spatially mapping the periodic temporal revival structure and, thus, modulating the properties of the molecular target gas throughout the fiber. Unfortunately, this modulation resulted in only a small increase in the HHG yield. Simulations indicate that this small enhancement is due to the weak time-independent alignment produced by the short, CP pulse.

Contents

List of Figures

List of Tables

List of Symbols

Greek

α = absorption coefficient (m^{-1})

$\bar{\alpha}$ = polarizability tensor

$\alpha_{\parallel}$ = polarizability parallel to molecular axis

$\alpha_{\perp}$ = polarizability perpendicular to molecular axis

β = weighted difference

Γ = gas density (atoms/m^3)

γ = shape factor for capillary

$\Delta\alpha$ = polarizability anisotropy

$\Delta\delta$ = neutral gas dispersion

Δk = phase mis-match (dispersion) (cm^{-1})

ΔR = change in internuclear separation (m)

Δw = width of SHG profile (m)

$\Delta\tau_a$ = width of autocorrelation function (sec)

ϵ = ellipticity

η = ionization fraction

η_{cr} = critical ionization fraction

θ = angle between laser polarization and principle molecular axis

Θ = relative phase

λ = wavelength (m)

Λ = modulation period (m)

ρ = gas density (mass/m^3)

σ = ionization cross section (cm^2/g)

τ = pulse(time) duration

$\vec{\tau}$ = torque

ϕ = phase modulation

χ_{eff} = effective nonlinear coefficient

Ψ = wavefunction

ψ = angle

ω = frequency

Roman

a = waveguide radius (μm)
B_0 = rotational constant (cm^{-1})
$\vec{d}$ = dipole moment
c = speed of light
d = grating function
D_q = phase difference
E = field amplitude
E_J = rotational energy
F_q = complex constant
$\hbar$ = reduced Planck's constant
I = field intensity (W/cm^2)
I_p = ionization potential
I_q = intensity of qth order harmonic
J = rotational quantum number
k = wavenumber
k = elastic force constant
L = length (m)
L_{abs} = absorption length (m)
L_c = coherence length (m)
L_{med} = medium length (m)
m_r = reduced mass (g)
n = index of refraction
N = number of atoms/molecules
N_a = number of radiating dipoles
N_{atm} = number density at 1 atm
P = pressure (torr)
P_{2N}(x) = Legendre Polynomials
r_e = classical electron radius (m)
R = universal gas constant
R = grating radius
R_{eq} = equilibrium internuclear distance (m)
q = harmonic order
T = temperature (K)
v_g = group velocity
u_{11} = first zero of the Bessel function J_0
U_p = pondermotive energy
X = counter reading

Acknowledgments

I have been blessed to have the aid and support of so many during my educational journey. First and foremost, I would like to thank my Mommas. She has been the rock throughout my life and I would not be the man I am today without her love and encouragement. To my Dad, thank you for always believing in me and inspiring me to achieve all that I can. To Greg and Piper, thank you for being a source of support throughout my formative years. Cory and Kendall, I wish you all the best as you both pursue your own paths. I must also thank my grandparents: Rudy, Mary Anne, Eileen, and Donavon (posthumously). Your love gives me strength no matter what life throws at me.

To love of my life, Nicole, thank you for standing beside me for these last nine years. You listened to me when I was frustrated and were there to celebrate my successes. Your smile lights up any room you are in and brightens even my worst day. I look forward continuing to build our lives together. I would not be where I am today without you next to me; this was a team effort.

My time at the University of Virginia was made easier due to the hard work and dedication of the staff of both the Physics and Materials Science Departments. Thank you, Chris, Gwen, Pat, Beverly and Faye for aiding in all my lab purchases and accounting needs. A special thanks goes out to Suzie, Tammie, Dawn, Beth, and Vickie. If not for the work of these fine people, this mutt would have been lost. I could not have navigated the bureaucracy of EP program without all of you.

Thanks to Eric for showing me the ropes and assisting me as I began my research. Russell, thank you for the insightful discussions about physics and the World Cup. Thank you, Kelsie, for helping me get through my last year here and for your help editing this dissertation. Good luck in your research.

Dan, congratulations on both your graduation and your nuptial. You were always there when I had a question, needed a hand, or just needed someone to talk to. I wish you and Alden all the best.

This work could not have been accomplished without Dr. Robert Jones, who not only served as my supervisor but also encouraged and challenged me throughout my academic program. Thank for all of your patience when I sometimes did not see the big picture. I hope my work will prove useful to you in your future endeavors.

Chapter 1

Introduction

1.1   Motivation

Ultrafast laser technology enables the generation of laser pulses with extremely short durations on the order of a few femtoseconds, that can produce fields with intensities well above 10^{18} W/cm^2. With these short, intense fields the non-perturbative regime of light-matter interactions can be explored. At intensities $> 10^{14}$ W/cm^2, the electric field becomes comparable to the binding energy of electrons. The atom can thus be easily ionized, and the freed electron is subject to interactions with the oscillating laser field. The electron can gain kinetic energy from the field, and its energy can be several times larger than its original binding energy. High harmonic generation (HHG) is one consequence of the atom/field interaction [1]. In HHG, the free electron recombines with its parent ion, releasing its large kinetic energy as a single high energy photon. HHG produces radiation, from the ultraviolet to soft X-ray regime (photon engeries up to ~ 950 eV), that has both temporal and spatial coherence. The HHG conversion efficiency is usually low and only 10^{-10} to 10^{-5} of the laser energy is transferred into each harmonic order.

1

Even so, the HHG process and radiation can enable various fundamental and practical applications such as attosecond pulse production [2], x-ray holography [3], and probing molecular dynamics [4, 5]. The output HHG flux is a combination of the single atom response and its macroscopic propagation through the medium. When the HHG process is phase-matched, the harmonic energy scales as N^2 rather than N for a larger number, N, of emitters.

A significant portion of HHG research focuses on increasing harmonic production in macroscopic media via phase matching or quasi-phase matching. At intensities where there is negligible ionization, the production of lower order harmonics (< 90 eV) can be phase matched inside a hollow-core fiber waveguide via pressure-tuning [6, 7]. The generation of higher order harmonics requires higher intensities where significant ionization, > 5 % in Ar, occurs. In this case, pressure-tuning itself is insufficient to compensate for the dispersion due to the plasma and quasi-phase matching (QPM) techniques must implemented. In one QPM scheme, a sinusoidal modulation of the waveguide's inner diameter induces an oscillating fundamental laser intensity which results in periodic variations in the harmonic production efficiency along the fiber. For the correct periodicity, the yield of high order harmonics with energies up to 300 eV can be substantially increased [8]. Another QPM scheme observed an increased harmonic flux via out-of-phase zone cancellation through the use of counter-propagating beams [9]. Other work has concentrated on manipulating the free electron propagation to optimize the single atom response. For example, optical fields have been used to control the electronic trajectories [10, 11] and selectively optimize a single harmonic [12].

Most HHG research noted above uses atomic gas targets. For this dissertation, the bulk of the work focuses on HHG from a diatomic molecular gas target. Molecules have non-spherically symmetric scattering cores. This asymmetry can be used to gain insight

into the ionization and recombination steps in HHG. We can exploit this knowledge to improve the HHG efficiency. Additionally, the HHG spectrum can be utilized as a probe of the dynamics of the molecular system [5, 13, 14].

In this dissertation, we discuss the development of the first HHG source in our lab which allows for the potential to image photo-excitation/ionization for pump-probe experiments in atoms and molecules. We also detail the first exploration of HHG from aligned molecules in a hollow-core fiber waveguide specifically focusing on how the molecular anisotropy affects the 1st and 3rd steps in the 3-step model. Also, we explicitly show that molecular alignment can affect the macroscopic propagation properties of the medium which emphasizes that the contribution of both the single molecule response and the phase matching properties of the gas are responsible for the alignment-dependent variation in the HHG yield. Next, the effect of the initial rotational temperature of the gas on the degree of alignment and the harmonic efficiency was explored through the construction of a liquid nitrogen cooled fiber.

The last section in this dissertation focuses on experiments performed using counter-propagating pump and probe beams to create an optical quasi-phase matching scheme. We explored the use of the counter-propagating pump beam to create periodic alignment in the fiber to enhance the harmonic efficiencies.

1.2 Harmonic Generation

High harmonic generation occurs when a short, intense laser field interacts with an atomic or molecular gas. On the single atom level, HHG can be explained using the quasi-classical three-step model [15]. In the first step, an intense, non-resonant electric field tilts the atomic potential, suppressing the binding barrier, see Fig. 1.1. A bound electron can
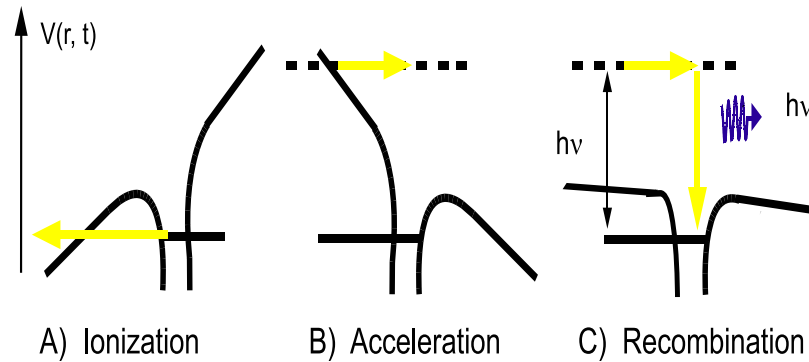
Figure 1.1: Illustration of HHG: Three-step model. (A) tunnel ionization, (B) acceleration of the free electron in the oscillating laser field, and (C) recombination and emission of high energy photon.

tunnel through the barrier, reaching the continuum with zero velocity. The "free" electron is accelerated by the oscillating laser field and moves on a classical trajectory. When the field reverses direction, the electron can return to the nucleus, recombine with its parent ion, and emit a high-energy photon. In a multi-cycle laser pulse, this can occur during each half-cycle of the laser field.

The coherent addition of the emission from each half-cycle results in a spectrum which consists of odd harmonics of the fundamental laser frequency. Even order harmonics are forbidden in systems that have inversion symmetry, i.e. harmonics generated from atomic media by a single-frequency laser field. The HHG spectrum has a distinctive profile as shown in Fig. 1.2. The harmonic spectrum structures can be derived from the square of the Fourier transform of the laser induced dipole moment. Perturbation theory can be used to describe the production of lower order harmonics (q< 9) which are produced at low intensities present during the rise and fall of the laser pulse or in the wings of the spatial intensity profile of the beam. The harmonic yields in this region decrease following the power law: $I_{\circ} = I_q^q$, where q is the harmonic order.
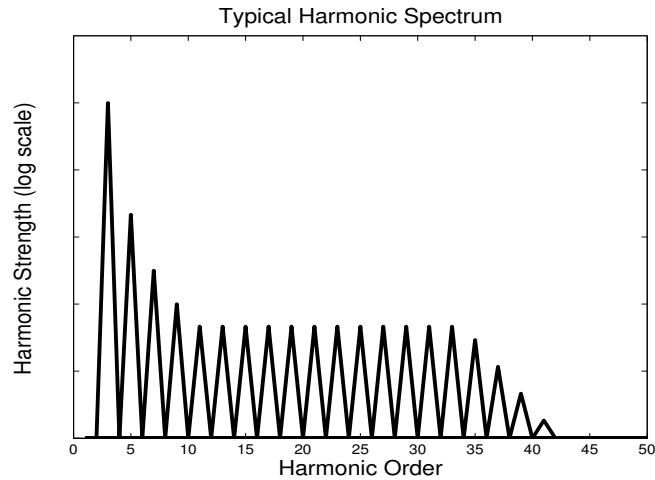
Figure 1.2: Simulated typical harmonic spectrum: the spectrum can be divided into three regimes, the perturbative, plateau, and cutoff which is determined by the maximum kinetic energy the electron can gain in the field.

The higher order harmonics are produced at larger laser intensities. Here, perturbation theory breaks down as the laser electric field strength approaches the inner-atomic field strength. In this intermediate (plateau region), the harmonic intensities are relatively constant with increasing order. In the plateau region, two interfering electron trajectories contribute to the harmonic spectrum [16]. Electrons in these two trajectories are ionized at different phases of the laser field but return to the core with the same velocity, and in turn, the same final kinetic energy at recombination. Following tunnel ionization, an electron that follow the "short trajectory" returns to the parent ion in less than half an optical cycle while an electron on the "long trajectory" returns after one-half of the laser period. An electron on the long trajectory is more strongly influenced by the ionizing laser field. This can cause spectral broadening due to the increased laser intensity dependence of the returning electron's phase [17]. For example in a sufficiently short pulse, the laser intensity varies rapidly. Electrons ionized on the leading (falling) edge of the laser pulse

experience increased (decreased) acceleration altering their phase at recombination. This leads to a blue (red) shift of the generated harmonic spectrum.

The plateau region ends in a sharp cutoff. The cutoff photon energy is determined by the maximum energy the recombining electron can obtain in the field and can be computed using classical [15] or quantum [18] techniques. Specifically, the harmonic cutoff is given by:

$$E_{max} = I_p + 3.17 U_p \tag{1.1}$$

where I_p is the ionization potential of the atom/molecule and $U_p = E^2/4\omega^2$ (a.u.) is the ponderomotive energy (the time-averaged energy associated with the oscillatory motion of the electron in the laser field), where E and ω are the laser field amplitude and frequency, respectively.

1.3 Propagation Effects

While the single-atom response accurately predicts the shape of the harmonic spectrum, it cannot account for the observed harmonic yield. The harmonic spectrum is due to the coherent, or partially coherent, sum of the radiated fields from contributing atoms throughout the generating medium. Propagation effects must be taken into account to theoretically reproduce the experimentally obtained harmonic strength. In a standard geometry, the fundamental laser field propagates through the medium while the generated harmonic signal builds up and propagates parallel to the fundamental. Different experimental geometries can be used to exploit macroscopic beam propagation effects to improve the temporal and spatial coherence of the harmonics as well as the yield in one or more harmonic orders [7, 19, 20]. For efficient harmonic production over a extended propagation distance, the generated harmonics and the fundamental must travel at the same

phase velocity, i.e. the process must be phase matched [21]. If phase-matched, the generated harmonics add constructively throughout the interaction length. Of course, since the harmonics photon energies exceed the bonding energies of electrons in most atomic and molecular gases, the generated harmonics can also be absorbed by the generating medium. The absorption length is a function of the gas density, ρ, and the wavelength dependent ionization cross section, $\sigma(\lambda)$, through the equation $L_{abs} = 1/\sigma\rho$ [22]. Propagation effects are discussed in greater detail in the following sections.

1.3.1   Phase Matching

The harmonic intensity of the qth order harmonic can be expressed as:

$$I_q \approx N_a^2 \left| \chi_{eff}^{(q)} E_o^s \right|^2 \frac{\sin^2(\Delta k L/2)}{(\Delta k L/2)^2} \tag{1.2}$$

where N_a is the number radiating atomic dipoles, χ is the effective nonlinear coefficient, E_o is the fundamental laser field, s is the order of the field dependence (typically, $s \sim 5$ in the plateau region)[21], L is the length of the interaction, and $\Delta k = k_q$ - qk_o is the phase mis-match. Phase mis-match between the fundamental, $E_o \propto e^{i(k_o x - \omega t)}$, and the qth order harmonic, $E_q \propto e^{i(k_q x - q\omega t)}$, depends on the neutral gas dispersion, the plasma dispersion, and a geometric term that depends on the focusing conditions and intrinsic phase [7]:

$$\Delta k = \Delta k_{plasma} + \Delta k_{neutrals} + (Geometric\ Term) \tag{1.3}$$

A gas-filled hollow-core fiber waveguide geometry is used in all experiments described in this dissertation. The fiber waveguide maintains constant laser intensity throughout the interaction region. This enables phase matching by tuning the pressure of the gas

inside the waveguide [6]. Eq.1.3 becomes:

$$\Delta k = \Delta k_{plasma} + \Delta k_{neutrals} + \Delta k_{waveguide} \tag{1.4}$$

or

$$\Delta k = P\eta N_{atm} r_e \left(q\lambda - \frac{\lambda}{q} \right) - \frac{2\pi(1-\eta)Pq\Delta\delta}{\lambda} + \frac{qu_{11}^2\lambda}{4a\pi^2} \tag{1.5}$$

where λ, q, η, P, N_{atm}, r_e, $\Delta\delta$, a, and u_{11} are the fundamental wavelength, the harmonic order, the ionization fraction, the gas pressure in atm, the target gas number density at 1 atm, the classical electron radius, the difference in the index of refraction at the fundamental and harmonic frequencies at 1 atm, the waveguide radius, and the first zero of the Bessel function J_0, respectively.

The waveguide dispersion is essentially constant for a given waveguide and, along with the plasma dispersion, gives a negative contribution to the phase mis-match. Conversely, the neutral dispersion gives a positive contribution. Thus, phase matching occurs when the waveguide and plasma dispersion terms are balanced by the neutral gas dispersion. At low fundamental laser intensities the ionization fraction is small, so there is negligible contribution from the plasma dispersion. The balance between the waveguide and neutral dispersion can be made by tuning the gas pressure inside the fiber. Fig. 1.3 shows typical phase matching curves for Ar and N_2 at I = 1x10^{14} W/cm^2 in a waveguide with a interaction length L = 4.5 cm and an inner diameter D = 150 μm.

To generate higher order harmonics, e.g. q > 29 in Ar, higher fundamental laser intensities are needed. At these intensities the plasma dispersion term becomes significant, shifting the optimum neutral gas pressure to higher values. Moreover, once the ionization
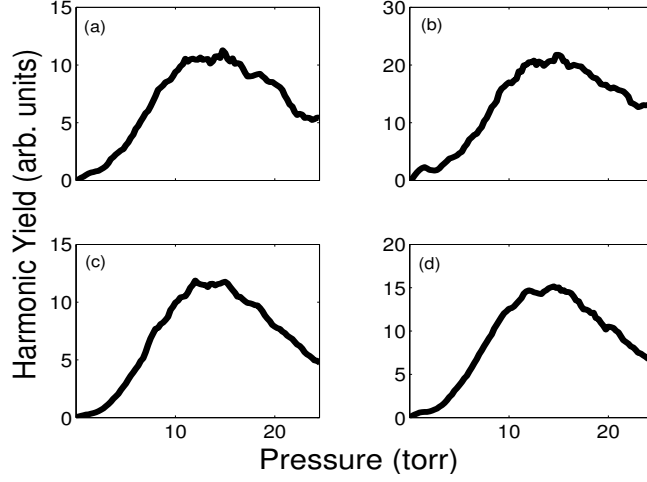
Figure 1.3: Measured harmonic output as a function of gas pressure inside a hollow-core waveguide at a laser intensity of 1×10^{14} W/cm^2. (a) and (b) are the 19th harmonic and 21st harmonic generated from Ar, while (c) and (d) are the 19th harmonic and 21st harmonic generated from N$_2$, respectively.

fraction reaches a critical value, the plasma dispersion term is larger than the neutral dispersion term for all pressures; thus, basic phase-matching is not possible [7]. This critical ionization fraction can be derived from Eq. 1.5 and is given by:

$$\eta_{cr} = (1 + \frac{N_{atm} r_e \lambda^2}{2\pi \Delta \delta})^{-1} \tag{1.6}$$

The critical ionization fractions for common gases are relatively low, 0.5% in He, 1% in Ne and 5% in Ar. This limits the photon energies that can be phase matched by simple pressure tuning to $q_{Ar} \leq 29$, $q_{He} \leq 76$, $q_{Ne} \leq 53$, $q_{N_2} \leq 29$ for harmonics generated from a 25 fs pulse. To phase-match the production of higher order harmonics alternative approaches must be used.

1.3.2 Quasi-Phase Matching

Quasi-phase matching (QPM) is a scheme which utilizes a periodic structure in the non-linear medium to correct for the phase mismatch throughout the medium [23]. The most common example of quasi-phase matching is periodic poling in ferromagnetic nonlinear crystals [24]. Since HHG is most conveniently done in gaseous media or on surfaces (because of the absorption of the generated harmonics in most materials), gas-filled hollow-core fiber waveguides are an ideal medium for QPM of high harmonics.

Previous experiments have implemented QPM by modulating the inner diameter of the hollow-core waveguide via a glass blowing technique. The varying diameter of the waveguide modulates the intensity of the fundamental beam [8], adding an additional term to Eq. 1.4:

$$\Delta k = \Delta k_{waveguide} + \Delta k_{plasma} + \Delta k_{neutrals} - K_m \tag{1.7}$$

where $K_m = \frac{2\pi m}{\Lambda}$, Λ is the modulation period, and m is the order of the QPM process. Eq. 1.5 becomes:

$$\Delta k = \frac{q u_{11}^2 \lambda}{4 a \pi^2} + P \eta N_{atm} re \left(q\lambda - \frac{\lambda}{q} \right) - \frac{2\pi(1 - \eta)Pq\Delta\delta}{\lambda} - 2\pi m/\Lambda \tag{1.8}$$

This QPM scheme has been used successfully to increase the harmonic yield of energies up to 300 eV. Unfortunately, the modulation period is fixed for a given fiber. This limits the range of harmonics for which a given fiber can quasi-phase match. In chapter 5 of this thesis we will discuss another QPM scheme utilizing counter-propagating (CP) beams to increase the high harmonic yields. There we will consider the effect of the CP pulse on the generation of harmonics from a diatomic gas.

1.3.3 Absorption

In addition to phase matching, absorption has a significant influence on the maximum harmonic production efficiency. The absorption length (L_{abs}) is highly dependent on wavelength. Typically, for photons energies exceeding the ionization potential of the gas target, L_{abs} is inversely proportional to wavelength, leading to less absorption of the higher order harmonics. Adapting Eq. 1.2 to include absorption effects, the harmonic intensities are given by:

$$I_q \approx N_a^2 \left| \chi_{eff}^{(q)} E_o^s \right|^2 \left(\frac{1 + e^{-2\alpha L} - 2e^{-\alpha L} \cos(\Delta k L)}{\alpha^2 + \Delta k^2} \right) \tag{1.9}$$

where α is the absorption coefficient, $\alpha = \sigma \rho / 2$. It has previously been shown that under phase-matched conditions the optimum harmonic yield is achieved if the medium length, $L_{med} > 3L_{abs}$ and $L_c > 5L_{abs}$, where the coherence length $L_c = \pi/\Delta k$ [25]. The experimental design must account for phase matching and absorption to maximize the yield within the desired harmonic range. Typically, our experiments are run at the optimum phase-matched pressure for the target harmonic range giving us a coherence length of $\approx \infty$ which fulfills the second condition. At these optimum pressures ($\sim$ 15 torr in Ar), the absorption lengths ranges from 7.5×10^{-2} cm for the 19th harmonic and 1.7 cm for the 29th harmonic. The medium lengths in our experiments, given by the length of the interaction region of the fiber, range from 5-7 cm which gives $L_{med} \geq 3L_{abs}$ for the harmonic q > 19th in our experiments.

1.4 HHG from Molecules

Until recently, the preferred media for HHG experiments were inert atomic gases, i.e. He, Ne, Ar, Kr, and Xe. However, the additional degrees of freedom and complicated symme-

tries in molecules can be exploited to investigate the ionization and recombination step in the three-step model. These steps can be highly dependent on molecular rotational and vibrational states. In diatomic molecules, controlling the angle between the molecular axis and the laser polarization can alter both the ionization and recombination steps. Experiments have shown the ionization probability of N_2 is $\sim 4 \times$ greater for molecules aligned parallel rather than perpendicular to the laser polarization [26]. Additionally, molecules have anisotropic recombination cross-sectional areas which can alter recombination probabilities and give rise to multi-center interference [27, 28]. Manipulation of these properties can enhance the yield of high order harmonics and give insight into the dynamics of the HHG process. Also since HHG occurs when the electrons are driven into their parent ion, the HHG spectrum can be used to determine the molecular structure and view molecular dynamics [5, 13, 29–31]. Our lab has the advantage of an available apparatus which enables the precise characterization of the degree of alignment achieved with the same laser and at the same gas temperature utilized in the HHG experiments.

Optical fields can be employed to control the angular distribution of molecules in a diatomic sample [32], and there are two categories of optical alignment schemes: adiabatic alignment and transient or "field-free" alignment. In both schemes, the molecules anisotropic polarizability, $\Delta \alpha = \alpha_\parallel - \alpha_\perp$, is exploited to preferentially align the most polarizable molecular axis along the laser polarization axis.

1.4.1 Adiabatic Molecular Alignment

In adiabatic alignment, the optical field pulse duration is much greater than the rotational period of the molecule, $\tau_{laser} \gg \tau_{rot}$. In this limit, the field experienced by the molecule is essentially a CW field which is "turned on" slowly compared to the rotational period of the molecule. During the field turn on, the free rotor eigenstates, in which the Hamiltonian
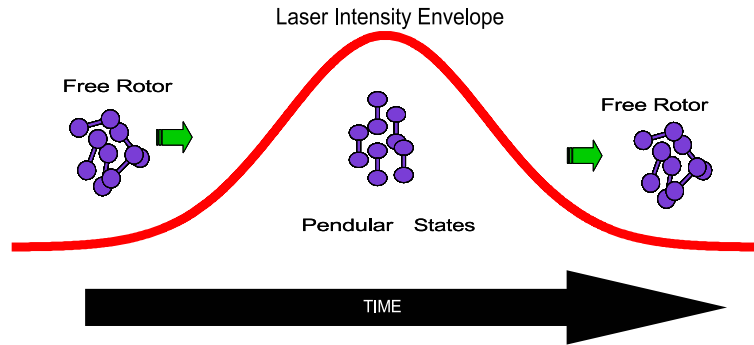
Figure 1.4: Adiabatic alignment schematic: Initially, a randomly aligned molecular sample interacts with a laser pulse aligning its most polarizable axis with the laser polarization axis. The molecules are only aligned in the presence of the laser pulse. After the field, the sample returns to its original randomly aligned state.

is given by $H = BJ^2$ where B is the rotational constant of the molecule, are transformed adiabatically into states of the full rotational Hamiltonian ($H = BJ^2 - \mu \cdot \mathbf{E}$) called "pendular states" (see Fig.1.4). In these pendular states, the molecules librate about the laser polarization axis [33]. After the laser pulse, the rotational population adiabatically evolves back into the free rotor angular momentum eigenstates. The pendular states only exist in the presence of the aligning laser field. The presence of the intense aligning field with the driving laser field results in a non-linear enhancement in the ionization which affects the phase matching properties of the medium. Additionally, previous experiments have shown a weak effect of alignment on the harmonic yields generated in an adiabatically aligned molecular sample [34].

1.4.2 Transient Molecular Alignment

Transient molecular alignment can occur when molecules are exposed to an intense, short laser ($\tau_{laser} \ll \tau_{rot}$) pulse. In classical terms, the laser field, $\vec{F}(t)$, induces a dipole moment $\vec{d} = \bar{\alpha}\vec{F}(t)$ in the molecule. This dipole experiences a torque, $\vec{\tau} = \vec{d} \times \vec{F}(t)$, in the presence
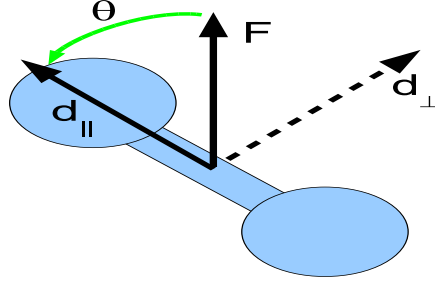
Figure 1.5: Cartoon of alignment angle θ

of the field. Here $\bar{\alpha}$ is the polarizability tensor for the molecule. For a rigid rotor, $\bar{\alpha}$ is diagonal in the molecular frame with values $\alpha_\parallel$ and $\alpha_\perp$ parallel and perpendicular to the molecular axis, respectively. For an initial angle, θ, between the laser field and the molecular axis, the torque has a magnitude, $\tau = 1/2\Delta\alpha F^2 \sin 2\theta$,

$$\begin{aligned} \tau &= d_\parallel F \sin\theta - d_\perp F \sin(90-\theta) \\ &= \alpha_\parallel F^2 \sin\theta\cos\theta - \alpha_\perp F^2 \sin(90-\theta)\cos(90-\theta) \\ &= (\alpha_\parallel - \alpha_\perp)F^2 \sin\theta\cos\theta \end{aligned}$$

and acts to align the molecular axis with the laser field. Here $\Delta\alpha \equiv (\alpha_\parallel - \alpha_\perp)$ is the polarizability anisotropy. The torque turns on and off rapidly during each laser field cycle, resulting in a time-average torque, $\langle\tau\rangle = 1/4\Delta\alpha F_0^2(t)\sin 2\theta$, where $F_0(t)$ is the temporal envelope of the laser field. For $\tau_{laser} \ll \tau_{rot}$, the torque is non-zero for only a brief time, giving the molecule an angular impulse. An ensemble of molecules, which are randomly aligned immediately preceding the kick, will, therefore, be preferentially aligned along the laser polarization axis soon after the kick.

In quantum mechanical terms, the "kick" creates an angular wavepacket in the molecules which are originally in angular momentum eigenstates. In a rigorous treatment,

the laser drives a series of Raman transitions through virtual intermediate, electronically excited states, populating a coherent superposition of rotational eigenstates. However, if the effect of the field is limited to teh Raman processes, i.e. no electronic or vibrational excitations, the molecule/field interaction can be parameterized in terms of the polarizability of the molecules as in the classical case. The time-average interaction potential is $\langle u \rangle = -\langle \vec{d} \cdot \vec{F} \rangle = -1/2\Delta\alpha F_0^2(t)\cos^2\theta$. Through the action of the transient potential, a molecule initially in a rotational eigenstate $|J_0, M_0\rangle$ will be in a superposition of rotational eigenstates following the laser pulse:

$$\Psi(t) = \Sigma c_J |J, M\rangle e^{(-iE_J t)} \tag{1.10}$$

and

$$|\Psi(t)|^2 = \sum_{J,J'} c_J c_{J'} \Psi_J^* \Psi_{J'} e^{(-i(E_{J'} - E_J)t)} \tag{1.11}$$

where $|J, M\rangle$ are spherical harmonics, E_J is the rotational energy, $E_J = BJ(J+1)$, B is the rotational constant of the molecule and the coefficients c_J are determined by the interaction potential.

The phases of the constituent eigenstates evolve at different rates so the wavepacket is characterized by time-dependent variations in the angular dependence of the polarizability distribution. Preferential alignment occurs when the angular distribution peaks in a given direction. Soon after the laser pulse, preferential alignment can be observed along the laser polarization axis. However, this localization is rapidly lost as the wavepacket evolves and the eigenstates dephase. Interestingly, since the energy differences, $\Delta E_{J,J'} = E_{J'} - E_J$, are integer multiples of the fundamental rotational frequency, $\Delta E_{1,0} = 2B$, the states
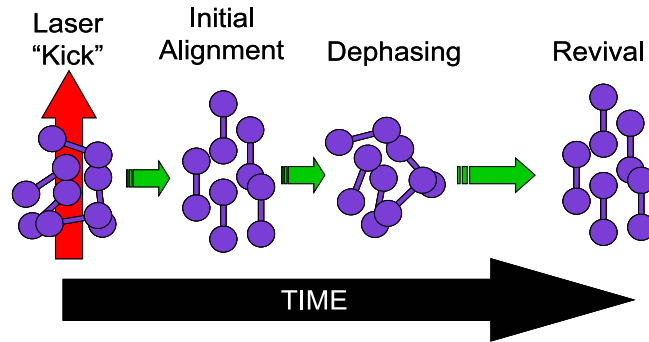
Figure 1.6: Transient alignment timing schematic: The laser creates a rotational wavepacket which rapidly aligns. The different eigenstates rapidly dephase. These states will rephase at calculable times related to the rotational constant of the molecule, $\tau_{revival}$ = π/B.

rephase at integer and half integer multiples of the fundamental rotational period, $\tau_{rot} = \frac{\pi}{B}$. These "revivals" occur under field-free conditions, see Fig. 1.6. The absence of the field allows for the direct probing of the dynamics of the molecular system or utilizing the aligned sample as a controllable anisotropic medium for HHG. The degree of alignment is not only dependent on the laser parameters, but is also determined by the molecules initial rotational states distribution. For a molecular sample with a finite temperature, the degree of alignment is the result of averaging over the initial distribution of rotational states, $|J, M\rangle$. Higher temperatures produce broader state distributions reducing the best obtainable alignment. The degree of alignment can be improved by reducing the initial temperature of the molecular gas [32, 35, 36].

1.5 Discussion

This dissertation discusses the results of several experiments exploring high harmonic generation from diatomic molecules. All of the experiments and analyses described in this work were conducted by the author under the guidance of Dr. Robert Jones. This

dissertation is organized into three main sections. First, Chapter 2 details the apparatus used to perform the experiments. Specifically, Chapter 2 gives an overview of the laser systems, hollow-core fiber waveguide, and the X-ray spectrometer.

The second section describes several experiments involving HHG from aligned molecules. Chapter 3 explores the harmonic yield as a function of the angle between the molecular axis and the laser polarization. In addition, experiments probing the recombination step as a function of alignment angle were performed through the use of elliptically-polarized light. Chapter 4 details the results of experiments which demonstrate that the harmonic response from aligned molecules can be increased by reducing the initial temperature of the molecular sample.

The third section describes an investigation of the effect of a counter-propagating laser pulse on HHG efficiency in a waveguide. Chapter 5 examines the dependence of the HHG yield on counter-propagating pulses with variable pulse durations and energies. The results from the previous sections are summarized in chapter 6. The appendices address various technical details of the experiments.

Chapter 2

Experimental Setup

2.1 Introduction

All of the experiments were conducted at the Center for Atomic, Molecular, and Optical Sciences (CAMOS) at the University of Virginia. This chapter is devoted to the description of the experimental apparatus which includes two Ti:Sapphire laser systems, a gas-filled, hollow-core waveguide for HHG, and an X-ray spectrometer. The laser systems are used to produce synchronized 30 fs and 130 fs laser pulses with central wavelengths of 790 nm. HHG occurs when the lasers propagate through the gas-filled waveguide. An X-ray spectrometer is used to measure the VUV yield over a range of harmonic orders (q = 15-35).

2.2 Ultrafast Laser Systems

Ti:Sapphire lasers are employed to produce the ultrafast laser pulses needed for all the experiments described in this dissertation. The laser systems are comprised of an oscillator which produces 790 nm pulses that are amplified in one of two configurations. In one setup,

a multi-pass amplifier produces 790 nm, 35 fs pulses with energies up to 1.5 mJ. The other uses a regenerative amplifier that produces 790 nm, 130 fs pulses with energies as high as 1.6 mJ. Both systems run at a 1 kHz repetition rate. Synchronization of the amplified output is facilitated by the use of seed pulses from a common mode-locked oscillator. The following sections describe these elements in greater detail.

2.2.1   Short Pulse Ti:Sapphire Oscillator

Both amplifiers are seeded by the same Kapteyn-Murnane Laboratories (KLM) Model MTS Mini Ti:Sapphire Laser Kit oscillator, as shown in Fig. 2.1. The KLM oscillator crystal is pumped by a 4.25 W, 532 nm CW beam from a Millennia Vs diode-pumped solid-state vanadate laser. The oscillator cavity has a large gain bandwidth, allowing for a large number of resonant cavity modes to be excited ($\sim 10^5$). The mode spacing is equal to c/2d $\approx$ 90 MHz, where d $\sim$ 160 cm is the cavity length. In CW operation these excited modes have random relative phases. However, if there is a well-defined phase relationship between the cavity modes (referred to as phase-locked or mode-locked) then coherent superposition of the modes can produce a train of short pulses. In Ti:Sapphire, mode-locking can be accomplished without an additional modulator. Instead, mode-locking is initiated by the introduction of noise into the cavity. In the MTS this is accomplished by physically jolting one of the dispersion-correcting prisms inside the cavity. The noise spike has a specific phase relationship across the excited modes and is more intense than the background. The non-linear Kerr effect in the Ti:Sapphire crystal creates an intensity dependent lens in the cavity. Through appropriate positioning of the static focusing optics (M2, M3) the laser gain is higher at higher intensities leading to preferential amplification of transients. The Kerr lens is a result of the intensity-dependent index of refraction (n) of the Ti:Sapphire crystal. Since n increases with intensity, and spatially, the beam is more
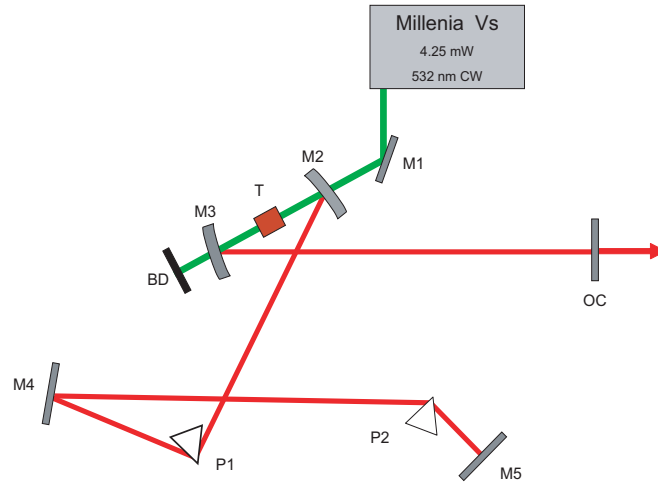
Figure 2.1: Diagram of KLM Ti:Sapphire oscillator: The principal cavity components include: the Ti:Sapphire crystal gain medium (T), focusing mirrors (M_2, M_3) for enabling Kerr lens mode-locking, an output coupler (OC), and the end mirror (M5). The prism pair (P1 & P2) compensate for the GVD acquired as the pulses propagate through the cavity [37].

intense at its center than near its edge, the material acts like a positive lens (self-focusing). The non-linear index also leads to self-phase modulation [38] which increases the spectral bandwidth of the pulse. The variation in the index induces an intensity dependent phase shift in the optical field, broadening the spectrum [38]. The added bandwidth generated through self-phase modulation can accommodate a temporally shorter laser pulse. However, shorter pulses are only produced if the appropriate phase relationship is maintained for all the spectral components. Kerr lensing provides positive feedback to encourage the amplification of the shortest possible pulses. However, when the pulse travels through various optical components, it experiences group velocity dispersion (GVD). GVD occurs when different frequency components in the pulse experience different frequency-dependent index of refractions and, therefore, travel at different group velocities. Two prisms are incorporated into the cavity to provide the negative GVD need to compensate for the

positive GVD produced by the rest of the cavity (i.e., mirror coatings and crystal).

When optimized, the KLM oscillator outputs a train of 15 fs pulses with a center frequency of 790 nm. The total output power from the oscillator is approximately 300 mW with pulse energies of ∼3 nJ. The intensities achievable with these pulse energies are insufficient for harmonic production thus amplification of the pulses is needed. A high voltage supply and a Pockels cell in combination with a thin film polarizer are used to extract amplifier seed pulses at a 1 kHz repetition rate from the 90 MHz pulse train. The seed pulses are sent to the multi-pass amplifier and the remaining pulses are sent to the regenerative amplifier.

2.2.2 Chirped-Pulse Amplifiers

Direct amplification of an ultrashort laser pulse is difficult to achieve because the high peak intensity of the pulse is above the damage threshold of the optics and crystals used for amplification. Also, self-focusing and self-phase modulation modify the spatial and temporal characteristics of the pulse. To prevent this, the pulse is temporally stretched by introducing a well-defined amount of linear chirp. This stretching reduces its intensity by several orders of magnitude. After amplification, the chirp is reversed to obtain huge intensity, ultra-short pulses for the experiments. The entire process is known as chirped-pulse amplification.

Expander

The expander consists of a reflective diffraction grating and several mirrors, as shown in Fig. 2.2 (A). The grating spatially disperses the pulse, with shorter wavelengths traveling a longer distance than the longer wavelengths. The input pulses are incident on the grating four times. The pulse exits the expander along nearly the same path as the input, but
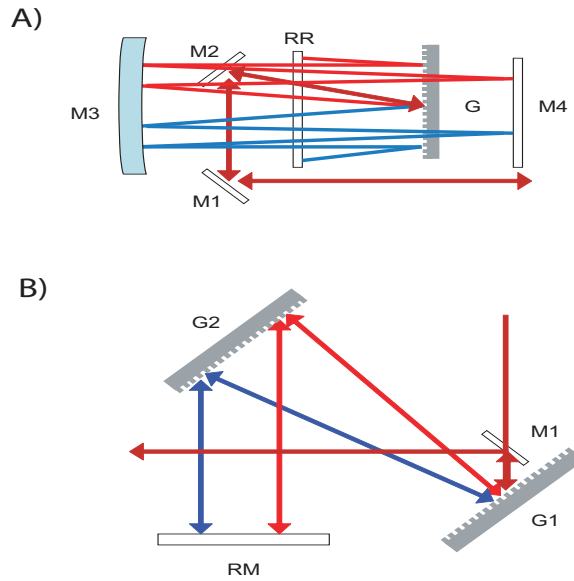
Figure 2.2: Diagram of pulse expander and pulse compressor. A) Schematic of expander: The input beam is diffracted a total of four times. The expanded beam is offset slightly vertically. B) Schematic of compressor: The gratings of the expander and compressor are aligned such that the GVD introduced by the expander is removed by the compressor. The second grating (G2) in the compressor can be moved to adjust the path length to pre-compensate for additional linear chirp add by the amplifier and experimental setup. Higher order dispersion can be reduced by using a slightly different angle of incidence for the expander and compressor gratings.

with a slight vertical offset. When properly aligned, the pulse exits the expander with an identical spatial mode as the input pulse, but with a positive temporal frequency chirp. Under the current configuration, a 15 fs input pulse leaves the expander with a duration of ∼300 ps. Throughout the expansion, the pulse loses approximately 40% of its original energy to specular reflections off the gratings.

Multipass Amplifier

The production of amplified 30 fs light is accomplished in a multipass amplifier, Fig. 2.3. The Ti:Sapphire crystal at the center of a triangular cavity is pumped by an Evolution-
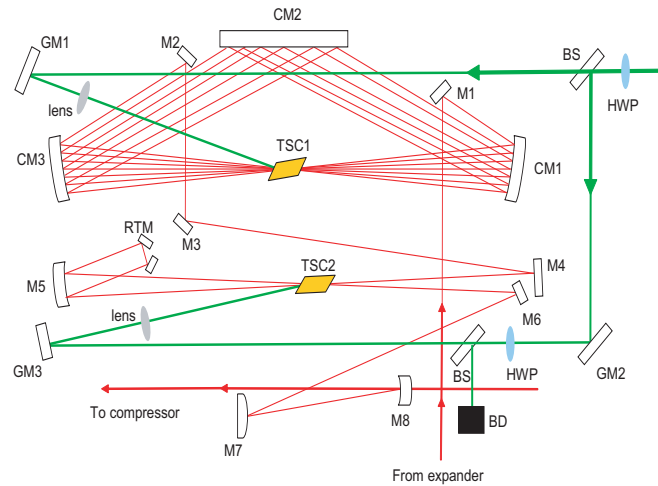
Figure 2.3: Diagram of multipass amplifier. The Ti:Sapphire crystals are optically pumped with the 532 nm light from an Evolution-30. The seed beam makes 8-9 trips through the cavity sweeping out gain from the crystal before being picked off by M2. Light exits the pre-amp at M2 and enters the power amp via M3.

30. The Evolution-30 is a pulsed Nd:YLF diode-pumped laser which produces 200 nsec, pulses centered at 532 nm with a repetition rate of 1 kHz and pulse energies up to 20 mJ. The Evolution output beam is split with 8.50 W going to the multipass pre-amplifier and 10.0 W going to a two-pass power amplifier. The seed light from the oscillator propagates through the pre-amp cavity sweeping out gain from the Ti:sapphire crystal. The beam makes approximately 8-9 passes throughout the cavity walking slightly in the horizontal direction on each pass until it leaves the cavity with pulse energies of up to 1.0 mJ. The beam is then sent into a double-pass power amplifier in a bow-tie configuration. After the power amplifier, the beam is collimated with dielectric mirrors. The power of the amplified beam can be controlled, somewhat, by using a half-wave plate to adjust the 532 nm pump power in the final amplification, enabling the creation of (uncompressed) pulse energies as high as 2.5 mJ. The amplified beam is then sent to the compressor to remove the linear chirp added by the expander.

Compressor

The amplified pulse has a linear frequency chirp from the expander and the additional dispersion accumulated from the amplification process. The pulse compressor acts similarly to the expander but instead adds negative chirp by making the shorter wavelengths travel a further distance than the longer wavelengths. Fig. 2.2 (B) illustrates a typical pulse compressor. To effectively compensate for the linear chirp, the compressor gratings are set to match the gratings in the expander. The gratings' angle and separation distance can be tuned to reduce the higher order dispersion terms and produce the shortest pulse inside the experimental region.

Regenerative Amplifier

The 130 fs pulses are produced in a regenerative amplifier, as illustrated in Fig. 2.4. The regenerative amplifier is a commercial Spectra-Physics Spitfire system. The Spitfire has a grating expander and compressor within its enclosure. The seed beam enters the regenerative amplifier cavity by reflection off the Ti:Sapphire crystal. If no voltage is applied to either Pockels cell, (PC1, PC2), seed pulses make one round trip in the cavity before being ejected by reflections from the laser crystal and thin film polarizer (TFP). When voltage is applied to the first Pockels cell (PC1) it rotates the polarization of the seed beam by 90°, capturing the pulse in the cavity. The seed beam propagates through the cavity sweeping out gain from the Ti:Sapphire crystal which is pumped by a pulsed Nd:YLF diode-pumped laser (an Evolution-30). Once the gain is saturated, approximately 10-15 round trips, voltage applied to another Pockels cell (PC2) is used to rotate the beam polarization by 90°, switching it out of the cavity by reflection off a thin film polarizer. The light leaves the regenerative amplifier with pulse energies up to 1.6 mJ. The amplified
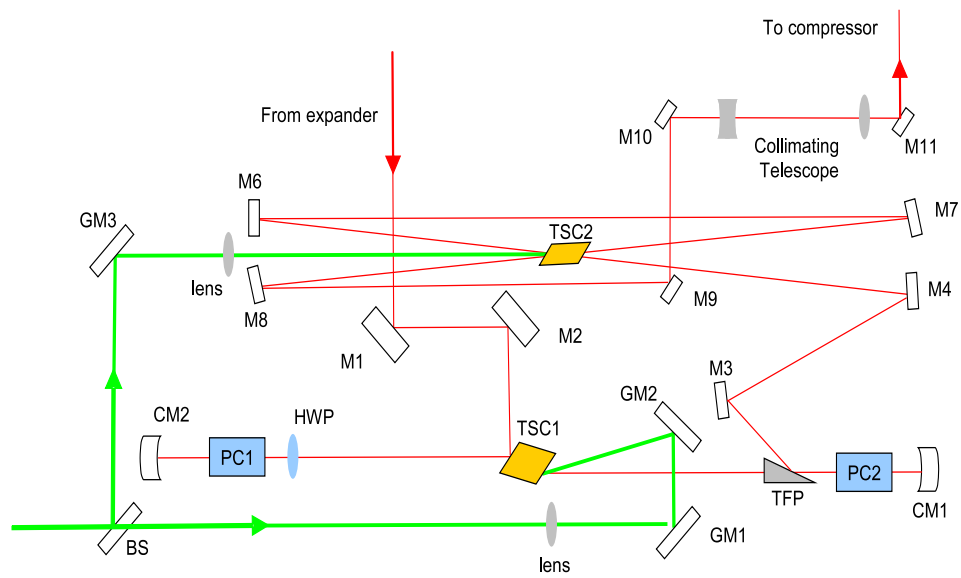
Figure 2.4: Diagram of regenerative amplifier. The Ti:Sapphire crystals are optically pumped with the 532 nm light from an Evolution-30. Voltage across the Pockels cell rotates the polarization of the seed beam by π switching it into the cavity. The seed makes $\sim$10 trip through the cavity sweeping out gain from the crystal before having its polarization rotated again. The amplified light is deflected out of the cavity by a thin film polarizer (TFP).

pulses then enter a linear power amplifier similar to the one described above. The linear amplifier adds $\sim$ 800 to 1000 μJ. The amplifier produces pulses with uncompressed pulse energies of up to 2.6 mJ. The amplified light is collimated then sent to the compressor.

2.3 Laser Diagnostics

Characterization of ultrashort pulses can not be done with conventional electronic detectors because their response times are on the order of picoseconds or more. Therefore, optical detection methods are required. Specifically, other short pulses or the pulse itself can be used to probe the temporal and frequency profiles of the laser pulse. The following sections describe several such techniques used in our lab.

2.3.1 Autocorrelator

In an intensity autocorrelator, the short pulse is split into two identical pulses which are then crossed in a non-linear crystal. There are two primary configurations for autocorrelators: single-shot and scanning. The single shot configuration is highly advantageous because feedback is given in real-time. In the single shot configuration, Fig. 2.5, the beam is incident on two half mirrors which direct the two halves of the beam into a BBO crystal at a small angle of 2Φ. The temporal profile is extracted from the second harmonic generation (SHG) signal along the axis transverse to the laser propagation [39]. The width of the SHG profile Δw is a function of the width of the autocorrelation function $\Delta\tau_a$ and is given by:

$$\Delta w = \frac{\Delta\tau_a v_g}{sin(\Phi)} \tag{2.1}$$

where v_g is the group velocity and $\Delta\tau_a$ is given by:
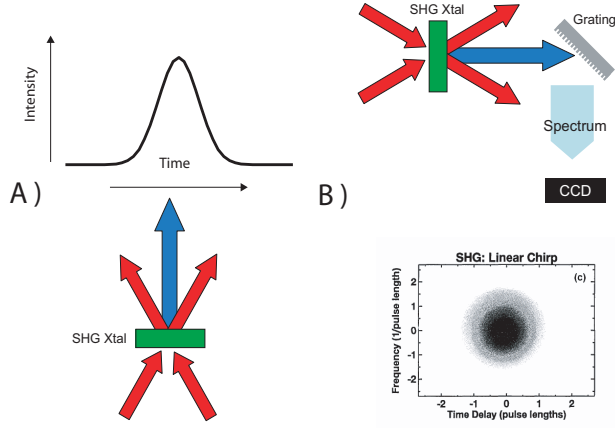
Figure 2.5: Diagrams of single shot autocorrelator and SHG FROG: A) Schematic of single shot autocorrelator with output signal. The pulse is split to two pulses which are crossed in a BBO SHG crystal. The temporal profile of the pulse is extracted from the intensity of the SHG response. B) SHG FROG schematic and sample trace from DeLong, et al. [40]. The SHG FROG is constructed similarly to a single shot autocorrelator with the exception of sending the SHG signal to a spectrometer.

$$\Delta\tau_a = \int\limits_{-\infty}^{\infty} I_o(t)I_o(t-\tau)dt \tag{2.2}$$

The other possible configuration is the scanning auto-correlation configuration. This is accomplished with a Michelson interferometer, where the relative delay between the two pulses is scanned by changing the optical path length of one of the interferometer arms. The SHG response is the convolution of the two pulses. Assuming a Gaussian pulse shape, the resulting convolution is a Gaussian. The ultrashort pulse width, σ, is related to the SHG response width , σ_{SHG} by $\sigma = \frac{\sigma_{SHG}}{\sqrt{2}}$.

2.3.2 Cross-Correlator

The cross-correlator construction is similar to that of an autocorrelator except that the pulses are not identical. In this instance, a shorter probe pulse of known temporal profile (pulse width, σ_{probe}) is used to probe the temporal characteristics of a longer pulse with unknown temporal profile by monitoring the SHG response as the relative delay between the two pulses is scanned. For Gaussian pulses, the relationship between the SHG response width, σ_{SHG}, the probe pulse duration, σ_{probe}, and the unknown pulse duration, σ is given by:

$$\sigma_{SHG} = \sqrt{\sigma_{probe}^2 + \sigma^2} \tag{2.3}$$

If the probe pulse width is much smaller than the unknown pulse width, then $\sigma \approx \sigma_{SHG}$.

2.3.3 FROG

To obtain real-time temporal intensity and phase information, we employ a technique called frequency resolved optical gating (FROG). There are numerous FROG geometries but the basic concept is the same: the laser pulse is split into two pulses that are crossed in a non-linear optical medium, and the spectrum from the resulting correlation is imaged by a grating spectrometer [41]. The resultant measured spectrogram (FROG trace) is a function of both the frequency ω and the relative delay τ:

$$I_{FROG}(\omega, \tau) \propto \left| \int_{-\infty}^{\infty} E_{sig}(t, \tau) e^{-i\omega t} dt \right|^2 \tag{2.4}$$

where E_{sig} is the signal field generated by the two pulses interacting in the non-linear medium and is proportional to $E(t)g(t - \tau)$, and $g(t - \tau)$ is a gate-function determined by the geometry and non-linear process used.

We utilize a single shot SHG FROG geometry, shown in Fig.2.5, where the second harmonic generated by the pulse crosses is sent to a spectrometer. The gate function for an SHG FROG is g(t,τ) = E(t - τ) [40]. The SHG FROG trace allows for the real-time feedback of pulse duration, chirp, self-phase modulation, and spectral width. In addition, a video frame grabber can be used in conjunction with an iterative algorithm to extract the temporal intensity and phase in a laser pulse from a FROG spectrogram.

2.4 Hollow-Core Fiber Waveguide

We generate high harmonics in a gas-filled hollow-core fiber waveguide. The use of a hollow-core waveguide for HHG eliminates the need for a vacuum chamber beyond the fiber and the spectrometer. As compared to a standard high pressure cw or pulsed valves, the waveguide design is compact and the vacuum pumping requirements are dramatically reduced. Additionally, there is the potential for an enhancement of HHG yields due to phase-matching over a longer interaction length since the high laser intensity is maintained along with a constant gas pressure and no Gouy phase shift.

The hollow-core fiber is a polyimide-coated fused silica capillary with an inner diameter of 150 μm. The waveguide is based on a three section design [6], which uses the two outer sections for differential pumping while maintaining the center section (interaction region) at constant pressure. The three sections are held aligned and in place using a section of glass capillary with 1/4" OD and 380 μm ID. The method used to assemble the waveguide in the capillary is described in Appendix A. Fig. 2.6 illustrates the basic fiber design. The fiber lengths range from 6 cm to 11 cm with an interaction region of 3.5 cm to 7.5 cm. The length of the differential pumping sections for all fiber lengths is $\sim$1.5 cm. The pressure immediately outside the waveguide was held at rough vacuum ($\leq$ 3x10^{-2}) for gas
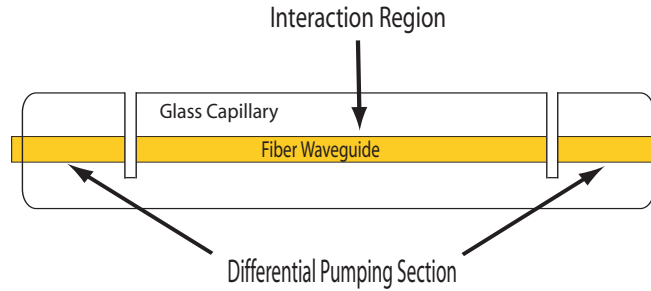
Figure 2.6: Diagram of typical waveguide design. The three sections of the hollow-core fiber are held concentrically by a glass capillary. The three piece design maintains the center section at constant gas pressure while limiting the gas flow and reducing the vacuum load.

pressures in the fiber ranging from 0 to 80 torr.

Three separate vacuum cell designs were utilized to back-fill the hollow-core fiber with the target gas. In the first cell design, two KF-40 compression ports held the fiber in place and acted as the gas supply cell. Swagelok connections were used to feed the gas into the KF cell. This cell worked well but was heavy and ridged, restricting the total fiber length to 9-10 cm. The second design's aim was to reduce the cell weight and enable us to use different fiber lengths. We used glass-blown cells. The fiber was sealed to the cells with Torr Seal. The fiber and the cell were connected to the rest of the chamber via Swagelok connections. The use of nylon ferrules allowed for a good vacuum seal without the risk of cracking the fiber. Several glass cells of differing sizes were made which allowed variation in the fiber lengths. The last design uses the same Swagelok connection on the fiber but the gas is directly sent to the fiber through the separation between the fiber sections. Stainless steel tubes were Torr Sealed to the fiber and acted as the gas inlets. This design is lightest of the three and has the ability to be adapted to any fiber length. For all vacuum cell designs, the gas pressure inside the fiber is controlled by a needle valve and is monitored by a capacitive manometer.

When focusing the fundamental laser pulse into the waveguide there is a significant loss in intensity. The light propagating in the waveguide can be approximated as a plane-wave and the propagation losses over the length of the fiber are minimal [6]. The hollow-core fiber modes are non-Gaussian, thus the entire intensity loss can be attributed to fiber coupling. Our typical coupling efficiency is 60% with a maximum observed efficiency of 68%, which is on par with other published efficiencies [42]. The generated harmonics depend not only on the intensity of the light in the waveguide but are also sensitive to the specific propagation mode in the fiber. Beam alignment and an input aperture are used to couple into the lowest order mode of the waveguide, the EH_{11} mode [43]. Typically, the aperture selects the innermost portion of the beam with a diameter of 7-8 mm. The apertured beam is focused into the fiber using a 40 cm focal length lens.

2.5 X-Ray Spectrometer

The final key component is the detector for the generated harmonics. We use a McPherson 248/310G One Meter Grazing Incident Monochromator and a BrightView Model XUV-2010 microchannel plate (MCP) image converter (see Fig. 2.7). After the fiber, the generated harmonics and fundamental beams pass through a variable vertical slit. They are then incident on a Luxel, 1500 angstrom Al filter which absorbs the fundamental and lower order harmonics (q < 13) but transmits VUV wavelengths from 18 nm to 60 nm. The transmission efficiency through the filter over this wavelength range is quoted as 80%, but oxidation over time can reduce the transmission efficiency to as low as 10% [44]. The transmitted harmonics are incident on a 300 or 600 grooves/mm concave diffraction grating at an angle of 86.0°. The spatially separated diffracted harmonics are detected using a matched pair of 50 mm diameter Burle Image Quality microchannel plates (MCP)
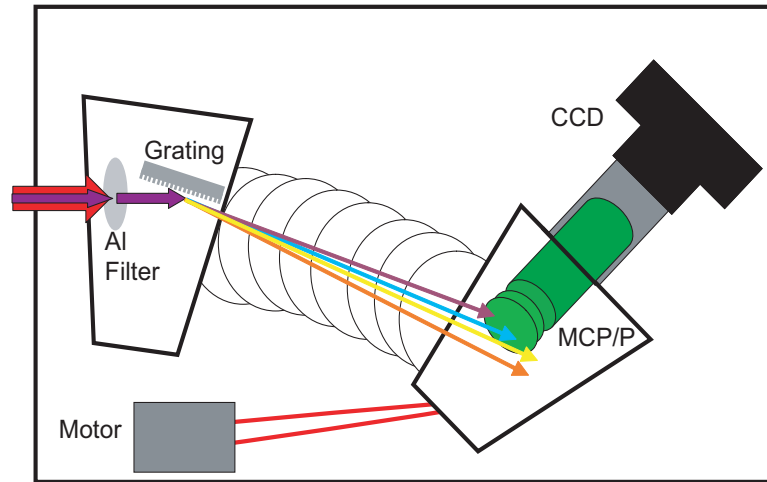
Figure 2.7: X-Ray spectrometer schematic. The generated harmonics diffract from a grating whose housing is connected to the detector by a bellows. The diffracted harmonics are incident on a pair of MCPs that are coupled to a phosphor coated fiber optic. The resultant signal is imaged by a CCD camera.

that are mounted above a phosphor-coated fiber optic bundle. The electrons emitted from the MCPs hit the phosphor-coated fiber optic. The resulting fluorescence image is transported outside the chamber via the fiber bundle. The output image is captured by an Apogee SPH5 CCD camera controlled with Kestral Spec software from Catalina Scientific Corporation. The entire MCP/P detector is free to move along a Rowland circle to view different wavelength ranges [45]. The center wavelength of the range detected by the MCP/P detector is governed by

$$\lambda = d \left\{ \sin(\alpha) - \sin \left[\arccos \left(\frac{X}{R} \right) \right] \right\} \tag{2.5}$$

where λ is center wavelength in Angstroms, d is grating function ($\frac{1}{(grooves/mm)} * 10^7$), α is angle of incident in degrees, X is counter reading in inches and R is grating radius in inches. The detector position is moved via a McPherson Model 789A-3 Scan Controller
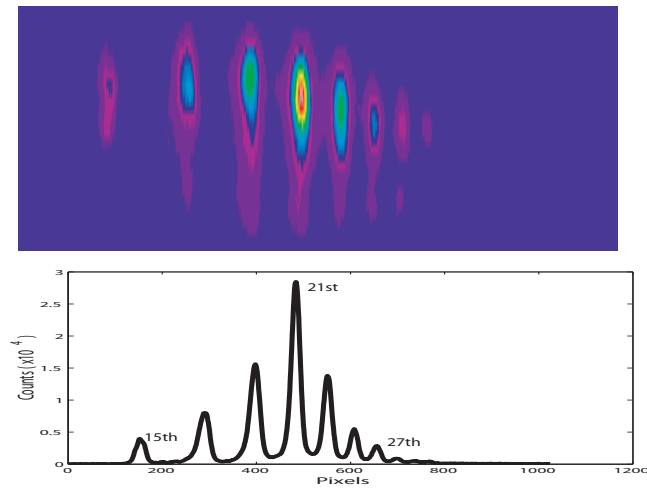
Figure 2.8: Typical harmonic spectrum: Image and the derived spectral curve.

controlled by a supplied LabView program.

During data collection the fluorescence image is obtained by integrating over many laser shots. The typical integration times range from 0.5 to 30 seconds, i.e. 500 to 30,000 laser shots, and a background blank is subtracted from each image. The upper image in Fig. 2.8 is a typical spectral image where the intensity is in units of counts. The image counts are summed over the columns to produce the spectral curves, lower curve in Fig. 2.8. The spectral data is then analyzed using MATLAB. A variety of MATLAB m-files have been written for different analyzes depending on the data collection procedures.

Chapter 3

High Harmonic Generation from Transiently Aligned Diatomic Molecules

3.1 Introduction

High harmonic generation can be used to probe the dynamics of rotationally excited molecules. The harmonic emission spectrum is sensitive to the relative angle between the molecular axis and the laser polarization as well as the ionized electronic wavefunction. This angular dependence can be exploited to improve harmonic efficiency at the single molecule level [27, 46]. Each of the three steps leading to HHG can be influenced by the molecular alignment relative to the fundamental laser polarization. First, the ionization rate has an angular dependence due to differences in the tunneling ionization potential seen by the ground-state wavefunction [47, 48]. Second, the recollision probability is inversely proportional to the lateral spread of the ionized wavepacket as it propagates in

the continuum. The amount of lateral spreading is determined by the transverse extent of the ground-state wavefunction when it tunnels out of the molecular binding potential [49, 50]. Third, the recombination cross section depends on the orientation of the molecular axis with respect to the propagation direction of the returning electron.

Molecular alignment also influences the macroscopic harmonic yield by altering the properties of the gas through which the harmonics propagate. First, the index of refraction of a gas is a function of the molecular alignment angle. Second, the tunneling ionization rate and the resulting free electron density in the gas is alignment dependent. Both of these affect the degree to which the generated harmonics are phase-matched with the fundamental as they propagate through the generating medium. Some degree of phase-matching is critical for observing harmonics.

The angular dependence of HHG has been studied previously by focusing both the alignment and HHG pulses into a pulsed gas jet [34]. In this gas jet configuration, the harmonic efficiency is limited by the short interaction distance, which is on the order of the confocal parameter ($\sim$ 3 mm for a 40 f-number lens). In addition, the laser beam undergoes a π-phase shift as it passes through the focus, known as the Gouy phase shift [51]. This intrinsic phase shift reduces the harmonic output due to interference [52] and eliminates the ability to phase-match the HHG process over an extended propagation distance. These limitations can be overcome with the use of a hollow-core fiber waveguide. In the waveguide, both the alignment and signal beams are coupled into the fiber and the interaction region can be significantly increased, $L_{med} \sim 5$ cm for the experiments presented here. The beams propagate through the fiber in a low order waveguide mode, predominantly the EH_{11} mode, and can be approximated as plane waves in the target gas. The waveguide also allows for greater control of the gas pressure in the interaction region enabling more precise tuning of the phase-mismatch for given experimental parameters

and, thus, substantially enhancing the harmonic yields [7].

Specifically in this chapter, we describe measurements of the harmonic yield for different angular distributions of both homonuclear, N_2, and heteronuclear, CO, molecules. We sample these distributions at specific instances during the evolution of a rotational wavepacket. We determine the contribution of the recombination by recording the harmonic emission as a function of the ellipticity of the fundamental laser for various molecular alignments. In the last section of this chapter, we explore the effect of alignment on the macroscopic properties of the medium and the resulting influence on harmonic yield. We observe a previously unobserved reversal of the HHG revival structure at higher harmonic orders due to changes in the phase-matching properties of the gas. This reversal explicitly shows that the macroscopic effects can be just as, if not more important in determining the harmonic yield. Great care must be taken when attempting to extract structural or dynamical information about the target gas by interpreting the harmonic signal using the single molecule response alone [29, 53].

3.2 Experimental Design

The experiments are performed using a Michelson interferometer to split the amplified, 30 fs laser pulse into two collinear beams, a "pump" beam for the preparation of the transiently aligned molecular sample and a probe/signal beam for creating high-order harmonics. The apparatus is illustrated in Fig. 3.1. After the interferometer, each beam has a pulse energy of up to 300 μJ. Linear chirp is added to the pump pulse by introducing a dispersive medium (i.e. glass window) into the beam path. The glass window increases the pump pulse duration to $\sim$85 fs and reduces the pulse intensity by about a factor of 3. The reduced intensity of the pump pulse enables the transient alignment of the
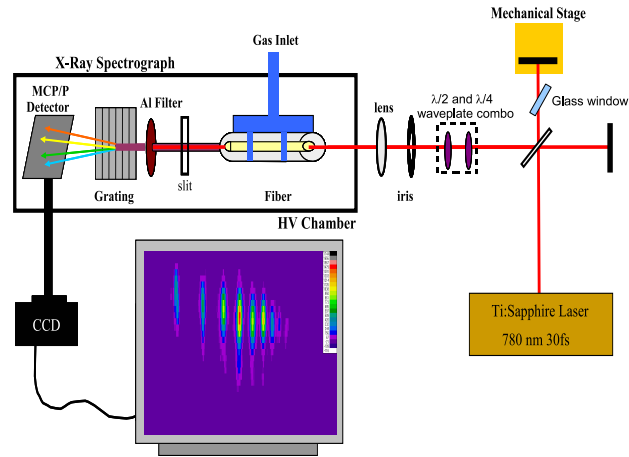
Figure 3.1: Experimental setup for the preparation and measurement of the harmonics generated in a transiently aligned molecular sample.

molecular sample, while minimizing both the ionization and the HHG contributions from the pump pulse. Additionally, a quarter-waveplate can be inserted into the alignment arm of the interferometer to control the relative angle between the polarizations of the two beams and, thus, controlling the relative angle between the harmonic generating pulse polarization and the molecular axis at the revival time. The relative delay between the pump and probe pulses is controlled via a mechanical delay stage in one arm of the interferometer. Both collinear beams are coupled into the fiber waveguide by a 400 mm focal length lens. The gas pressure inside the fiber is regulated by a needle valve and is monitored by a capacitive manometer. The generated harmonics are detected by the grazing incidence X-ray monochromator detailed in chapter 2.
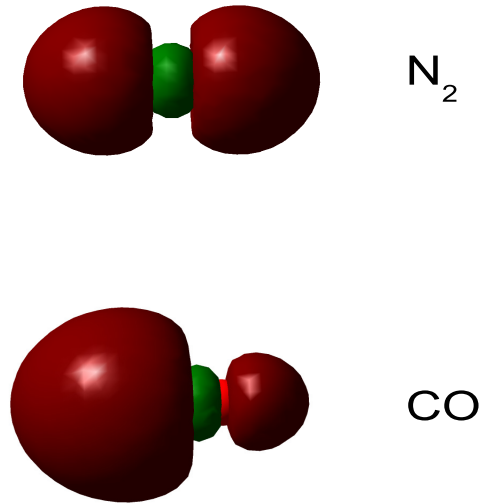
Figure 3.2: Image of the highest occupied molecular orbital for N_2 and CO calculated with the use of Gaussian 03 [56].

3.3   Harmonic Intensities from Rotationally Excited N_2 and CO

It has been shown that harmonic yield from a molecular gas can be enhanced by an order of magnitude through control of the molecular orientation and phase-matching properties of the medium [54]. The understanding of the alignment dependence of the harmonic yield is essential to exploiting this potential yield enhancement. The alignment dependence of the harmonic yield is primarily determined by the symmetry of the molecule's highest occupied molecular orbital (HOMO) [55]. In this section, we investigate HHG from two rotationally excited diatomic species, N_2 and CO. N_2 and CO have the same cylindrical symmetric σ HOMO, but while the σ orbital in N_2 is evenly distributed between both nuclei, the orbital in CO is more concentrated around the C site, see Fig. 3.2. There is a predicted preference for ionization from the C rather than the O site due to the asymmetric electron
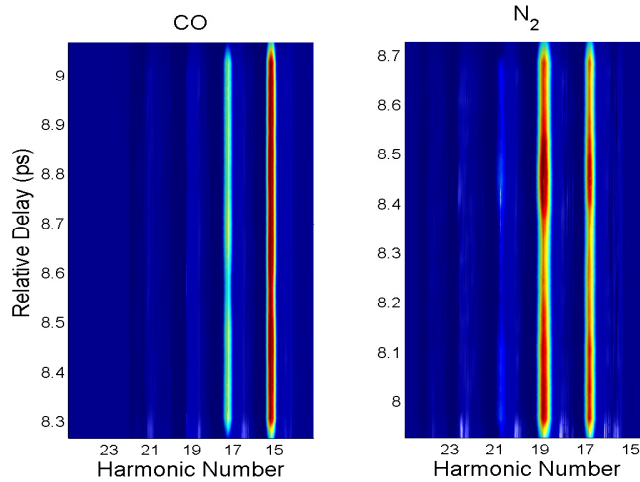
Figure 3.3: The measured harmonic spectrum as function of relative time delay between alignment and generation pulses for target gas species (A) CO and (B) N_2.

distribution of its HOMO [57]. As discussed further in Sec. 3.6, on the single molecule level, the ionization anisotropy of CO can lead to different harmonic contributions from the positive and negative half-cycles of the driving laser field, potentially allowing for the production of both even and odd order harmonics [58].

3.3.1 Delay-Dependent Variation in HHG Yield from Transiently Aligned Sample

The harmonic yield was measured as a function of the pump-probe delay around the first full revivals, $T = (B_0 c)^{-1}$, of N_2 and CO, i.e. for delays near t = 8.46 ps and t = 8.64 ps, respectively. Fig. 3.3 shows the harmonic spectrum from CO (A) and N_2 (B). The molecular alignment was produced by a 85 fs pulse with an intensity of about 2.7×10^{13} W/cm^2 while the harmonics were generated by a 30 fs pulse with an intensity of about 1×10^{14} W/cm^2. For each gas, the data were collected at the optimum phase-matched pressure (7 torr for N_2 , 8 torr for CO). As a result of the different IPs (14.014 eV for CO,
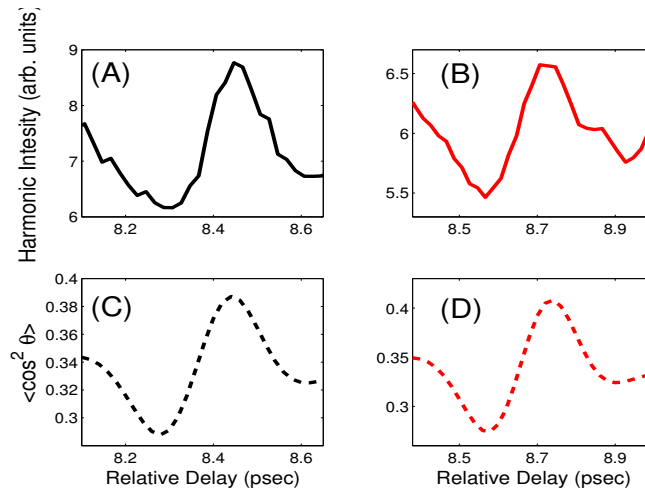
Figure 3.4: (A)-(B) The measured intensity of the 19th harmonic as function of time delay for N_2 and CO. (C)-(D) The calculated alignment parameter, $\langle \cos^2 \theta \rangle$. The variations in the harmonic intensities are well correlated with the calculated alignment.

15.581 for N_2) the cutoff energies of the two species are different. For our experimental laser intensity, the cutoff energies (derived from Eq. 1.1) are 32 eV and 34 eV or 21st and 23th orders for CO and N_2, respectively.

From Fig. 3.3, the total yield of the 19th harmonic as a function of pump-probe delay for N_2 and CO is shown in Fig. 3.4 (A) and (B), respectively. Each curve in Fig. 3.4 consists of 41 data points. Typically, 4-10 data sets are averaged together to form the alignment curves. The resulting curve is then filtered by a three point moving average that reduces the random spikes in the data. We observe contrast (peak to trough) ratios of 1.5 and 1.3 from rotational wavepackets in N_2 and CO, respectively. These contrast ratios are typical, however, a contrast ratio as large as 3 has been observed in N_2. The degree of molecular alignment can be quantified using the $\langle \cos^2 \theta \rangle$ for the ensemble, where θ is the angle between the aligning laser polarization and the molecular axis. We find that primary variations in the harmonic yield occur at predicted rotational revival times which

are marked by pronounced temporal variations in the molecular alignment parameter. Comparison of Figures 3.4 A and B with Figures 3.4 C and D show that the variations in harmonic yield are well correlated with the alignment parameter. Apparently, the harmonic yield increases as the alignment parameter increases, reaching a maximum when the molecules are maximally aligned along the signal laser polarization and a minimum when the molecules are preferentially aligned in a plane perpendicular to the polarization axis.

We use a quantum rigid rotor simulation to compute the ensemble averaged angular distribution of the target molecules following the alignment pulse. The time-dependent Schroedinger equation is solved for a thermal ensemble of rigid rotors under the influence of an induced dipole interaction potential, $u(\theta, t) = -\frac{1}{4}E^2(t)\Delta\alpha\cos^2\theta$ where $E(t)$ is the laser electric field envelop and $\Delta\alpha$ is the anisotropic polarizability. In this simulation, the rigid rotor energies are given by: $E_J = B_\circ J(J+1) - D_e J^2(J+1)^2$, where B_0 is the rotational constant in the ground electronic and vibrational states, and D_e is the deformation constant due to centrifugal distortion. The value of $\langle\cos^2\theta\rangle$ is 1/3 for randomly aligned molecules. Fig. 3.4 shows that both N_2 and CO efficiently produce harmonics when the molecules are preferentially aligned along the laser field, and there is a suppression of the harmonic generation for perpendicularly-aligned molecules. The predicted variation in $\langle\cos^2\theta\rangle$ is smaller for N_2 than for CO, $\frac{\langle\cos^2\theta\rangle_{max}}{\langle\cos^2\theta\rangle_{min}} = 1.35$ vs 1.49 due to the greater polarization anisotropy in CO (6.5 a.u. compared to 4.7 a.u. in N_2). This implies that the variation in harmonic yield is determined by the specific angular-dependent properties of the target gas, i.e. anisotropies in the ionization, the recolliding electron flux and, as discussed later, the macroscopic phase matching properties of the medium.

3.3.2   Discussion

The similarity of the delay-dependent harmonic yield to the ensemble alignment parameter suggests that the angular dependence of the harmonic intensity is proportional to $\langle \cos^2 \theta \rangle$ to lowest order. This is typical for molecules whose highest occupied molecular orbital (HOMO) has σ_g symmetry [31] due to the larger spatial distribution of the molecular orbital along the molecular axis. This results in an increase in the recombination probability for electrons returning on trajectories parallel to the molecular axis. In addition, as noted previously, there is an increase in the ionization probability for molecules aligned along the laser polarization. Thus, the rates for both the 1st and 3rd processes in the 3-step model are enhanced by molecular alignment [26, 59].

In general, the angular dependence of physical processes in axially symmetric, linear molecules can be expressed as an expansion of orthonormal functions (e.g. the Legendre polynomials) [59]. In particular, the angular dependence of the harmonic yield can be modeled by an expansion of the moments of $\langle \cos^{2N} \theta \rangle$ for N = 0, 1, 2, .., ∞:

$$
\begin{aligned}
I_q(\theta) &= \sum_{N=0}^{\infty} \alpha_N \langle P_{2N}(\cos \theta) \rangle \\
&= \alpha_0 + \alpha_1 \langle \cos^2 \theta \rangle + \alpha_2 \langle \cos^4 \theta \rangle + ...
\end{aligned}
\tag{3.1}
$$

where θ, $P_{2N}(\cos \theta)$, and α_N are the angle between the laser polarization and molecular axis, the Nth order Legendre polynomials, and constants that can be fitted or determined by quantum mechanical calculations of the ionization and recombination process [18].

We produce fits for both the CO and N_2 data using a least squares fit of the HHG signal to the moments $\langle \cos^{2N} \theta \rangle$ generated from the alignment simulation laser pulse parameters consistent with our experimental conditions, Fig. 3.5 and Fig. 3.6, respectively. Typically, the time-dependent HHG alignment structure has been assumed to scale similarly to the
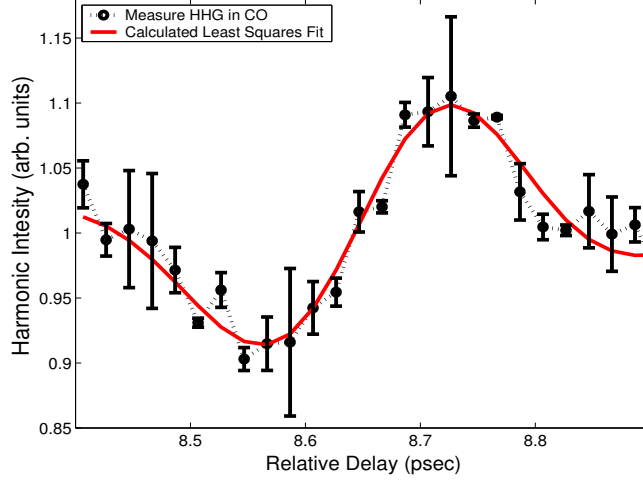
Figure 3.5: Modulation in harmonic intensity of the 19th harmonic generated in rotationally excited CO. The solid line is the fit of the data in terms of Eq. 3.1 with the inclusion of only constant and N=2 terms in the expansion: $I_{19}(\theta) = .67 + 1.6\langle\,\cos^4\theta\,\rangle$.

alignment-dependent ionization, as $\langle\,\cos^2\theta\,\rangle$ [26, 60]. However, recent analytic work shows

that the HHG signal more precisely evolves as $\langle\,\cos^4\theta\,\rangle$ [61]. The best fit of 19th harmonic

signal in CO scaled with $\langle\,\cos^4\theta\,\rangle$, giving the functional form of the angular dependence of

the HHG intensity, $I_{19}^{CO}(\theta) = .67(\pm.02) + 1.6(\pm.1)\langle\cos^4\theta\rangle$. The errorbars in Fig. 3.5 and

Fig. 3.6 represent the standard deviation of N measurements, where N = 4 in these plots.

From this fit, the HHG anisotropy of the 19th harmonic for molecules aligned parallel

or perpendicular to the drive laser polarization can be determined. Setting $\langle\cos^2\theta\rangle = 1$,

0 for parallel $(I_{\parallel})$ and perpendicular $(I_{\perp})$ molecular alignment, respectively, we obtain a

anisotropy of the 19th harmonic in CO, $I_{\parallel}/I_{\perp} = 3.4\ \pm.3$.

Similarly in N_2, the best fit of the 19th harmonic has the form, $I_{19}^{N_2}(\theta) = .18(\pm.03) +$

$4.1(\pm.1)\langle\cos^4\theta\rangle$. This form of the angular dependence of 19th intensity results in a HHG

anisotropy in N_2 of $I_{\parallel}/I_{\perp} = 24.1\ \pm4.5$. This large HHG anisotropy is consistent with

previous experiments that measured an order of magnitude larger yield from molecules in
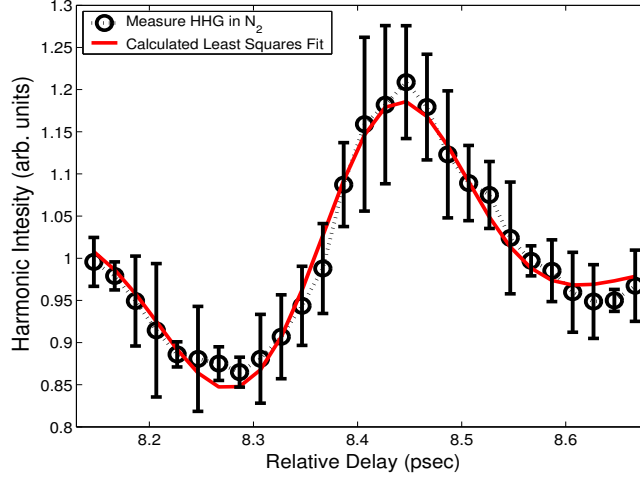
Figure 3.6: Least square fit of the delay-dependent variation in 19th harmonic signal to the generated $\langle \cos^2 \theta \rangle$ in rotationally excited N_2 (solid line). The best fit only includes the N=0,2 terms in the expansion: $I_{19}(\theta) = .18 + 4.1\langle \cos^4 \theta \rangle$.

parallel compared to perpendicular alignment [5].

Comparison of our measured HHG anisotropies with previously measured values of the ionization rate anisotropy of CO ($P_\parallel/P_\perp = 1.9$ [59]) under similar laser intensities show $\sim$ 50% larger anisotropy in the HHG yield than in the ionization rate. In N_2, the ionization rate has been measured to be approximately 4 times greater for parallel as opposed to perpendicular alignment [26]. Therefore a significant portion of the anisotropic HHG yield is due to processes other than ionization, such as the alignment-dependent recombination rate along with macroscopic propagation properties of the aligned molecular medium. In summary, we have confirmed that the delay-dependent variation in the harmonic yield is determined by the symmetry of the species HOMO. Also, we have shown that the harmonic anisotropy is significantly larger than the previously measured anisotropies of the species' ionization rates, which illustrates the need for further investigations into the angular dependence of the recombination rate and propagation properties.

3.4 Analysis of Recombination Step in N_2

In the previous section, we considered the contribution of the ionization rate anisotropy to the observed alignment dependence of HHG yield. We now explore the role of the recombination anisotropy. The recombination probability depends on both the returning electron flux and the angular dependence of the recombination rate. The rate of the returning electron flux can be examined by measuring the harmonic yield as a function of the ellipticity of the generating laser for different molecular alignments. The returning electron flux decreases with increasing ellipticity of the drive laser polarization. In the elliptically polarized laser fields, classical electron trajectories do not precisely return to the ion core. However, quantum mechanically, recombination can still occur due to the transverse extent of the returning electron wavepacket. The initial spatial distribution of the tunnel ionized wavepacket, along with the wavelength of the recolliding electron, determines the overlap of the returning electron flux with the ground-state wavefunction and, therefore, the spectral intensity of the generated harmonics. In diatomic molecules, this overlap determines the effective returning flux and depends on the orientation of the molecular axis relative to the principal (i.e. major) axis of the laser polarization. The importance of the alignment-dependent electron flux to the alignment-dependent harmonic efficiency can be characterized by comparing the ellipticity dependence of the harmonic yields for molecules preferentially aligned parallel and perpendicular to the major axis of the drive laser polarization.

3.4.1 Results

This experiment is performed using the same optical setup described previously, Fig. 3.1. The molecular gas is transiently aligned by a 85 fs pulse with an intensity of about $4\mathrm{x}10^{13}$
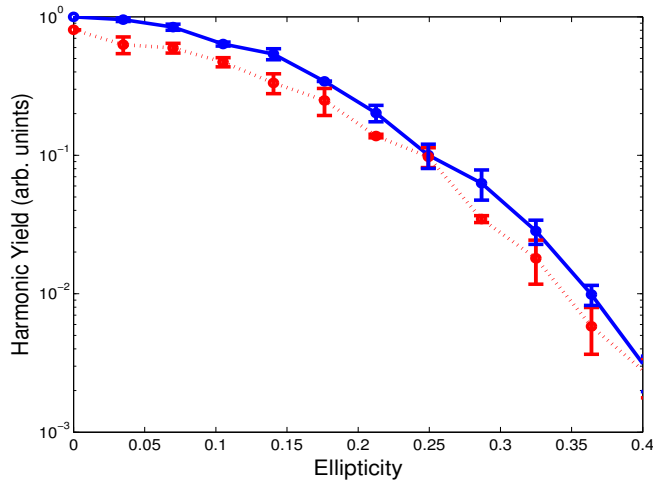
Figure 3.7: Measure of ellipticity dependence of HHG from molecules preferentially aligned parallel (solid) and perpendicular (dotted) to the fundamental laser polarization.

W/cm^2. The delay between the alignment and signal beams is held fixed at the minimum or maximum of the first full revival, ~ 8.5 ps. The ellipticity (given by $\epsilon = E_y/E_x$, where E_x and E_y are the electric field strengths of the x (principal) axis and y axis, respectively) of the pulses was adjusted using a zero order half-wave plate and zero order quarter-wave plate combination. By rotating the half-wave plate in front of the quarter-wave plate, we control the beam ellipticity while maintaining the principal polarization axis direction. This makes it possible to maintain a fixed angle between the molecular and principal laser polarization axes and minimizes the effect of the polarization dependent diffraction efficiency of the spectrometer grating. Both the alignment and signal beams are given the same polarization ellipticity, but a previous study of aligned molecules (via Coulombic explosion) showed that for small ellipticities (< 0.3) the degree of alignment is unchanged [62].

We explored the ellipticity dependence of HHG for two extreme alignment cases, parallel and perpendicular to the principal polarization axis of the drive laser. Our results

for the 21st harmonic are displayed in Fig. 3.7. Each data point represents the average of four different data runs each containing two measurements at each ellipticity value, $\pm \epsilon$, leading to eight independent measurements of the harmonic yield at each $|\epsilon|$ value. The errorbars are the standard deviation of these eight independent measurements. For the case of randomly aligned N_2 molecules, previous experiments have observed that the harmonic yield in N_2 decreases slower with increased ellipticity than the yield in Ar [63]. Additionally, N_2 molecules aligned parallel to the drive laser polarization have been shown to have an ellipticity dependence similar to that of an atom, specifically Ar [64].

In the perpendicular case, the transverse profile of both the tunnel ionized wavepacket and the ground-state electronic wavefunction reflect the two center molecular potential. Previous experiments show that for perpendicular alignment, the recolliding wavepacket is narrower than in parallel alignment due to the broader distribution at ionization. This narrow wavepacket results in a stronger decay of the harmonic signal as a function of ellipticity [65]. We, however, observe no significant differences in the ellipticity dependence of HHG for the different molecular orientations of N_2 over all the analyzed harmonic orders, q=17-23.

3.4.2   Discussion

The previous experiment showing the different ellipticity-dependent yields for parallel vs perpendicular alignments was conducted using a supersonic pulsed jet to rotationally cool the molecular sample, achieving a higher degree of molecular alignment than obtainable in our experiment [65]. In our case, the relatively low degree of alignment produces a broader angular distribution at both the aligned and anti-aligned delay times and, thus, the effect of the molecular alignment on the recolliding electron wavepacket is negligible under our experimental conditions. Therefore, the HHG signal variation observed in our experiment

is due to the angular-dependence of the ionization rate, the recombination rate, and the macroscopic propagation effects, which are considered in the next section.

3.5 Macroscopic Propagation Effects of Molecular Alignment on HHG

The previous sections have focused on the molecular alignment dependence of HHG at the single molecule, or microscopic, level. In this section, we explore the effect of molecular alignment on the propagation of the generated harmonics in the macroscopic medium. Interestingly, we observe different revival structures in the harmonic yield for different harmonic orders. The q-dependence of the alignment-dependent harmonic emission can be attributed to shifts in the pressure-dependent phase-matching curves. Our results have significant implications for experiments which utilize the harmonic yields in different orders in an attempt to probe molecular structure and dynamics.

3.5.1 Results

As indicated in the previous section, we generally observe that the harmonic yield is greater for aligned N_2 and CO molecules as compared to molecules in an anti-aligned configuration, which is seen across all harmonic orders in the spectrum. The magnitude of the alignment enhancement depends on harmonic order and the target molecule. For, example, the harmonic yield ratio for parallel:perpendicular aligned N_2 is ~ 1.5 for harmonic orders 19 and 23 at laser intensities of $2.7x10^{13}$ and $1x10^{14}$ for the alignment pulse and HHG pulse, respectively. However, this is not always the case. For example, yield ratios for parallel:perpendicular alignment as large as 3x have been observed. Even more interesting is the observation, under certain experimental conditions, of a reversal in the relative
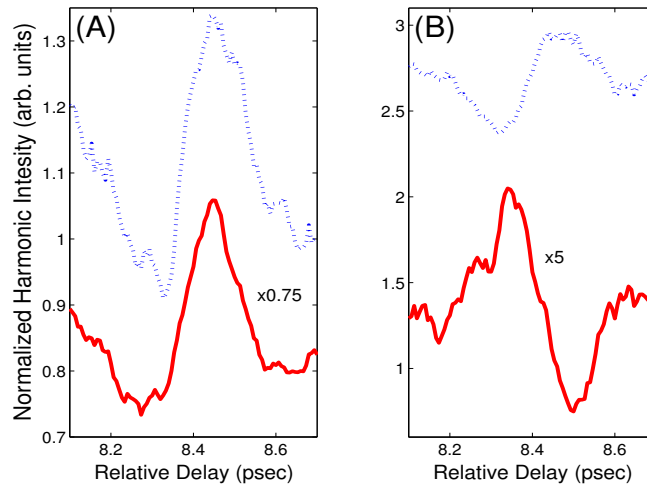
Figure 3.8: The harmonic yield generated from aligned N_2 under slightly different laser pulse chirp conditions. In (A) both the 17^{th}(blue) and 21^{st}(red) harmonics show an increased yield for the aligned vs anti-aligned configuration. However, in (B) we observe a "flip" in the harmonic revival structure in the 21st harmonic.

HHG efficiency from parallel and perpendicularly aligned samples. This reversal has been observed for some harmonic orders, but not others collected in the same laser shot.

In Fig. 3.8 (A), the yields of all harmonics decrease (increase) in unison as a function of pump-probe delay. However, as shown in Fig. 3.8 (B), under slightly different pulse chirp conditions, we observe that the yields for harmonics, q > 17, increase (decrease) as the signal in the harmonics q < 17 decrease (increase). For the data collected in Fig. 3.8 (A), the pulse chirp was set to maximize the 15th harmonic signal while in (B) it was set to maximize the 19th. This alteration of the chirp conditions slightly reduced the pulse duration for the data in (B).

This reversal is also evident in measurements of the pressure dependent phase matching curves for the different harmonic orders. Fig. 3.9 (A) shows that, for all pressures, the 17th harmonic is more efficiently generated from aligned molecules in a parallel rather than perpendicular configuration. However, Fig. 3.9(B) shows that for higher order
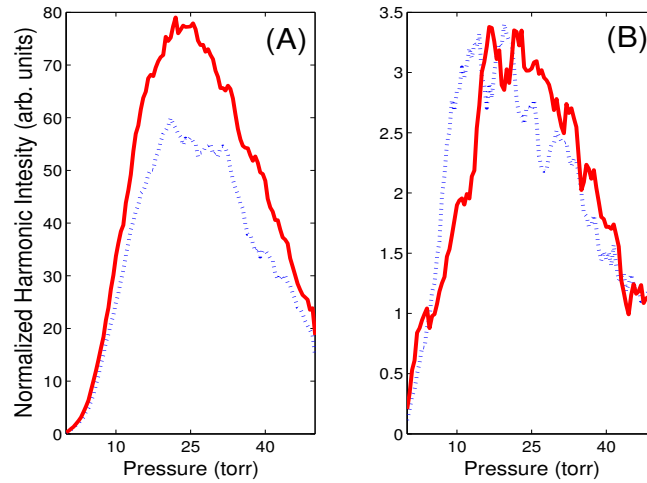
Figure 3.9: (A) Phase matching curve of 17th harmonic generated from molecules aligned parallel(solid) and perpendicular(dotted). For all pressures, the yield from the molecules aligned parallel is greater. (B) Phase matching curve for 25th harmonic. There is a range of pressures where the yield from perpendicularly aligned molecules is greater.

harmonics produced on the same laser shots, there is a range of pressures ($\sim$5-15torr) where perpendicular alignment gives a greater yield enhancement. This effect is seen for harmonics with q = 21-27. The sensitivity of this enhancement reversal to the pulse chirp as well as measurements of harmonic yield vs. pressure suggest that it is a propagation effect associated with harmonic phase-matching.

3.5.2 Discussion

We can simulate this reversal by considering the alignment dependent properties of the medium in the propagation equation, Eq. 1.2. First we consider the alignment dependence of the laser induced plasma term. The alignment dependent ionization rate modifies the free electron density (η) for the two geometries, parallel and perpendicular. The different ionization fraction changes the phase-mismatching between the fundamental and harmonic

fields, Eq. 1.5:

$$\Delta k = P \eta N_{atm} r_e \left(q\lambda - \frac{\lambda}{q} \right) - \frac{2\pi(1-\eta)Pq\Delta\delta}{\lambda} + \frac{qu_{11}^2}{4a\pi^2} \tag{3.2}$$

A larger ionization fraction increases the dispersion due to the plasma, resulting in a higher gas pressure needed to phase match the HHG process. Litvinyuk et al. observed a 1.23 times stronger ion signal for the N_2 molecules preferentially aligned along the polarization of the ionizing laser field leading to an expression of the angular dependent ionization rate for aligned N_2 molecules, [15]:

$$I(\theta) = .22 + .78\langle \cos^2 \theta \rangle \tag{3.3}$$

The ionization anisotropy is intensity-independent for intensities under the saturation threshold [57, 66]. Additionally, the laser parameters of the HHG pulse in our experiment are on the same order as the ionizing laser parameters utilized in Litvinyuk et al. (35 fs pulse with intensity of $1\text{x}10^{14}$ W/cm^2 compared to 40 fs pulse at $2\text{x}10^{14}$ W/cm^2, respectively) and, therefore, we use Eq. 3.3 to predict the ionization enhancement from molecules aligned parallel as opposed to perpendicular to the HHG laser polarization.

We determined the range of molecular alignment obtained in the fiber by running quantum rigid-rotor simulation for our experimental conditions. Based on these simulations, we calculate the minimum and maximum $\langle \cos^2 \theta \rangle$ values to be .44 and .57. Note that in this simulation the $\langle \cos^2 \theta \rangle$ were averaged in the plane of the driving laser polarization, thus in this case, $\langle \cos^2 \theta \rangle = .5$ for randomly oriented molecules. This was done to match the experiment detailed in Litvinyuk et al. under our experimental conditions. Using Eq. 3.3 for the simulated range of $\langle \cos^2 \theta \rangle$ for our experimental parameters, we calculate a

factor of 1.19 increase in the ionization from molecules preferentially aligned parallel as opposed to perpendicular to the drive laser polarization.

Next, we consider the difference in the $\Delta\delta$ for parallel and perpendicular alignment. Recall that $\Delta\delta$ is the difference in the index of refraction at the fundamental and harmonic frequencies. The index of refraction of a molecular gas is a function of the anisotropic polarizability and the molecular alignment. It can be evaluated from [19]:

$$n^2(\theta) \approx 1 + \frac{N}{\epsilon_0}(\alpha_\perp + \Delta\alpha\langle\cos^2\theta\rangle) \tag{3.4}$$

where $\alpha_\perp$ is the component of the polarizability perpendicular to the molecular axis and $\Delta\alpha \equiv \alpha_\parallel - \alpha_\perp$ is the polarizability anisotropy. For N_2 at 800 nm, $\alpha_\parallel$ and $\alpha_\perp$ are approximately equal to their static field values of $\alpha_\parallel = 14.8$ and $\alpha_\perp = 10.2$. Thus, for the range of $\langle\cos^2\theta\rangle$ values obtained in the experiments described here, the difference in the index of refraction for the two alignments at the fundamental frequency is only .0014%. Of course, it is the difference in the index of refraction between the fundamental and harmonic frequencies, $\Delta\delta$, which is the important quantity. Unfortunately, we were unable to find a calculation or measurement of the wavelength dependence of $\bar{\alpha}$ in the VUV regime. However, at frequencies above the principal resonances in N_2, we would expect a relatively small difference between $\alpha_\parallel$ and $\alpha_\perp$. Assuming $\Delta\alpha = 0$ for the harmonics is likely an over estimate of the alignment dependence of $\Delta\delta$. Even so, this estimate for the change in $\Delta\delta$ has little impact on the phase matching due to the large plasma dispersion contribution, especially at high intensities and high harmonic orders. Thus, we only include the ionization anisotropy in the propagation model.

We have calculated the pressure dependent phase-matching curves from molecules
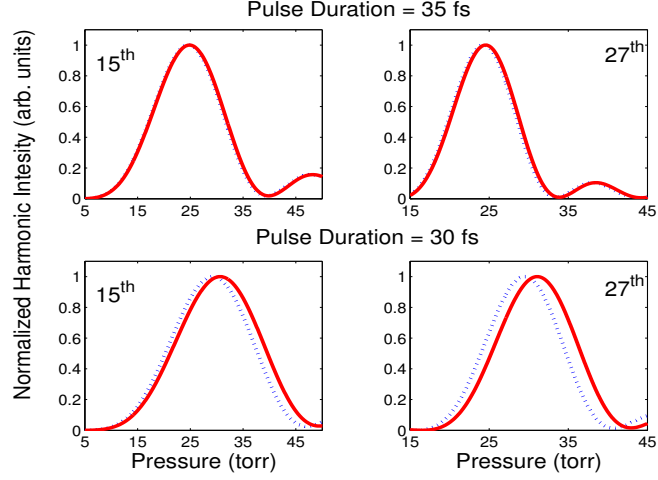
Figure 3.10: The calculated harmonic yield as a function of pressure for the 15th and 27th harmonic. The top two plots show the simulated pressure dependence of the harmonic yields generated by a 35 fs laser pulse for molecules preferentially aligned parallel (solid) and perpendicular (dotted) to the laser polarization. The bottom plot display the simulated phase matching curves generated by a 30 fs laser pulse. The increase in the free electron density in molecules preferentially aligned along the laser polarization induces a shift in the optimum phase matched pressure to higher values. The magnitude of this shift increases with harmonic order and the effect is larger for smaller generating pulse durations.

aligned parallel and perpendicular to the laser polarization using Eq. 1.9:

$$I_q = \frac{C^2}{\alpha^2 + \Delta k^2}\left(1 + e^{-2\alpha L} - 2e^{-\alpha L}\cos(\Delta k L)\right) \tag{3.5}$$

Note that Eq. 3.5 only allows us to predict the pressure dependence of the harmonic yield up to a normalization constant. Therefore, the simulated curves are normalized individually to a maximum value of 1. Fig. 3.10 shows the calculated yields of the 15th and 25th harmonics generated by laser pulses with the same energy but different pulse durations. In Fig. 3.10, we observe almost no difference in the normalized phase matching curves from molecules aligned parallel or perpendicular to the laser polarization for the harmonics generated by a 35 fs laser pulse. However, with a slightly shorter 30 fs pulse, the
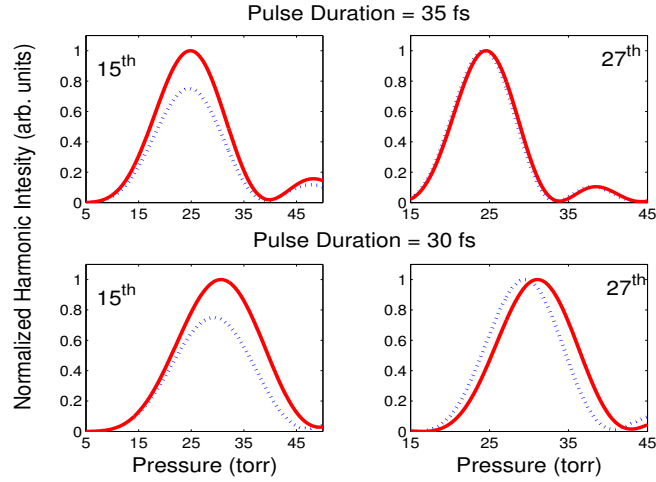
Figure 3.11: Data shown in Fig. 3.10 normalized to the relative peaks of the measured phase matching curves (Fig. 3.9)

laser intensity increases and there is a distinct shift in the optimum pressure toward higher values for all harmonic orders. The magnitude of the shift increases with harmonic order. At higher orders, the plasma dispersion term dominates the phase mis-match equation. Thus, the model predicts a significant "flip" in the 27th harmonic revival structure over the range of pressure on the rising edge of the phase matching curve, $P \leq 20$ torr. This corresponds well with the experimental data shown in Fig. 3.9.

Our primary interest is the role of phase matching in the reversal of the HHG dependence on the alignment direction for only the high order harmonics. This effect is more apparent if we scale the maximum harmonic yields in the simulation to the measured values (see Fig. 3.11). This scaling is required because the model does not incorporate the effect of the molecular alignment on the single molecule yield. As shown in Fig. 3.11 when the anisotropic single molecule yield is taken into account, the pressure shift at the lower order harmonics does not result in a reversal in the optimum molecular alignment direction.

Potentially, there are additional coupling and propagation effects that have not been incorporated into the model. In the experiment, the pulse duration was changed by physically moving the grating in the compressor. This may have caused a slight alteration in the alignment of the beams into the fiber which changed the fiber modes that were excited by the lasers. The mis-alignment could lead to mode beating which can enhance/suppress the yield of the harmonics over the propagation distance [67]. Mode beating continuously changes the intensity distribution of the beam as it propagates along the waveguide, resulting in a periodic intensity pattern that can quasi-phase match the harmonic emission. However, in hollow-core fiber waveguides, higher order fiber modes generally suffer much greater losses than the lower order modes. Additionally, our focusing conditions are implemented to optimize coupling into the EH_{11} mode, thus inducing more losses into the higher modes and reducing the effect of mode-beating. We conclude that the observed reversal in the HHG revival structure is primarily the result of the increase in the free electron density due to enhanced ionization of molecules aligned along the harmonic driving laser polarization.

3.6 Production of Even Harmonics by the Breaking of the Inversion Symmetry via 2-Color Field or Asymmetric Medium

The production of even harmonics from asymmetric molecules can be understood from a basic symmetry argument as well as semi-classical dynamics. The polarization of the medium can be expressed as a series expansion in terms of powers of the applied electric field. If the medium possesses inversion symmetry, only odd powers of E can contribute to the polarization. Thus, in a (nearly) monochromatic field only odd harmonics of the

fundamental frequency are generated. At the single molecule level, CO does not possess inversion symmetry thus even order harmonics can be generated by individual molecules. However, by definition, the even order harmonic fields from molecules with opposite orientations have opposite signs. Thus, if a well-defined phase relationship exists between the fields generated by different molecules, the even order harmonic signal will precisely cancel in the far field. Since a substantial degree of phase matching is required to observe any harmonic signal, no even harmonics are expected from a non-oriented molecular ensemble driven by a single color laser field. In an asymmetric field, i.e. an octave spanning a few cycle pulse [68] or a $1\omega + 2\omega$ superposition, the medium polarization need not possess inversion symmetry and both even and odd order harmonics can be produced.

Alternatively, we can consider the microscopic dynamics responsible for the polarization. For symmetric laser fields and molecules, matched pairs of oppositely directed electron trajectories are launched on consecutive half-cycles. The resulting harmonic fields have the same spectral amplitude but differ in sign. This leads to the destructive interference for even-order harmonics while constructive interference occurs for odd harmonics. This symmetry can be broken by driving HHG with an asymmetric laser pulse or through the use of a macroscopically non-symmetric target gas, as illustrated in Fig. 3.12.

Indeed, we observe the production of odd and even harmonics by driving the harmonic production with a two-color laser field, the combination of the fundamental with its second harmonic ($\omega + 2\omega$), see Fig. 3.13 [11, 69]. The 2-color laser field has a larger maximum value in one direction than in the opposite direction. Because of this asymmetry, the tunneling ionization probability is larger for electron ejection in one direction. In addition electrons launched into opposing trajectories expand different amounts in the field before returning to the nucleus and recombining. This leads to a phase difference between the two trajectories. If the 2ω field is very weak, we can neglect the difference in the ionization
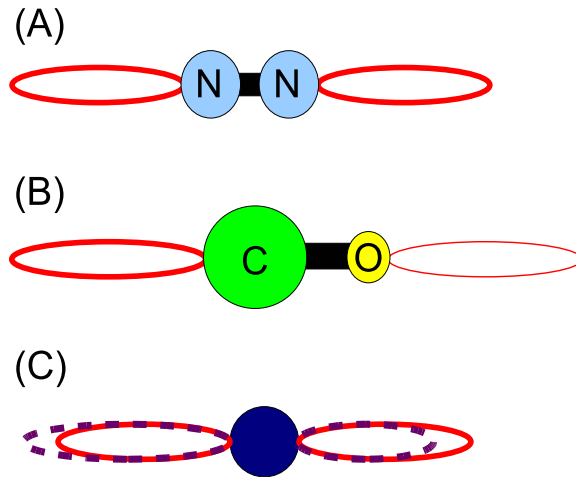
Figure 3.12: Cartoon depiction of inversion symmetry breaking in recollision electron trajectories driven by 2-color laser field. (A)-(B) Schematic of opposing electron trajectories generated by symmetric multi-cycle laser pulse from N_2 and CO, respectively (exaggerated in this diagram for clarity). The preferential ionization from the C site breaks the symmetry and results in the production of even harmonics. (C) The trajectories generated by a single color field (solid lines) and by a 2-color ($\omega + 2\omega$) field (dashed line). The latter clearly breaks the symmetry of the opposing trajectories.
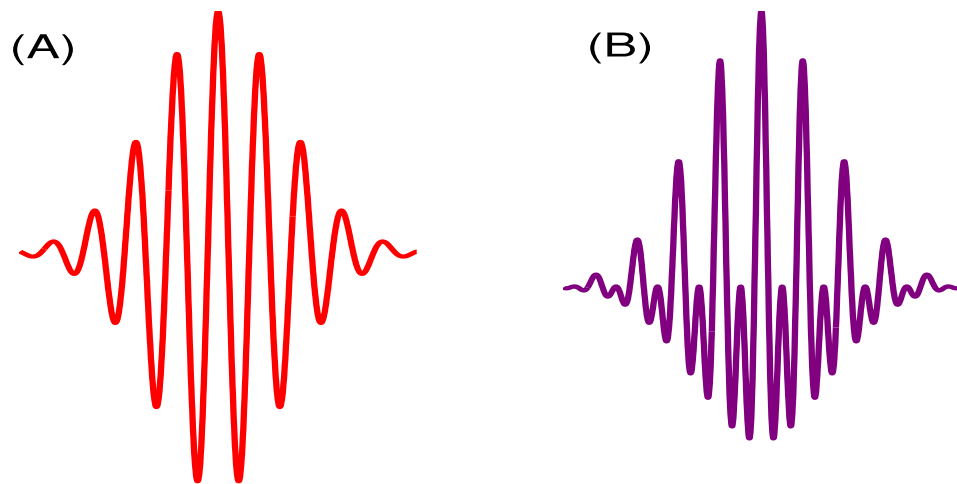
Figure 3.13: (A) Single frequency laser field (B) 2-color ($\omega + 2\omega$) laser field
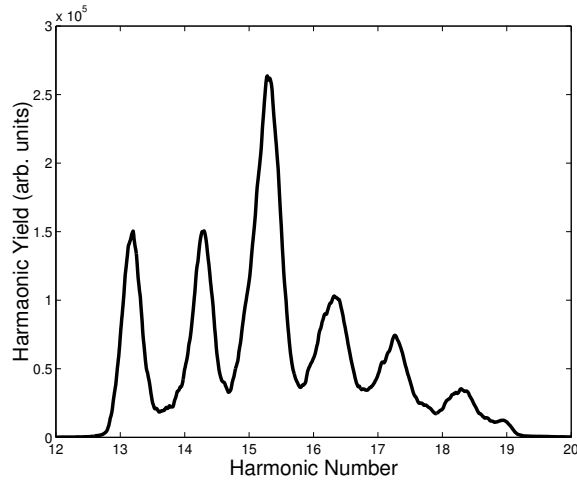
Figure 3.14: Harmonic spectrum generated in CO via a 2-color (800 nm + 400 nm) laser field. The asymmetric laser field breaks parity and leads to the production of both even and odd harmonics. Note the peaks of the spectrum experience a blue shift due to the increased ionization from the 2ω pulse.

rates from the two states of the molecule. In this case, the harmonic amplitude of the qth order, D_q, can be expressed mathematically in terms of this phase difference [70]:

$$D_q = F_q(1 - e^{i(q\pi + \Theta)}) \tag{3.6}$$

where F_q is a complex constant and Θ is the relative phase. It is apparent from Eq. 3.6 that when the phase difference is zero, as is the case for a 1ω field, $D_q = 0$ for all even q. The 2-color field can introduce a non-zero Θ which allows for the generation of both odd and even harmonics. The phase delay is a function of the ratio of intensities of the fundamental and its 2nd harmonic. Thus the relative amplitudes of the even and odd harmonics can be controlled by tuning the intensity ratio [69]. Fig. 3.14 shows the measured harmonic spectrum generated by a two-color field (800 nm + 400nm) with intensities $6\text{x}10^{13}$ W/cm^2 for the 2ω field and $1.5\text{x}10^{14}$ W/cm^2 for the fundamental field.
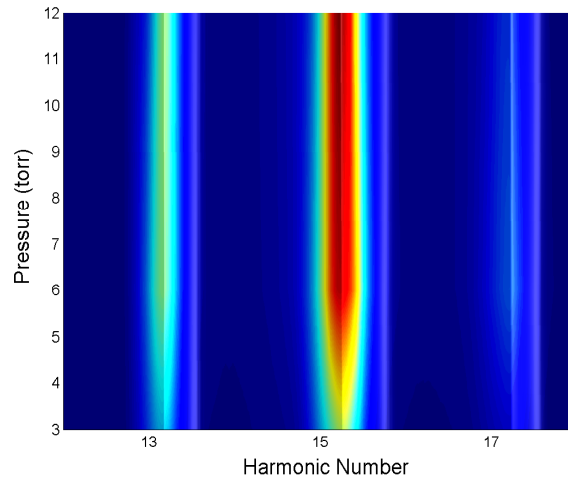
Figure 3.15: Measured HHG spectrum from randomly oriented CO in a hollow-core fiber at a laser intensity of 1×10^{14}.

For non-symmetric molecules, such as CO, the ionization anisotropy breaks the microscopic inversion symmetry and allows for the generation of even harmonics using a symmetric laser field. Fig. 3.15 is the harmonic spectrum generated in randomly oriented CO. Only odd harmonics are observed. Thus, as expected, although the production of even harmonics from single molecules may occur in a randomly oriented macroscopic sample, the coherent addition of the fields from the neighboring molecules leads to destructive interference of the even order harmonics. The even harmonics generated from single non-symmetric molecules might be observable if the molecular sample were macroscopically oriented in a "head-over-tail" fashion. Field-free orientation through the use of a coherent two-color laser excitation scheme has been predicted [71]. The scheme is similar to transient molecular alignment except that the phase-stable two-color laser Raman excitation allows for both even and odd changes in the ground-state rotational quantum number J (see Fig. 3.16). In this case, parity is no longer conserved and all molecules in a sample can be preferentially oriented in the field. Similarly to transient alignment, the molecules
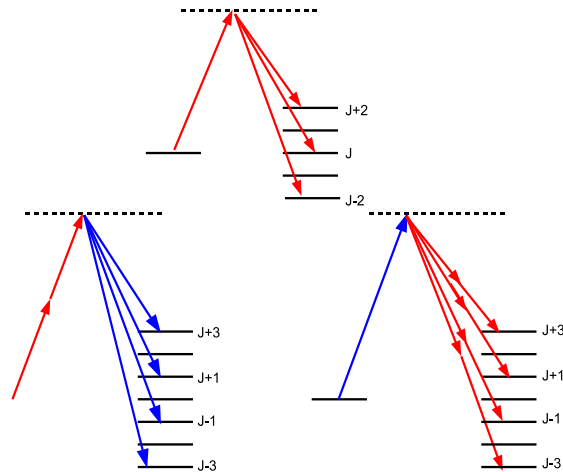
Figure 3.16: Quantum two-color excitation diagram. The 2-color ($\omega + 2\omega$) field allows for both even and odd rotational transitions.

are driven into coherent superpositions of rotational eigenstates which evolve in time and periodically return to their initial oriented geometry. However, field-free transient orientation has not yet been observed experimentally. Our attempts to measure field-free 2-color transient orientation of CO molecules through the production of even harmonics in our lab were unsuccessful. The main hurdle to achieving orientation via this scheme is the masking of the coherent orientation preserving rotational motion by the coherent orientation non-preserving alignment dynamics and the large incoherent thermal rotational motion of the molecules. Approaches to limit both of these effects are being pursued in continuing experiments [72].

3.7 Conclusion

In conclusion, we report the first measurement of harmonics generated in transiently aligned N_2 and CO in a hollow-core fiber. We observe a correlation between HHG yield and the $\langle \cos^4 \theta \rangle$ distribution in both diatomic species. From drive laser ellipticity mea-

surements, we conclude that the angular-dependence of the recolliding electron flux is negligible in our experiments. Additionally, we observe the effect of molecular alignment on the macroscopic properties of the target gas. The increased ionization from the aligned molecules shifts the peak of the phase matching curves to higher pressures particularly in the higher order harmonics. This leads to a reversal in the optimum alignment angle, from parallel to perpendicular, as a function of laser intensity for higher harmonics. This reversal effect could have severe consequences for experiments in which the reconstruction of molecular orbitals is performed using high harmonic yields from all harmonic orders assuming that only the single molecule response is responsible for the variation in the HHG yield as a function of harmonic order, see [5, 13, 29]. These experiments are typically conducted using a gas jet configuration; however, phase matching is still important for observing HHG in a jet and, thus, this reversal might be present.

Chapter 4

Role of Initial Temperature on Harmonics Generated in an Aligned Molecular Gas

4.1 Introduction

For most applications, the optimum experimental response is obtained when all aspects of the system under study are well controlled. Manipulating molecular alignment for HHG is one example. In the work presented later in this dissertation, we explore the potential to use the delay-dependent HHG modulation from transiently aligned molecules to quasi-phase match high order harmonics. The optimization of the aligning laser pulse parameters is the most obvious method for alignment improvement [73–75]. Pulses with higher intensities populate higher rotational states, producing a broader coherent distribution of J-states and a wavepacket that exhibits greater angular localization. However, high intensities can lead to multi-photon ionization, which, in the case of HHG, alters the
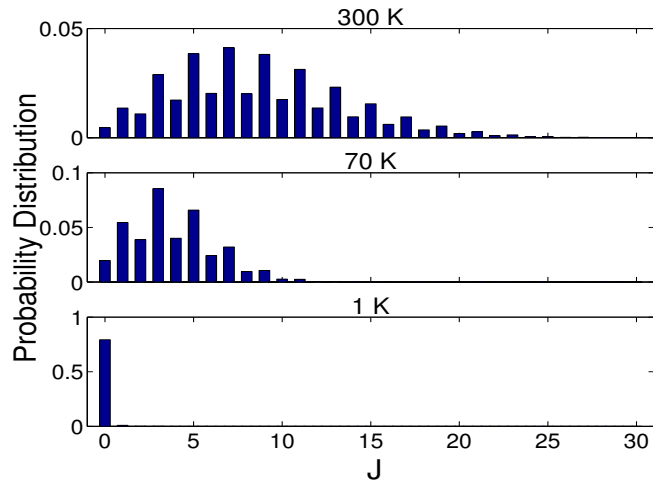
Figure 4.1: Initial J-state Boltzmann distributions for N_2 gas at 300 K, 70 K(liquid nitrogen temperature), and 1 K.

phase-matching properties of the medium and reduces the harmonic yield. The intensity can be reduced while maintaining the energy by increasing the pulse duration so long as the process is still in the impulsive limit. More sophisticated schemes can be employed to enhance alignment while minimizing ionization, such as the tailoring the temporal intensity profile of the aligning pulse (pulse shaping) [73, 76] and the use of trains of aligning [77, 78]. But these add substantial complications particularly when overlapping multiple beams in a fiber.

In addition to the dependence on laser parameters, the degree of alignment is also determined by the initial rotational temperature of the molecules. Fig. 4.1 illustrates the initial J-state populations in N_2 determined by the Boltzmann distribution at several temperatures. The J-state distribution narrows and the peak of the distribution shifts toward J=0 as the temperature decreases to 0 K. Narrow initial state distribution improves the final wavepacket coherence enabling better alignment of the ensemble of molecules due to the reduced Boltzmann averaging. Classically, for low initial temperatures, the rotation

of the molecules is dominated by the impulsive "kick" from the laser pulse. Molecular samples at finite temperatures have a distribution of initial rotational energies resulting in a different alignment times for different molecules in the ensemble [79]. For the greatest degree of alignment, the molecular sample should be initialized in a single rotational state. This can be accomplished by sufficient cooling. Interestingly, the temporal structure of the alignment revival can be strongly influenced by the rotational temperature. At low temperature and laser intensities below the tunneling ionization threshold, alignment is achieved through the coherent population of relatively few, low-J states. The difference in frequencies between these states is small, reflecting the slow rotational period at these energies. The constituent J-states remain in phase for longer periods of time and, in turn, the temporal revival structure broadens.

The initial rotational temperature of the gas sample can be reduced to sub-10 K in a gas jet configuration through supersonic expansion [80], but temperature reduction in a gas-filled hollow-core waveguide is more difficult. Collisions with the inlet tubing and the waveguide walls limit the effectiveness of cooling the molecules before they enter the fiber. In this chapter, we discuss the construction of a liquid nitrogen (LN_2) cooled fiber and examine the effect of the resulting molecular cooling on the harmonic yield.

4.2 Experimental Design

The experiment is performed using the same optical components (Michelson interferometer, lens, etc.) and spectrometer detailed in Chapter 3 (see Fig. 3.1). The only change is the hollow-core fiber waveguide vacuum cell, illustrated in Fig. 4.2. Briefly, the fiber is held by Torr-Seal epoxy inside a stainless steel pipe tee. The stainless steel tubing is attached inside a stainless steel beaker through pipe threaded holes. The beaker is filled
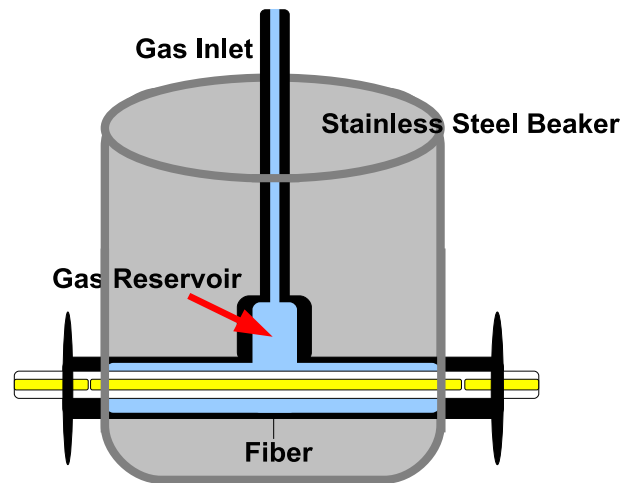
Figure 4.2: Diagram of LN$_2$ cooled fiber vacuum cell: The cell is constructed from a stainless steel beaker and stainless steel tubing. The collisional cooling is accomplished by submerging the entire fiber into a liquid nitrogen bath. The gas temperature was reduced to about 150 K.

with liquid nitrogen, submerging the interaction region of the fiber. The temperature is maintained through continuous monitoring of the LN$_2$ level. Unfortunately, the TorrSeal epoxy does not completely hold vacuum during cooling, so there is a small leak of the target gas from the high pressure fiber region into the low pressure roughing region of the chamber. This effectively doubles the backing pressure of the chamber, from 2x10^{-2} to 4x10^{-2} torr. When the fiber is returned to room temperature, the leak in the Torr-Seal is closed and the backing pressure is returned to normal value.

The external surfaces of the beaker are covered with styrofoam insulating material to reduce the heat transfer from the environment and the condensation and crystallization of water vapor. With the incorporation of the insulating material, the liquid nitrogen bath lasts about 30 minutes before the fiber is no longer submerged. The fiber is connected to the rest of the chamber by KF fittings which are heated using resistive heating tape to prevent the formation of water condensate on the input window and to prevent the
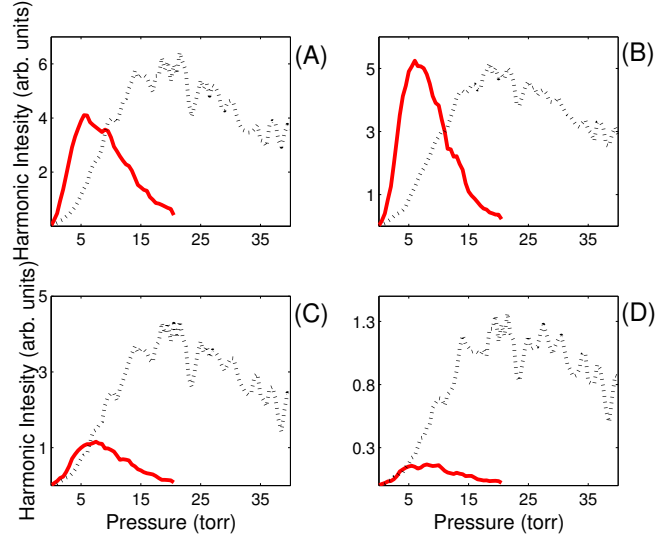
Figure 4.3: Comparison of the phase matching curves of the 19th-25th harmonics, (A)-(D) respectively, with different interaction lengths. The solid red line is the phase matching curve for a 10 cm fiber with and interaction length of 7 cm and the dotted black is the phase-matching curve for a 9 cm fiber with an interaction length of 4.5 cm. Both curves are generated using a 35 fs laser pulse of intensity $1.4x10^{14}$ W/cm^2.

Viton o-rings from reaching their failure temperature. Further details of the fiber housing construction are contained in appendix A.

The design of the vacuum cell constrains the length of the fiber to be approximately 10 cm with an interaction region of 7 cm, compared to an interaction region of 4.5 cm used in earlier work, Ch. 3. The increased interaction length shifts the peak of the phase matching curve to lower pressures, as seen in Fig. 4.3. This pressure shift might be attributed to the change in the pulse duration of the generating laser. Previous work has shown that as the pulse propagates through the gas-filled waveguide, it may undergo spectral broadening and temporal pulse compression at low pressures ($\sim$4-8 torr in Ar) [81]. However, we did not measure the pulse duration after the fiber to confirm that this is the case in our fiber configuration. The decrease in pulse duration can suppress

the ionization of the medium, reducing the plasma contribution to the phase mis-match. From Eq. 1.5, a reduced plasma dispersion term shifts the observed optimum pressure to a lower value. Additionally, for long fibers, the propagation loss is no longer negligible [43], and therefore, the pulse energy is lower at the exit of the fiber where most of the measured harmonics are generated, leading to a further reduction in the free electron density.

Lower laser intensity also results in a loss in harmonic production. First, at the single atom level, the harmonic yield increases with the ionization probability. Second, the harmonic cutoff decreases with laser intensity. For a 10 cm propagation length, the pulse energy drops by $\sim$ 10 % along the fiber [43]. At an intensity of 1.4×10^{14} W/cm^2, this power loss lowers the cutoff energy at the end of the fiber from 44 eV to 40 eV, i.e. it reduces the highest order harmonic generated from 27th to 25th. This is consistent with the data in Fig. 4.3, which shows a significant decrease in the yield for the 21st and 23rd harmonics generated in the longer fiber. The phase matching curves in Fig. 4.3 were collected utilizing the same laser (on the same day). Similar differences in the relative harmonic intensities for the two fiber lengths were observed in the data from multiple experiments. The yield loss can be corrected for by increasing the pulse energy of the driving laser field.

4.3   Results

We have compared the pressure dependence of the harmonic yield from a cold molecular sample to that produced at room temperature under the same laser conditions. The harmonic signal shown in Fig. 4.4 was produced using a single 35 fs laser pulse with an intensity of 1.6×10^{14} W/cm^2. There is a clear shift in the optimum pressure from 9 to 5 torr as the molecules are cooled. Furthermore, there is a decrease in the maximum yield
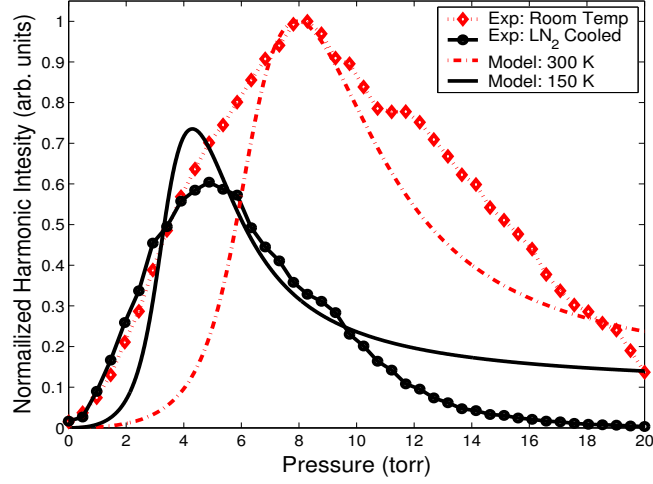
Figure 4.4: Pressure dependences of the 25th harmonic. The red diamonds and red dotted line are the measured and calculated phase matching curve of room temperature N_2 gas. The measured phase matching curve of the LN_2 cooled N_2 gas (black circles) is consistent with the calculated curve at 150 K. The peak of the experiment (calculated) phase matching curves are normalized to the maximum yield at room temperature and thus the relative heights of the calculated phase matching curves arise from the model.

obtained from the cold molecules. As discussed below, these changes are due to changes in the macroscopic properties of the medium.

We can alter the propagation equation (Eq. 3.5) to take into account the temperature dependent neutral atom number and density

$$I_q \approx \frac{C^2}{\alpha^2 + \Delta k^2} \left(1 + e^{-2\alpha L} - 2e^{-\alpha L} \cos(\Delta k L)\right), \tag{4.1}$$

where Δk is given by

$$\Delta k = P\eta N_{atm}(T)r_e \left(q\lambda - \frac{\lambda}{q}\right) - \frac{2\pi(1-\eta)Pq\Delta\delta(T)}{\lambda} + \frac{qu_{11}^2}{4a\pi^2} \tag{4.2}$$

Remember that N_{atm} is the number density of atoms per atm and, from the ideal gas law, $N_{atm} \propto 1/T$. Similarly, $\Delta\delta$ is the difference in index of refraction at room temperature

and 1 atm and, $\Delta\delta$ scales linearly with the gas density, $\Gamma = \mathrm{PN}_{atm}$ (atoms/volume):

$$\frac{\Delta\delta(T)}{\Gamma(T)} = \frac{\Delta\delta(STP)}{\Gamma(STP)} \Delta\delta(T) = \frac{\Gamma(T)}{\Gamma(STP)} = \frac{P(T)/RT}{1/(R300K)} \Delta\delta_{STP} = P(T) \left(\frac{300K}{T}\right) \Delta\delta_{STP}$$

(4.3)

The absorption coefficient, $\alpha = \sigma\rho/2$, also has a temperature dependence manifested in gas density, $\rho(\mathrm{T})$ (mass per volume), which is proportional to $\mathrm{N}_{atm}(\mathrm{T})$. The values for the ionization cross section, σ, were obtained from the Center for X-ray Optics, Berkeley Lab (www-cxro.lbl.gov) [82].

We fit the experimental data using Eq. 4.1 to determine the gas temperature in the LN$_2$ cooled fiber. The best fit was obtained for a gas temperature of 150 K. This is higher than the boiling temperature of the LN$_2$ bath ($\sim$ 77 K) but not entirely unexpected due to the poor thermal contact provided by the N$_2$ gas between the fiber and the LN$_2$ bath. The gas reservoir feeding the fiber is submerged in LN$_2$, but the Torr Seal epoxy provides some thermal contact between the glass fiber and the warm vacuum fittings that support the fiber ends. Our model produced the phase matching curve up to a normalization constant. To compare the measurements to the calculations, the peak of the experiment (calculated) curves were normalized to the maximum yield at room temperature. Therefore, the relative heights of the calculated phase matching curves arise directly from the propagation model. The model also predicts a narrower range of phase-matched pressures than measured. This discrepancy between the calculation and experiment arises from inherent limitations of the model. For computational ease, the propagation model is one-dimensional, but treats the spatial intensity variation of the laser by averaging the harmonic output over a range of ionization levels. This range is determined from the ADK calculated ionization rates at times where the intensity of the pulse is sufficient for the production of the desired harmonic order. However, this does not completely account for the experimental three
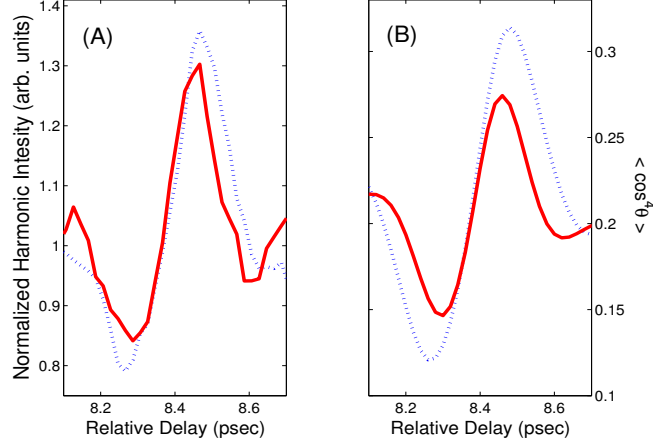
Figure 4.5: (A) The measured harmonic revivals at 300 K (solid) and 150 K (dotted). Notice the increase in the contrast ratio of the harmonic produced in a colder molecular sample. (B) Calculated $\langle \cos^4 \theta \rangle$ distribution in N_2.

dimensional beam intensity profile. However, there is qualitative agreement between the measured phase-matching curve and the model run at a temperature of 150 K.

The main objective of the temperature reduction was to increase the degree of alignment of the molecules in the fiber. Fig. 4.5 shows the intensity modulation of the 21st harmonic around the first full revival in N_2 for LN_2 cooled and room temperature molecules. The measured data curves in Fig. 4.5 (A) are the averages of four separate data sets each consists of 41 data points. The curves have been smoothed using a three point moving average filter, similar to the filter used for the alignment plots discussed in chapter 3. Fig. 4.5 (B) is the calculated $\langle \cos^4 \theta \rangle$ at 300 K and 150 K at a pump laser intensity of 4×10^{13} W/cm^2. We observe a significant increase in the contrast ratio for molecules cooled in the liquid nitrogen bath, from 1.48 to 1.65. We also see a similar increase in the calculated degree of alignment, $\langle \cos^4 \theta \rangle$, due to the increased coherence of the 150 K sample.

Along with the increase in the delay-dependent variation in the harmonic yield, other
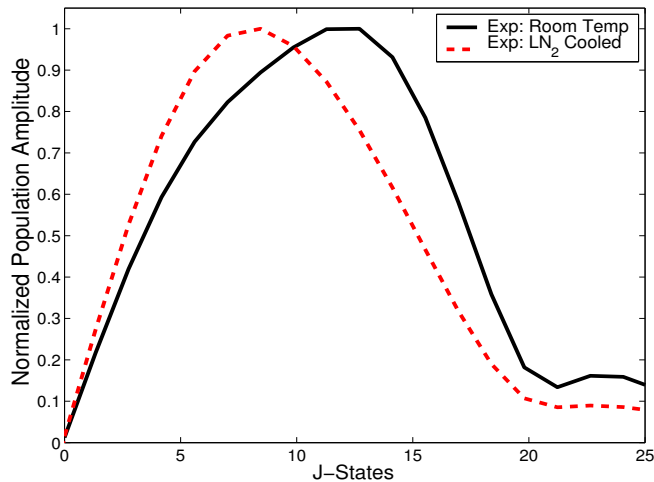
Figure 4.6: The FFT of the HHG alignment signals from Fig. 4.5.

structural features are evident in both the measured harmonic revival and the calculated $\langle \cos^4 \theta \rangle$ distribution. In particular, we measure a broader temporal revival structure from the cooled sample due to the predominant contribution of the lower J-states to the rotational wavepacket. The J-state distribution responsible for the delay dependent HHG signal can be obtained by taking the Fourier transform of the time-dependent alignment signal [59, 83]. Fig. 4.6 shows the envelope of the J-state distribution contributing to the harmonic alignment signals for room temperature (solid line) and cooled (dashed line) molecules. Only the envelope of the probability distribution can be extracted because the harmonic data were collected over only a single revival. As expected, there is a distinct shift of the peak of the distribution toward lower $|J\rangle$ values as well as a slight narrowing of the distribution for the lower initial rotational temperature.

The $|J\rangle$ state distributions of the measured harmonic signals were compared with the $|J\rangle$ distributions calculated by the rigid rotor simulation (from Fig. 4.5), see Fig. 4.7. The agreement between the measured harmonic J-state spread and the simulated J-state distribution is consistent with the propagation model that predicted that the N_2 molecules
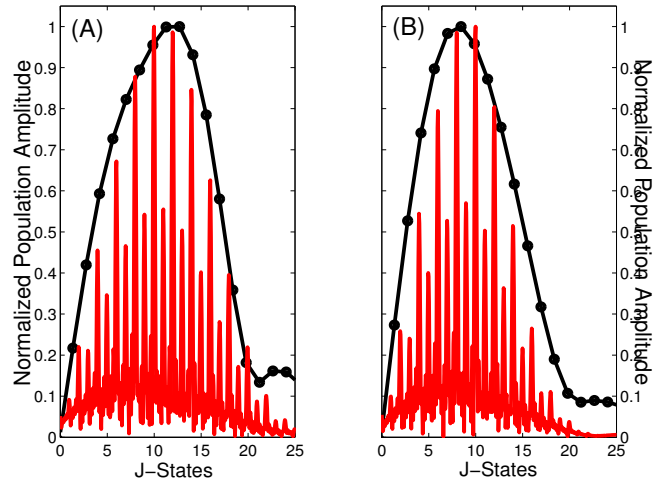
Figure 4.7: Comparison of J-state distribution from the measured delay-dependent HHG signal from aligned molecules (see Fig: 4.6) (black) and J-state the distribution computed using a rigid rotor simulation (red) for molecular gas temperature of (A) 300 K and (B) 150 K under the aligning laser conditions used in the experiments.

are cooled to $\sim$ 150 K in the LN_2 cooled fiber.

4.4   Conclusion

The purpose of cooling the hollow-core fiber waveguide was to increase the degree of alignment and, in turn, enhance the harmonic yield from the aligned sample. We designed a LN_2 cooled fiber that reduces the gas temperature to 150 K. From the cooled gas sample, we observed a 12% enhancement in the ratio of the harmonic signal generated from aligned/anti-aligned molecules. However, as seen the phase matching curves in Fig. 4.4, there was a factor of two decrease in the maximum harmonic yield negating any benefit of the increased degree of alignment for the purpose of increasing the harmonic efficiency. This yield reduction might be overcome through modifications to the cooled fiber design to reduce the absorption of the harmonics in the differential pumping region.

Chapter 5

Quasi-Phase Matching via Counter-Propagating Light

5.1 Introduction

The potential benefits of high harmonic radiation are currently limited by the available output flux. To date, most applications are restricted to intermediate harmonics (<70 eV) which have enhanced yields due to phase-matching in a hollow-core fiber [6, 7]. In this case, the flux is primarily constrained by absorption in the generating gas medium [19, 25]. For higher order harmonics, the conversion efficiency rapidly decreases. This decrease is primarily the result of ionization of the medium in the HHG process. A phase mismatch between the phase velocity of the driving laser and the generated harmonics arises from the dispersion due to the free electron plasma, which prevents efficient optical conversion by standard pressure-tuned, phase matching schemes. A significant fraction of HHG research is focused on increasing the efficiency of harmonic production at the higher photon energies where phase-matching is not obtainable.

73

Recently, quasi-phase matching (QPM) techniques have been implemented to correct for this deleterious phase mis-match by periodically adjusting the relatives phase or amplitudes of the fundamental and generated harmonics as they travel through the gas. The appropriate period for the adjustment corresponds to the optical coherence length, the distance over which the relative phase of the two waves changes by π [23]. Several methods can be employed to either periodically alter the generating properties of the medium or manipulate the fundamental laser. Past experimental work utilized specifically engineered optical fibers with a periodically modulated hollow-core diameter. The variation in the waveguide properties resulted in a periodic modulation of the driving laser intensity [8, 84]. Even small intensity variations (~ 1 %) produce significant modulations in both the phase and amplitude of the generated harmonic fields, leading to roughly an order of magnitude improvement in the conversion efficiency. The key to this scheme is matching the modulation period to twice the coherence length of the harmonic order of interest. Thus the effectiveness of this QPM scheme is limited to coherence length larger than the waveguide diameter because modulation periods shorter than the waveguide diameter do not significantly influence the intensity of the field. Additionally, the modulation period is fixed for a given fiber, limiting the range of harmonics which it can effectively quasi-phase match.

In this chapter, we discuss our results with an optical QPM scheme utilizing counter-propagating (CP) beams. QPM schemes based on CP pulses have the potential to be more convenient and less destructive than previously demonstrated QPM schemes. First, a weak counter-propagating pulse does not substantially alter the optical properties of the medium through which it propagates. Thus the non-linear properties of the medium are unaffected. Only the generating field within the volume where the two pulses overlap is modified. Additionally, the experimental apparatus (i.e. the fiber) is not permanently

altered in this optical scheme.

It has been shown that the use of a weak counter-propagating pulse can disrupt the high harmonic emission in any volume where a CP pulse and drive laser pulse are spatially and temporally overlapped [85, 86]. Interference between the counter-propagating beams crates a net field with both a standing wave component and a spatially dependent phase modulation. Because of the high nonlinearity of the HHG process, even a small spatial variation in the phase of the driving field produces a large variation in the amplitude of the harmonic fields. Moreover, this phase variation causes a significant phase mismatch suppressing the coherent harmonic production in the region of overlap between the two pulses [87].

The effect of the weak counter-propagating pulse can be understood by looking at the combined field due to the generating and CP pulses. Consider two plane waves with real amplitudes E_1 and E_2 traveling in opposite directions. If we assume E_1 is larger than E_2, then the sum of the two field can be written as [86]:

$$E_1 e^{i(kx-\omega t)} + E_2 e^{i(kx+\omega t)} = E_t(x) e^{i[kx-\omega t+\phi(x)]} \tag{5.1}$$

where the amplitude $E_t(x)$ is stationary in time, but varies spatially as:

$$E_t(x) = \sqrt{E_1^2 + E_2^2 + 2E_2 E_1 \cos 2kx} \tag{5.2}$$

and the time-independent phase modulation is given by:

$$\phi(x) = -\tan^{-1} \frac{\frac{E_2}{E_1} \sin 2kx}{1 + \frac{E_2}{E_1} \cos 2kx} \tag{5.3}$$

Both the intensity and phase modulations exhibit periods equal to one-half of the fun-

damental laser wavelength. Even for a weak CP pulse, 1/100 the intensity of the main beam, the phase variation over one period is greater than π for harmonics q > 15. Consider the microscopic phase matching over half the laser wavelength in the presence of the counter-propagating beam. The field at the qth harmonic order is [86]:

$$E_q(x,t) \sim E_o^s(x)e^{iq[kx-\omega t+\phi(x)]} \tag{5.4}$$

where E$_o$ is the fundamental field and s is the effective order of the field dependence for generating the qth order harmonic. For large enough phase modulations, the standing-wave phase factor, exp[iqϕ(x)], will dramatically disrupt the microscopic phase-matching and, essentially, turn off the coherent harmonic production.

In this chapter, we first describe our experimental exploration of the effect of a long ($\sim$ 1.6-2.3 ps) CP pulse on the harmonic yield from an intense laser pulse. Specifically, we record the high harmonic flux as a function of the energy and delay of a weaker CP pulse. The CP pulse delay determines the location in the fiber where the two pulses overlap. We find that the harmonic signal oscillates with the CP pulse delay as the overlap region is scanned through the zones which contribute constructively or destructively to the harmonic signal. We demonstrate that the oscillations in the harmonic yield can be used to extract the coherence lengths for several harmonics under different experimental conditions. From such coherence length measurements, one can determine the phase-matching conditions in the differential pumping region of the fiber. With this information one could, in principle, tailor the laser intensity, gas pressure, etc. to achieve a desired coherence length, which could then be exploited to enhance the harmonic yield via QPM. Next, we describe experiments examining a second QPM scheme for molecular gases. In particular, we examine the use of short ($\sim$ 135 fs) CP pulses to transiently align the
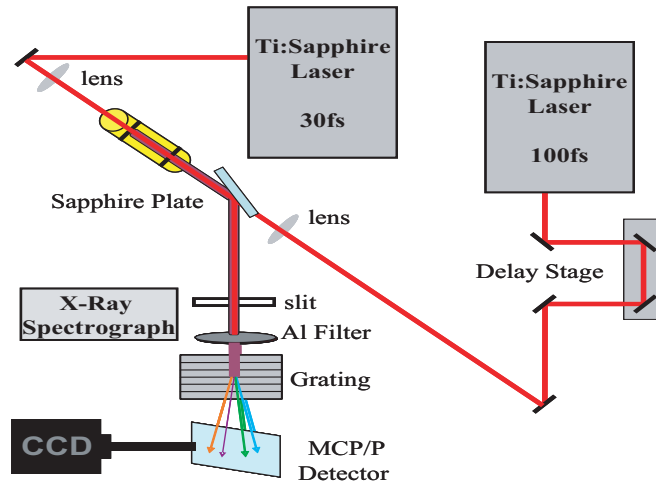
Figure 5.1: Diagram of experimental setup incorporating counter-propagating beams.

molecules along the fiber, and there by creating a spatial variation in the harmonic yield
and phase (see Chapters 1 and 3).

5.1.1 Experimental Setup

In the experiments detailed here, we employ both of the ultrafast laser systems described
in Chapter 2. The 100 fs laser system provides the counter-propagating beam and the
30 fs system is used to generate the harmonics. The laser systems are synchronized
to reduce the temporal jitter between the two pulses. Synchronization is obtained by
seeding both amplifiers with the same mode-locked pulse train and using a SRS DG535
Digital Delay/Pulse Generator to control the Q-switch timings of both laser systems. This
maintains a constant temporal delay between the two pulses. An optical delay line with a
mechanical delay stage is used to maintain the correct optical path difference between the
beams. The delay stage allows us to control the overlap location of the two beams in the
fiber and account for slow drifts associated with thermal expansion of the laser cavities
and optical tables.

The vacuum chamber configuration was altered to allow for counter-propagating beams. Fig. 5.1 illustrates the modified configuration. The hollow-core fiber waveguide is positioned at an angle relative to the spectrometer axis so that the fundamental pulse and the generated harmonics are incident on a sapphire window at an angle near 60°. Flexible bellows on each end of the fiber allow for minor tuning of this angle. The two beams are focused into opposite ends of the waveguide. The counter-propagating beam passes through the sapphire plate before entering the fiber. The sapphire window reflects about 40% of the generated harmonics into the x-ray spectrograph. S rather than P-polarized light is used for the two beams to enhance the detection efficiency of the parallel polarized harmonic beams. With this choice of polarization, ∼40% of the harmonic generating beam co-propagates with the harmonics toward the spectrometer and ∼40% of the CP beam is reflected into the chamber wall and does not enter the fiber.

When both pulses are sent into the fiber, the counter-propagating beam can propagate into the 30 fs amplifier affecting its power and decreasing the harmonic yield. This is partially corrected for by introducing a Pockels cell into the beam path between the fiber and the grating compressor for the 30 fs system. After the 30 fs pulse passes through the Pockels cell, a half-wave voltage is applied across the cell rotating the CP pulse polarization by 90°. The poor diffraction efficiency of the gratings inside the 30 fs compressor reduces the transmission of the CP pulse into the 30 fs amplifier. The presence of the CP pulse always reduces the harmonic yield, even with the Pockels cell in place. The reduction in measured yield might be due to the small portion of the CP pulse that still propagates into the 30 fs amplifier. Additionally, there is potential for the thermal CP beam to alter the properties of the sapphire window increasing the absorption of the harmonic beam by the window.

The pulse duration of the counter-propagating pulses ranges from 135 fs to 2.5 ps, as
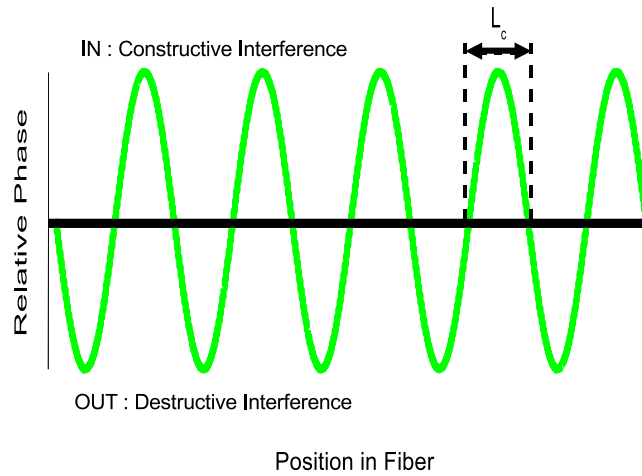
Figure 5.2: Graphic representation of the relative phases of the harmonics generated from a single pulse as a function of propagation distance in the fiber under non-optimum phase matching conditions.

measured by an interferometric cross-correlator. The pulse duration is controlled through the addition of linear chirp to the CP pulse by changing the separation between the gratings in the compressor for the 100 fs amplifier. Positive chirp is added to the pulse so that it adds to the positive chirp gained as the pulse propagates through the dispersive optical components in the beam path (i.e. mirror coatings, windows, and lens).

5.2 Probing Macroscopic Properties with a Long Counter-Propagating Pulse

In this section, we discuss the use of counter-propagating pulses to probe the macroscopic properties of the medium, specifically the coherence lengths of the generated harmonic fields. Under non-optimum phase matching conditions, the harmonics generated in conservative "zones" along the fiber add in-phase or out-of-phase with the harmonics produced in preceding zones at earlier times (see Fig.5.2). The zone width or coherence length (L_c)

is the propagation distance over which the phase of the generated harmonics changes by 180° relative to the driving laser's phase. Phase mismatch occurs when $\Delta k \neq 0$ (See Eq. 1.5), and the coherence length is defined $L_c = \pi / \Delta k$ [88]. The presence of the CP pulse of the correct duration can disrupt the harmonic production in a single, specific zone leading to an enhancement or suppression of the yield depending on the phase of the affected zone. The maximum enhancement (suppression) is obtained when the overlap region length equals the coherence length, canceling out the HHG production from an entire zone.

In our apparatus, the position of the overlap between the two pulses inside the fiber is controlled by changing the optical path length of the CP pulse. This changes the affected zone. The position of the exit from the interaction region, denoted by an overlap position $x = -1000$ in all plots, was determined by visual observation of the increased plasma density present at the intersection of the HHG generating pulse and a short CP pulse under high pressures, ~ 70 torr. Figure 5.3 shows the modulation in the yields of several harmonics as a function of the pulse overlap for a CP pulse duration of 1.6 ps. The harmonic signals in Fig. 5.3 were generated in 6 torr of Ar with pulse intensities of 3×10^{12} W/cm^2 and 3×10^{14} W/cm^2 for the CP and HHG pulses, respectively. The striking oscillations are observed in the differential pumping section of the fiber, located between 0 and 16000 μm in the plot. The absence of structure near and within the primary interaction region may be due to absorption which limits the contribution of harmonics generated earlier in the fiber [25].

Modulations in the harmonic yield due to the CP pulse are visible only when the coherence lengths of the harmonics approximately match the CP pulse length. Otherwise, the harmonic suppression within any zone is negligible compared to the total yield, and the intensity modulations disappear. This enables direct measurement of the phase matching properties of the gas for different experimental conditions. Additionally, these
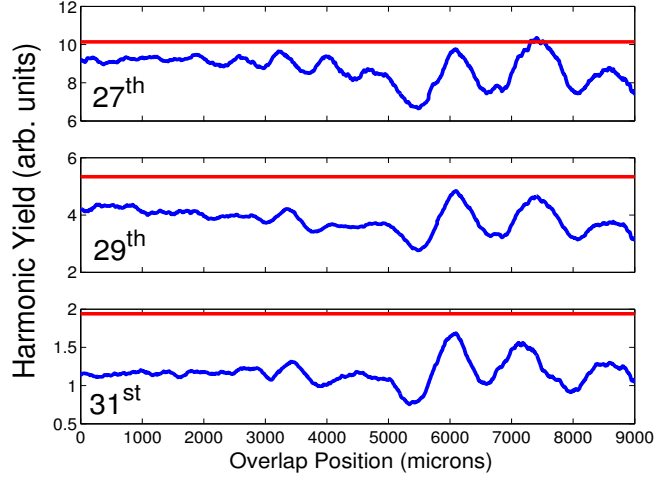
Figure 5.3: Influence of a single CP pulse on the harmonic output from 6 torr of Ar as a function of overlap position with respect to the entrance of the differential pumping section (x = 0 μm). The exit of the differential pumping region is at x= 16000 μm (off-scale). The approximate signal levels with no CP pulse are shown as red horizontal bars.

measurements can be used to gain insight into pressure gradients inside the fiber.

To demonstrate this, CP pulses of different durations were used to probe the non-linear optical properties of an Ar filled waveguide at several different pressures ranging from 6-120 torr. For probing the harmonic production at 6 torr, the CP pulse that resulted in the largest oscillation amplitudes has duration of 1.6 ps, corresponding to an overlap length of 485 μm. Due the effect of even a small CP field, the full width of the CP is used to calculate the overlap length. At higher pressures, these oscillations disappear and instead a large dip in the harmonic signal is observed at a location further from the entrance to the differential pumping section (see Fig. 5.4). To probe the optical properties at higher pressures, we employed a 2.3 ps CP pulse which corresponds to an overlap length of 700 μm. The HHG pulse energy was lowered to maintain the same intensity ratio (CP to HHG) as with the 1.6 ps CP pulse, $\sim 1\%$. Figure 5.5 shows the effect of the 2.3 ps CP pulse on the harmonic yield from 85 torr of Ar.
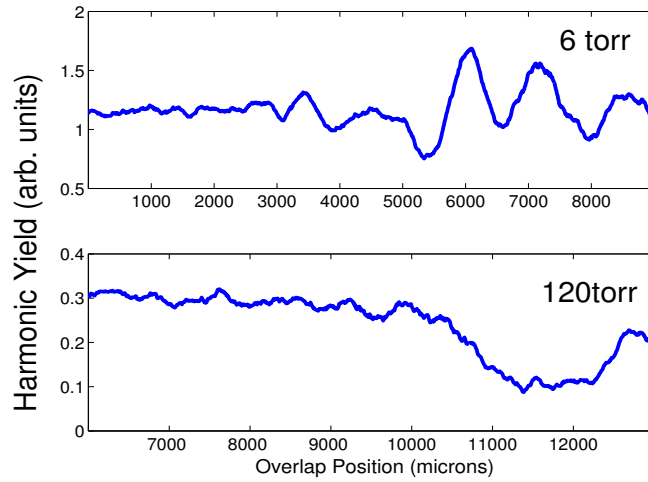
Figure 5.4: Oscillation in harmonic yield from Ar at 6 and 120 torr due to influence of 1.6 ps CP pulse. Note the different horizontal axis scales. The oscillations observed at 6 torr are not evident at 120 torr. Instead a large dip in the harmonic signal is observed in a position closer to the exit of the differential pumping region.
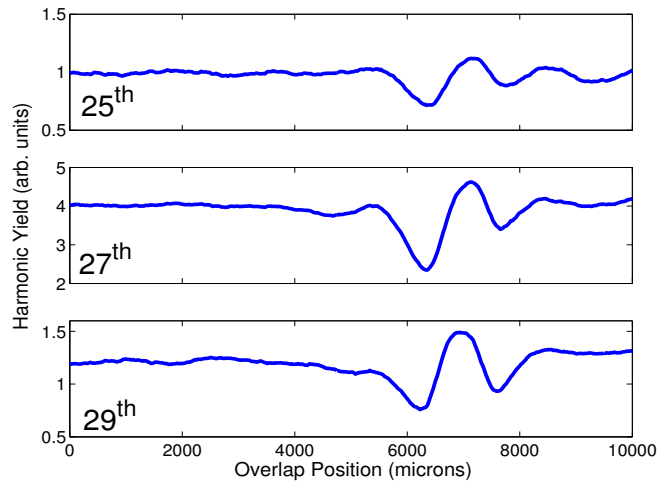
Figure 5.5: Influence of a single CP pulse on the harmonic output from 85 torr Ar for q = 25-29. The signal levels with no CP pulse (not shown) are approximately 3x larger than the baseline yield.
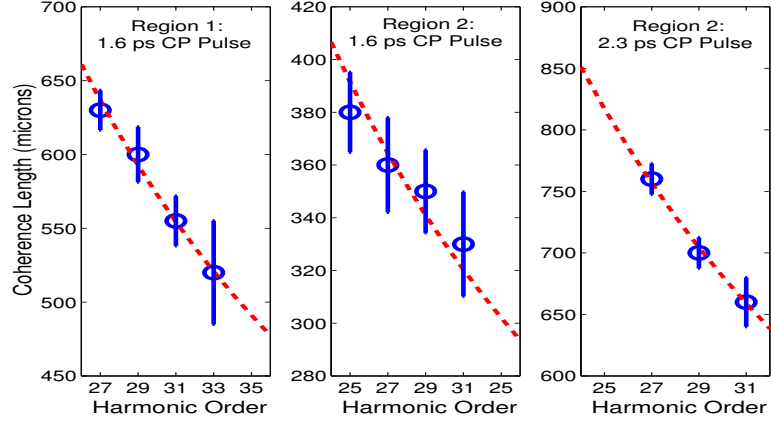
Figure 5.6: The measured coherence lengths over several harmonic orders (blue dots). The data points were computed from the data in Fig. 5.3 and 5.5 after a high pass Fourier filter and averaging over the entire range of oscillations in the region. The errorbars reflect the standard deviation of that averaging. The solid line is a least squares fit of the data in terms of the inverse of the harmonic order, (1/q).

We observe two distinct oscillatory regions, region 1 from 0-4000 μm and region 2 from 4000-9000 μm (See Fig. 5.3). The coherence length for individual harmonics can be calculated in these regions. The coherence length is equal to $\frac{1}{2}$ the oscillation period [89]. The computed coherence lengths for the measured harmonic orders are shown in Fig. 5.6. The coherence lengths are inversely proportional to Δk and, therefore, scale as 1/q for fixed pressure and ionization level. We fit the coherence length data to the equation L_c = $\frac{\pi}{\Delta k'}(1/q)$, where Δk' is the order-independent phase mis-match, using a least square fitting procedure in MATLAB. From this fit, we can determine the total phase mis-match, Δk = qΔk'. The phase mis-match over the harmonic orders q = 23-33 in each region are shown in Table 5.1.

By using the measured coherence lengths in combination with the phase-matching equation (Eq. 1.5), we have the potential to determine the local pressure inside the fiber. Additionally, the range over which the oscillation are present can give information about

Interaction Pressure (torr)	6		85
Harmonic Order	Region 1	Region 2	Region 1
23	4200	6840	3540
25	4570	7430	3840
27	4940	8020	4150
29	5300	8620	4460
31	5670	9210	4470
33	6030	9010	5080

Table 5.1: Calculated phase mis-match values, Δk, in m^{-1}.

the local pressure gradient. From the measured coherence lengths from the 27th harmonic in Fig. 5.3, we modeled the pressure gradients in region 1 and region 2 as two different linear functions. The phase mis-match (Δk) is then computed as a function of position in the fiber from the pressure gradients, which is in turn, used to determine the amplitude of the harmonic field where the total harmonic field, $E(x,t) = Ae^{i(\Delta kx - \omega t)}$, and the amplitude is defined as $\epsilon = e^{i\Delta kx}$, see Fig. 5.7 (A). The effect of the CP pulse on the harmonic yield was computed by scanning the position of a mask filter, with a width equal to the pulse overlap, over the harmonic field (black Fig. 5.7 (A)). Mathematically, this eliminated the harmonic production in the region in which the mask occupies. The resulting harmonic field is then integrated and squared to give the harmonic intensity as a function of overlap position in the fiber. The calculated modulations in the yield (Fig. 5.7 (B)) are in good qualitative agreement with the measured signal, Fig. 5.7 (C).

The harmonic signal variation in region 1 is not evident at 85 torr, thus we used the same percentage pressure drop utilized in Fig. 5.7 over the regions to determine the pressure gradients. Figure 5.8 displays both the calculated harmonic signal and the measured 27th harmonic signal from Fig. 5.5. Oscillations are observed over the same fiber location for both the measured and calculated signals. Even though our simple model does
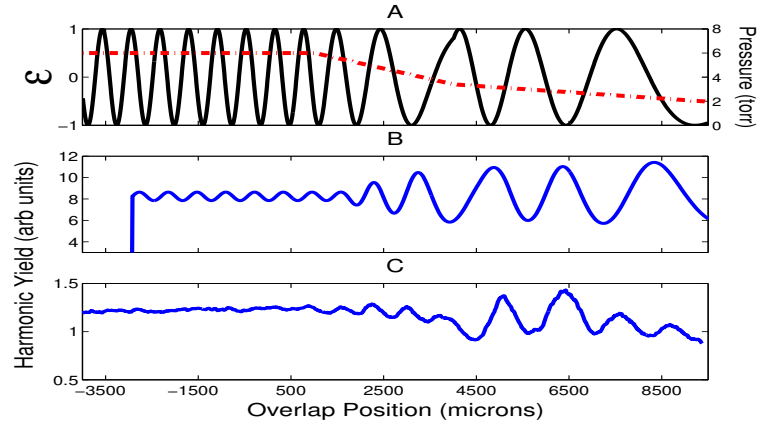
Figure 5.7: Simulated pressure inside a hollow-core capillary feed with 6 torr of Ar. (A) shows the harmonic field, $\epsilon = e^{i\Delta kx}$,(black) and the modeled pressure (red) as a function of position in the fiber. (B)-(C) display the calculated and measured harmonic yield vs overlap position, respectively.
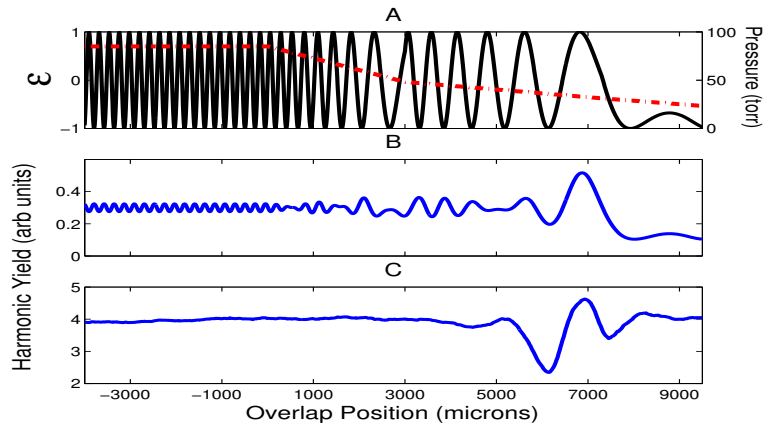

Figure 5.8: Simulated pressure inside a hollow-core capillary feed with 85 torr of Ar. The same percentage pressure drop observed in Fig. 5.7 was utilized for this case.

not fully explain the measurement, it does illustrate that the pressure gradient is non-linear inside the fiber used in our experiment and has a distinct change in slope about 3 mm inside the differential pumping region. The pressure gradients inside a capillary can be analytically determined for cases where $\gamma = 2a/L > .05$, where a and L are the capillary radius and length, respectively [90]. For the fiber used in these experiments, $\gamma \approx .01$. Also, these models are only valid under free flow conditions where the mean free path is greater than the diameter of the tube, which is not the case for pressures above 35 torr at room temperature for our fiber diameter of 150 μm. Thus, this result could lead to future explorations into the measurement of gas flow through gas-filled capillaries using HHG where analytical model are currently not viable.

Comparisons between the simulation and data at both 6 and 85 torr illustrates qualitatively that the pressure gradient is altered around 3 mm position, suggesting the non-linearity might be due to conditions specific to our fiber. An example of these conditions might be the turbulent flow at the entrance to the differential pumping region or the presence of debris or deformities in the fiber that restrict the gas flow. Previous groups have assumed a linear pressure gradient in the differential pumping region of the capillary [7, 91]. However, the results presented here show that this may not be the case.

In addition to determining local pressures, the direct measurement of the phase mis-match is necessary to enable greater control of the gas properties for the purpose of implementing an optical quasi-phase matching scheme for high order harmonics ($>$100 eV) that cannot be phase matched at any pressure due the large plasma term. To efficiently quasi-phase match along the entire length of the fiber, the QPM phase correction (K_m = $2\pi/\Lambda$, where Λ is the modulation period) must be equivalent to the phase mis-match (Δk). In region 1 for the experimental conditions detailed here, the QPM term K_m must $\sim$5000 m^{-1}, i.e. the modulation period, $\Lambda \approx 1.3$ mm. Interestingly, the modulation period
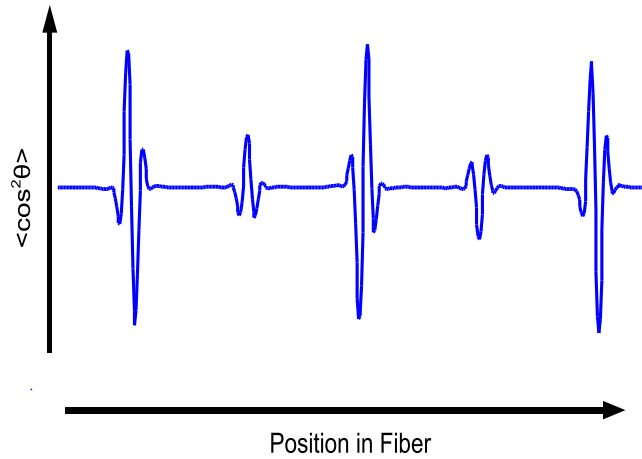
Figure 5.9: Diagram of the spatial mapping of the N_2 temporal revival structure.

we observe is on the order of the half revival period (~ 4.2 ps) for transiently aligned N_2. As described in the next section, this may lend itself to a different QPM scheme based on molecular alignment modulation along the fiber.

5.3 QPM with Short Counter-Propagating Pulse

In the previous section, we explored the use of a single long CP pulse to manipulate the harmonic yield via QPM. In this section, we describe analogues measurements utilizing a short CP pulse, $\tau \ll L_c$. In this regime, the overlap between the CP and generating pulse is too small to observe any enhancement/suppression due to the induced phase modulation. However, as described in Chapter 3, the short intense CP pulse can transiently align the molecular gas. In the CP configuration, the temporal revival structure is mapped onto a spatial axis throughout the interaction region, Fig. 5.9. While the spatial revival structure does slightly change throughout the fiber, i.e. at the higher order revivals due to the centrifugal distortion of the molecule, the time scale between the CP alignment

pulse and the harmonic production is significantly shorter than the relaxation time of the molecule. And since the harmonic efficiency from molecules aligned parallel to the laser polarization is significantly greater than that of unaligned molecules, or molecules aligned perpendicular to the laser polarization, this mapping results in a periodic modulation of the harmonic efficiency along the fiber.

Consider N_2 as an example, from the calculated $\langle\cos^2\rangle$ distribution, the spatial revival structure from rotationally excited N_2 has a periodicity, $\Lambda = cT/2 = c\pi/2B_0 = 1.3$ mm where T is the period of the full revival, and B_0 is the rotational constant in cm^{-1}. The half revival in N_2 is just as strong as the full revival thus the modulation period inside the fiber is half of the full revival period of the molecule. The correction to the phase mis-match, from Eq. 1.8, is $K_m = 2\pi m/\Lambda \approx 5000$ m^{-1} for a QPM order, m = 1. This means that the spatial alignment structure could efficiently quasi-phase match harmonics with a phase mis-match of 5000 m^{-1}. This is approximately the phase mis-match (4000 - 6000 m^{-1}) calculated in the previous section for the harmonic orders of q = 23-29 generated from a laser field of intensity 3 x 10^{14} W/cm^2 and at a pressure of 6 torr. If the coherence length and modulation period can be matched, the increased harmonic production from the aligned molecules adds constructively, resulting in an increase in the output flux.

5.3.1 Results

The effect of the short counter-propagating pulse was explored by comparing the harmonic yields before and after the short CP pulse interacts with the target gas. As illustrated in Fig. 5.10, if the signal beam passes through the fiber before the counter-propagating pulse enters the medium, harmonics are generated from a macroscopically isotropic gas. Conversely, if the signal beam enters the medium after the CP pulse has passed, then the spatially varying non-isotropic molecular distribution may affect the harmonic yield.

The role of molecular alignment was isolated by comparing the HHG yields with a short, 135 fs, CP pulse to the yields with a long, ~ 1.6 ps, CP pulse. The larger duration and lower intensity of the 1.6 ps pulse ($2.5\text{x}10^{12}$ W/cm^2) makes it ineffective for aligning N_2. Thus, any modification of the yield due to molecular alignment can only be observed from the short CP pulse interaction. In addition, we only consider CP pulse delays for which the pulse overlap occurs outside of the differentially pumped end-cap section of the fiber. Recall, that only in this region did the long CP have any affect on the harmonic yield in Ar.

To characterize changes in the harmonic yield due to the molecular angular distribution, we utilize a weighted difference, β, defined by:

$$\beta(z_0) = \frac{I_{short} - I_{long}}{I_{short} + I_{long}} \tag{5.5}$$

where I_{short} and I_{long} are the measured harmonic intensities with 135 fs and 1.6 ps CP pulses for a particular pulse overlap position z_0, respectively. Interestingly, an enhancement, albeit a small one, is observed in the harmonic passes through the fiber after the short CP pulse. Figure 5.11 shows the β values of the 27th harmonic measured for the case where the generating pulse arrives before and after the CP pulse. Similar data are observed over the entire range of harmonics measured, q = 23-33. In the "before" case, the signal beam passes through the fiber before the CP pulse enters. Thus, as expected, the length of the CP pulse has no effect on the harmonic yield and the weighted difference, $\beta \approx$ zero.

For comparison, the same experimental procedure used with N_2 as the molecular species was followed (on the same day) with atomic Ar as the target gas. Ar and N_2 have nearly identical ionization potentials and pressure dependent HHG phase matching
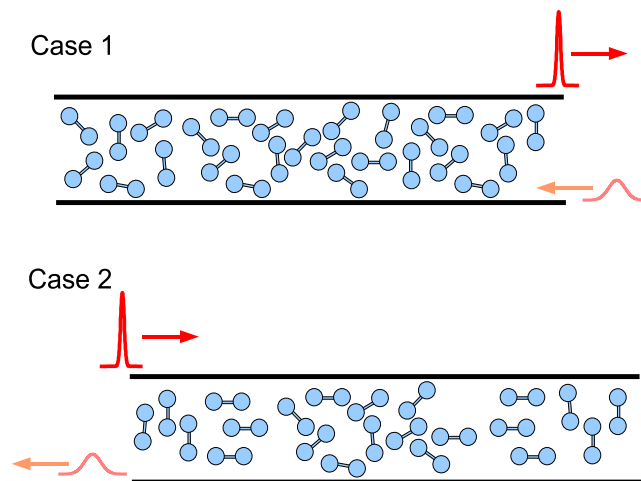
Figure 5.10: Diagram of the two situations: before and after the CP enters the fiber. Note: most of the measured harmonic output is produced in the last differential pumping section. Case 1 illustrates the situation of harmonic production before the CP pulse enters the fiber. The molecules are randomly aligned throughout the fiber and, thus, the yield is a result of just the HHG pulse. Case 2 shows the medium after the CP pulse has periodically aligned the medium along the fiber. Any effect due the molecular alignment can be measured in the harmonic yield. There is always a reduction in the observed harmonic yield with the CP pulse due its optical and thermal modification of the signal beam amplifier.
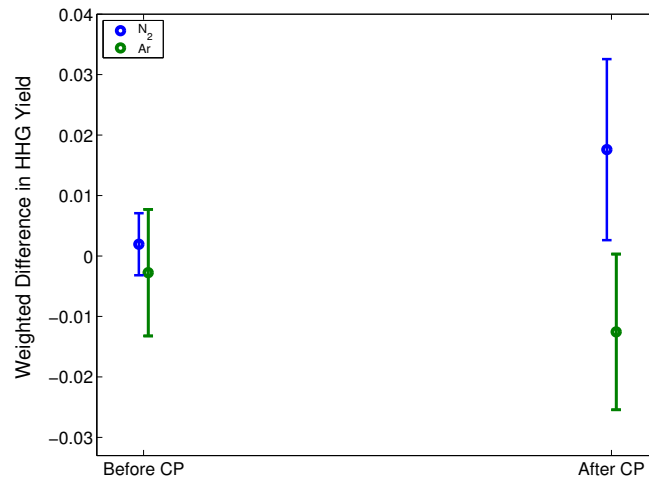
Figure 5.11: Weighted difference in the 27th harmonic yield influenced by a 135 fs and 1.6 ps counter-propagating pulses in 5 torr of Ar and N_2. The "before CP" point refers to the harmonics generated before the CP enters the fiber. The $\sim 2\%$ increase in the harmonic signal from N_2 after the CP pulses have interacted with the medium is observed over the entire range of harmonics (q = 23-33). The data points are the mean values of 400 different measurements and the errorbars are the propagation of the standard deviation of mean through the weight difference ratio. There is a clear, though slight, difference in the effect of the short CP pulse on Ar and N_2.

curves. Therefore, rotational excitation of N_2 is a likely candidate for any differences in the response of these two species to the short CP pulse. In contrast to N_2, for which there is a small ($\sim 2\%$) signal enhancement in the "after CP", the analogues yield in Ar shows a small, perhaps statistically insignificant decrease, which might be due to a slight increase in the free electron density with the presence of short CP pulse.

5.3.2   Discussion

The two percent increase in the harmonic yield after the short CP pulse is much smaller than the typical enhancements measured in other QPM schemes [8, 9]. In addition, we observed similar results over a range of harmonics that have much different coherence lengths. Thus, we explore alternative explanations for the signal enhancement which are

time (spatial)-independent. First an increase in the molecules average rotational energy, i.e. an increase in the $\langle J \rangle$ of the molecular sample, due to Raman redistribution by the short intense CP pulse can affect the macroscopic properties of the medium. The rotation generates a centrifugal force that stretches the molecule and, in turn, the average internuclear separation, which is a function of J, is altered. Classically, the change in internuclear separation can be expressed as:

$$\Delta R = \frac{L^2}{km_r R_{eq}^3} = \frac{J(J+1)\hbar^2}{km_r R_{eq}^3} \tag{5.6}$$

where k is the elastic force constant, m_r is the reduced mass and R_{eq} ($\approx 2a_0$ in N_2 where a_0 is the Bohr radius) is the equilibrium internuclear separation when the molecule is at rest. Previous studies predict an enhancement in the single molecule harmonic efficiency for increases in the internuclear separation, up to a value $\sim 12a_0$ [92]. Using the Boltzmann distribution at 300 K and a rigid rotor simulation, we evaluate the change in average energy, $\langle E_J \rangle \propto \langle J(J+1) \rangle$, due to the "kick" from the CP pulse. Using Eq. 5.6, the increase in $\langle$ J(J+1) $\rangle$ equates to an increase of 2.4×10^{-3} angstroms in the $\langle R \rangle$ value. This is an insignificant change. Pfeifer et al [92] derived the effect of internuclear separation on HHG in the extreme case of the molecular axis aligned perpendicular to the laser polarization. Of course, the molecular ensemble in our experiment has a distribution of alignments. Even in the extreme case of perfect alignment, the model predicts an increase of $\sim .2\%$ due to the average change in internuclear seperation, see Fig. 5.12. This is an order of magnitude smaller than the yield increase observed in our experiment. Thus, it is unlikely that this mechanism has a non-negligible effect to the macroscopic yield.

Another consequence of the short CP pulse is a time-independent increase in the $\langle \cos^4 \theta \rangle$ distribution known as incoherent alignment [83]. The incoherent alignment can
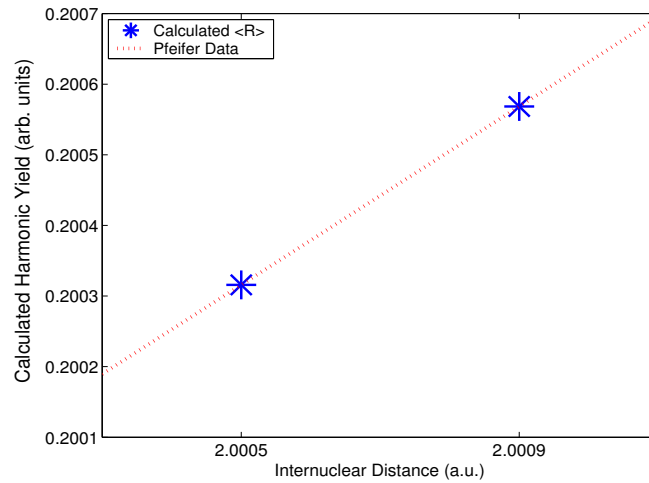
Figure 5.12: Theoretical enhancement in harmonic yield due to an increase in internuclear distance. The data points (*), calculated from the change in $\langle$ J(J+1) $\rangle$, are compared to the theoretically calculated yield as a function of internuclear separation from Pfeifer et al. [92]. The expected yield enhancement is less than 0.2%.

be understood through analysis of the laser excitation of the molecular ensemble. Initially, the $|J\rangle$-states are populated according to the Boltzmann distribution and the M values are uniformly distributed for each J-state. The interaction between the molecule and the linearly polarized aligning pulse is only dependent on the θ, not the azimuthal angle ϕ, thus M is conserved. As a result, the J-state distributions are modified, increasing $\langle J \rangle$, while leaving the M values unaffected. This leads to a time-independent cigar-shaped angular distribution aligned along the laser polarization [83].

From the quantum rigid rotor simulation between revivals, we calculate an increase in the $\langle \cos^4 \theta \rangle$ distribution from .20 to .22. Utilizing our previously measured values for the angular-dependence of harmonic generation (See Chapter 3), we predicted a harmonic enhancement due to the incoherent alignment. Simulated β values are compared to the measured data in Fig. 5.13. The simulated enhancement due to the incoherent alignment was determined by averaging the yield enhancement over several data sets. The error-
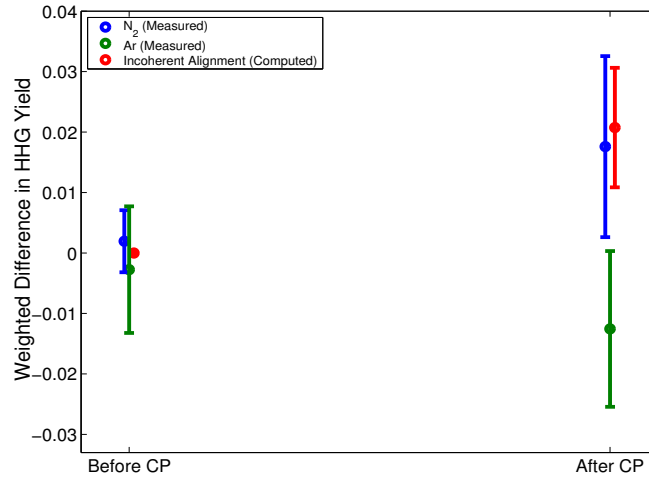
Figure 5.13: Comparison of the measured weighted difference from Fig. 5.11 and the expected effect on the harmonic yield due to incoherent alignment (squares).

bars are standard deviation about the mean. There is excellent agreement between the measured harmonic enhancement and the calculated yield increase due to the incoherent alignment.

Apparently, the observed increase in harmonic yield from the N_2 sample prepared by a short CP pulse can be attributed to the time-independent alignment. No evidence for quasi-phase matching due to modulations in the molecular alignment throughout the target gas is found. There are several potential reasons why the QPM scheme was unsuccessful. First, the alignment does not produce a perfectly periodic structure in the medium. The full and half revivals in N_2 half similar revival intensities but have reversed structure, shown in Fig. 5.14. This results in a short and long spacing between parallel alignment positions, short = 1.2 mm and long = 1.3 mm. This might not produce sufficient matching between the modulation period in the medium and the coherence length of the harmonics. Secondly, the molecular alignment gives both a signal enhancement and suppression over only a small portion of a coherence zone. This may be analogues
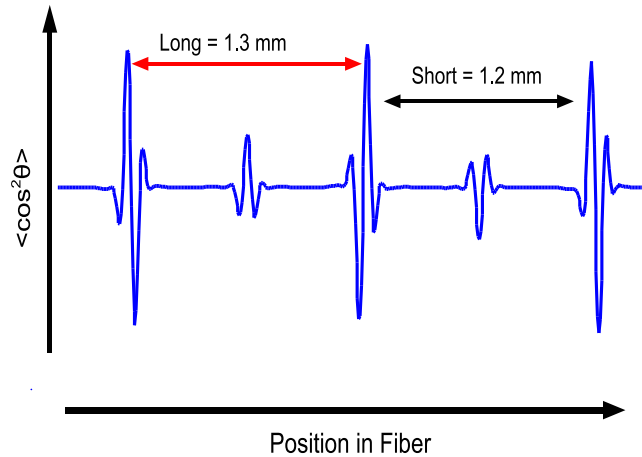
Figure 5.14: Diagram of the spatial mapping of the N_2 temporal revival structure in the fiber. Notice that in N_2, the half and full revivals have approximately the same intensity which leads to a non-periodic modulation in the molecular alignment.

to a short CP pulse canceling out the coherent harmonic emission from a small portion of the zone, which results in no observable net effect. Therefore, there might not be an integrated effect due to the periodic alignment of the medium.

Additionally, previous experiments conducted in our lab examining HHG for aligned molecules using collinear beams displayed a strong dependence of contrast ratio on the spatial overlap between the two beams. Slight mis-alignment may result in the beams coupling into different fiber modes. In these cases, there is a smaller variation in the delay-dependent harmonic yield from the transiently aligned molecules and in some cases the variation could not be observed. We scanned numerous coupling configurations but, the pump and probe beams originate from different amplifiers and propagate through different optics, therefore, it is reasonably to infer that the beams display different spatial intensity profiles. This may lead to the excitation of different waveguide modes by the two beams resulting in a reduction in the time (space)-dependent molecular alignment

experienced by the HHG generating pulse.

5.4   Conclusion

In summary, we used long counter-propagating pulses (τ = 1.6 - 2.3 ps) to probe the macroscopic non-linear-optical properties of gaseous HHG medium. The coherent harmonic production can be disrupted at locations where the CP and HHG pulses overlap. Similar to the results observed by other groups [9, 86], we observe an oscillation in the harmonic yield as a function of the position of the overlap in the fiber. The period of the oscillation corresponds to twice the coherence length of the harmonic field and, therefore, allows for the direct measure of the macroscopic phase matching properties of the medium under specific experimental conditions. In addition, we utilize the measured optical properties to qualitatively show a non-linear pressure gradient inside the fiber in our experiment. This illustrates potential to use CP pulses to probe local pressure values in a capillary.

Through probing of the phase matching properties of the medium, we were able to adjust the experimental parameters to achieve a phase mis-match of $\sim$5000 m^{-1} which corresponds to the periodicity of the time-dependent alignment revival structure in N$_2$. We attempted to implement a QPM scheme utilizing a 135 fs CP pulse to spatially map the temporal alignment structure throughout the fiber, periodically modulating the HHG efficiency of the gaseous medium. While we did not observe an effect due to the QPM scheme, we did see a small 2% enhancement in the harmonic yield due to the incoherent alignment induced by the CP pulse.

Chapter 6

Conclusion

In this dissertation, we discuss the development of a coherent VUV source based on optical high harmonic generation of intense laser pulses in a gas-filled hollow-core waveguide. Also detailed are several experiments exploring high harmonic generation from molecular gas targets. In Chapter 3, we report the first measurement of HHG from preferentially aligned molecules in a hollow-core fiber. Comparison of simulated time-dependent molecular angular distributions with the delay-dependent yields from transiently aligned N_2 and CO indicates that the HHG from both species scales as $\langle \cos^4 \theta \rangle$. We extract a functional form for the angular-dependence of the HHG yield and predict that the 19th harmonic signal should be 4x and 24x larger for molecules aligned parallel as opposed to perpendicular to the drive laser polarization in CO and N_2, respectively. Investigations into the alignment-dependence of the recolliding electron flux were conducted by measuring the harmonic yield from parallel and perpendicularly aligned molecules as a function of drive laser ellipticity. The results indicate that the angular-dependence of the recolliding electron flux is negligible in our experiments.

The harmonic yield is a function of the single molecule response as well as the macro-

scopic propagation effects. We explored the effect of molecular alignment on the macro-scopic properties of the medium and observed a reversal in the optimum alignment angle, from parallel to perpendicular, in the higher order harmonics as a function of laser in-tensity. While this reversal has previously been explained in terms of the single molecule response, we show that this reversal is likely due to the increase in the ionization rate for the aligned molecules. The increased free electron density shifts the peak of the phase matching curves to higher pressures particularly in the higher order harmonics. This reversal could severely impact experiments which assume that only the single molecule re-sponse is responsible for the alignment-dependent variation in the HHG yield as a function of harmonic order.

Chapter 4 details experiments focused on improving the harmonic efficiency by in-creasing the degree of alignment via reduction in the initial rotational temperature of the molecular sample. We constructed a LN_2 cooled fiber that reduces the gas temperature in the waveguide from 300 K to 150 K. The cooled sample gives a 12% improvement in the contrast ratio of the harmonic signal generated from N_2 molecules aligned par-allel/perpendicular to the drive laser polarization. However, the overall harmonic yield decreases by a factor of 2, apparently due to increased absorption. This negates any enhancement in the harmonic efficiency due to the increased degree of alignment.

The experiments described in Chapter 5 explore quasi-phase matching (QPM) schemes using counter-propagating (CP) pulses. First, long counter-propagating pulses ($\tau \geq 1.6$ ps) were utilized to probe the macroscopic non-linear-optical properties of the gaseous HHG medium, specifically, allowing for the direct measurement of the coherence lengths of the harmonic fields. The combination of the coherence length measurements and the development of a propagation model enabled an analysis of the pressure gradient in the differential pumping region of the fiber. Our analysis suggests an unexpected non-linear

pressure gradient within the waveguide. Apparently, HHG might be used as a tool to directly measure the pressure gradients within capillaries.

In addition to the potential use for determining local pressures inside capillaries, the measurement of the phase matching properties of the medium might enable the control of experimental parameters to achieve a desired phase mis-match. For example, we describe a QPM scheme to periodically modulate the HHG efficiency in a molecular medium. Specifically, we used 135 fs CP pulses to spatially map the temporal alignment structure along the fiber. The gas pressure in the fiber was adjusted to give a coherence length comparable to the induced molecular alignment revival structure. While we did observe a small 2% enhancement in the harmonic yield, it was probably not due to the QPM effect. Instead, the enhancement was shown to be consistent with the time-independent, incoherent alignment induced by the CP pulse.

In summary, we have demonstrated the ability to use molecular dynamics, i.e. transient molecular alignment, to affect the HHG signal generated in a waveguide. We have shown the importance of these same dynamics on the propagation properties of the medium and on the resulting harmonic yield. The reversal observed in Chapter 3 might allow for the selective enhancement of higher order harmonics by controlling the macroscopic phase-matching properties of the aligned molecular gas. Also, our demonstration of a liquid nitrogen cooled fiber opens the door for future experiments utilizing rotationally cold molecules over an extended interaction distance in a waveguide. For an example, this could increase the degree of alignment obtained in a fiber, possibly improving measurements of molecular dynamics using HHG. More generally, the experiments presented in this dissertation contribute to the general understand of the effect of molecular dynamics on the optical properties of the gaseous medium and the results could potentially influence both technology and fundamental science.

Bibliography

[1] A. McPherson, G. Gibson, H. Jara, U. Johann, T. S. Luk, I. A. McIntyre, K. Boyer, and C. K. Rhodes. Studies of multiphoton production of vacuum-ultraviolet radiation in the rare gases. *J. Opt. Soc. Am. B*, 4:595, 1987.

[2] P. M. Paul, E. S. Toma, P. Breger, G. Mullot, F. Auge, Ph. Balcou, H. G. Muller, and P. Agostini. Observation of a train of attosecond pulses from high harmonic generation. *Science*, 292:1689, 2001.

[3] Ch. Spielmann, N. H. Burnett, S. Sartania, R. Koppitsch, M. Schnurer, C. Kan, M. Lenzner, P. Wobrauschek, and F. Krausz. Generation of coherent x-rays in the water window using 5-femtosecond laser pulses. *Science*, 278:661, 1997.

[4] P. W. Dooley, I. V. Litvinyuk, K. F. Lee, D. M. Rayner, M. Spanner, D. M. Villeneuve, and P. B. Corkum. Direct imaging of rotational wave-packet dynamics of diatomic molecules. *Phys. Rev. A*, 68:023406, 2003.

[5] J. Itatani, J. Levesque, D. Zeidler, H. Niikura, H. Pepin, J. C. Kieffer, P. B. Corkum, and D. M. Villeneuve. Tomographic imaging of molecular orbitals. *Nature*, 432:867, 2004.

[6] A. Rundquist, C. G. Durfee III, Z. Chang, C. Herne, S. Backus, M. M. Murnane, and H. C. Kapteyn. Phase-matched generation of coherent soft x-rays. *Science*, 280:1412, 1998.

[7] C. G. Durfee III, A. Rundquist, S. Backus, C. Herne, M. M. Murnane, and H. C. Kapteyn. Phase matching of high-order harmonics in hollow waveguides. *Phys. Rev. Lett.*, 83:2187, 1999.

[8] E. A. Gibson, A. Paul, N. Wagner, R. Tobey, D. Gaudiosi, S. Backus, I. P. Christov, A. Aquila, E. M. Gullikson, D. T. Attwood, M. M. Murnane, and H. C. Kapteyn. Coherent soft x-ray generation in the water window with quasiphase matching. *Science*, 302:97, 2003.

[9] X. Zhang, A. L. Lytle, T. Popmintchev, X. Zhou, H. C. Kapteyn, M. M. Murnane, and O. Cohen. Quasi-phase-matching and quantum-path control of high-harmonic generation using counterpropagating light. *Nat. Phys.*, 3:270, 2007.

[10] P. Salieres, B. Carre, L. Le Deoff, F. Grabon, G. G. Paulus, H. Walther, R. Kopold, W. Becker adn D. B. Milosevic, A. Sampera, and M. Lewenstein. Feynman's path-integral approach for intense-laser-atom interactions. *Science*, 292:902, 2001.

[11] T. Zuo, A. D. Bandraum, M. Ivanov, and P. B. Corkum. Control of high-order harmonic generation in strong laser fields. *Phys. Rev. A*, 51:3991, 1995.

[12] R. Bartel, S. Backus, E. Zeek, L. Misoguti, G. Vdovin, I. P. Christov, M. M. Murnane, and H. C. Kapteyn. Shaped-pulse optimization of coherent emission of soft x-rays. *Nature*, 406:406, 2000.

[13] R. Torres, N. Kajumba, Jonathan G. Underwood, J. S. Robinson, S. Baker, J. W. G. Tisch, R. de Nalda, W. A. Bryan, R. Velotta, C. Altucci, I. C. E. Turcu, and J. P. Marangos. Probing orbital structure of polyatomic molecules by high-order harmonic generation. *Phys. Rev. Lett.*, 98:203007, 2007.

[14] X. Zhou, R. Lock, W. Li, N. Wagner, M. M. Murnane, and H. C. Kapteyn. Molecular recollision interferometry in high harmonic generation. *Phys. Rev. Lett.*, 100:073902, 2008.

[15] P. B. Corkum. Plasma perspective on strong-field multiphoton ionization. *Phys. Rev. Lett.*, 71:1994, 1993.

[16] M. Lewenstein, P. Salières, and A. L'Huillier. Phase of the atomic polarization in high-order harmonic generation. *Phys. Rev. A*, 52:4747, 1995.

[17] P. Salières, P. Antoine, A. de Bohan, and M. Lewenstein. Temporal and spectral tailoring of high-order harmonics. *Phys. Rev. Lett.*, 81:5544, 1998.

[18] M. Lewenstein, Ph. Balcou, M. Yu Ivanov, A. L'Huillier, and P. B. Corkum. Theory of high-harmonic generation by low-frequency laser fields. *Phys. Rev. A*, 49:2117, 1994.

[19] R. A. Bartels, A. Paul, H. Green, H. C. Kapteyn, M. M. Murnane, S. Backus, I. P. Christov, Y. Liu, D. Attwood, and C. Jacobsen. Phase modulation of ultrashort light pulses using molecular rotational wave packets. *Science*, 297:013903, 2002.

[20] E. Takahashi, Y. Nabekawa, M. Nurhuda, and K. Midorikawa. Generation of high-energy high-order harmonics by use of a long interaction medium. *J. Opt. Soc. Am. B*, 20:158, 2003.

[21] A. L'Huillier, K. J. Schafer, and K. C. Kulander. Higher-order harmonic generation in xenon at 1064 nm: The role of phase matching. *Phys. Rev. Lett.*, 66:2200, 1991.

[22] W. F. Chan, G. Cooper, X. Guo, G. R. Burton, and C. E. Brion. Absolute optical oscillator strengths for the electronic excitation of atoms at high resolution. iii the photoabsorption of argon, krypton, and xenon. *Phys. Rev. A*, 46:149, 1992.

[23] J. A. Armstrong, N. Bloembergen, J. Ducuing, and P. S. Pershan. Interactions between light waves in a nonlinear dielectric. *Phys. Rev.*, 127:1918, 1962.

[24] J.-P. Meyn and M. M. Fejer. Tunable ultraviolet radiation by second-harmonic generation in periodically poled lithium tantalate. *Opt. Lett.*, 22:1214, 1997.

[25] E. Constant, D. Garzella, P. Breger, E. Mével, Ch. Dorrer, C. Le Blanc, F. Salin, and P. Agostini. Optimizing high harmonic generation in absorbing gases: Model and experiment. *Phys. Rev. Lett.*, 82:1668, 1999.

[26] I. V. Litvinyuk, K. F. Lee, P.W. Dooley, D. M. Rayner, D. M. Villeneuve, and P.B. Corkum. Alignment-dependent strong field ionization of molecules. *Phys. Rev. Lett.*, 90:233003, 2003.

[27] B. Zimmermann, M. Lein, and J.M. Rost. Analysis of recombination in high-order harmonic generation in molecules. *Phys. Rev. A*, 71:033401, 2005.

[28] C. Vozzi, F. Calegari, E. Benedetti, J.P. Caumes, G. Sansone, S Stagira, M. Nisoli, R. Torres, E. Heesel, N. Kajumba, J.P. Marangos, C. Altucci, and R. Velotta. Controlling two-center interference in molecular high harmonic generation. *Phys. Rev. Lett.*, 95:153902, 2005.

[29] S. Patchkovskii, Z. Zhao, T. Brabec, and D. M. Villeneuve. High harmonic generation and molecular orbital tomography in multielectron systems: Beyond the single active electron approximation. *Phys. Rev. Lett.*, 97:123003, 2006.

[30] T. Kanai, E. J. Takahashi, Y. Nabekawa, and K. Midorikawa. Observing molecular structure by using high-order harmonic generation in mixed gases. *Phys. Rev. A*, 77:041402, 2008.

[31] J. Itatani, D. Zeidler, J. Levesque, M. Spanner, D. M. Villeneuve, and P. B. Corkum. Controlling high harmonic generation with molecular wave packets. *Phys. Rev. Lett.*, 94:123902, 2005.

[32] H. Stapelfeldt and T. Seideman. Colloquium: Aligning molecules with strong laser pulses. *Rev. Mod. Phys.*, 75:543, 2003.

[33] J. Ortigoso, M. Rodríguez, M. Gupta, and B. Friedrich. Time evolution of pendular states created by the interaction of molecular polarizability with a pulsed nonresonant laser field. *J. Chem. Phys.*, 110:3870, 1999.

[34] R. Velotta, N. Hay, M.B. Mason, M. Castillejo, and J. P. Marangos. High-order harmonic generation in aligned molecules. *Phys. Rev. Lett.*, 87:183901, 2001.

[35] V. Kumarappan, C. Z. Bisgaard, S. S. Viftrup, L. Holmegaad, and H. Stapelfedt. Role of rotational temperature in adiabatic molecular alignment. *J. Chem. Phys.*, 125:194309, 2006.

[36] C. Z. Bisgaard. *Laser induced alignment.* PhD thesis, University of Aarhus, 2006.

[37] R. L Fork, O. E. Martinez, and J. P. Gordon. Negative dispersion using pairs of prism. *Opt. Lett.*, 9:150, 1984.

[38] W.T. Silfvast. *Laser Fundamentals.* Cambridge University Press, 1996.

[39] J. Diels and W. Rudolph. *Ultrashort Laser Pulse Phenomena.* Academic Press, Inc., 1996.

[40] K. W. DeLong, R. Trebino, and D. J. Kane. Comparison of ultrashort-pulse frequency-resolved-optical-gating for three common beam geometries. *J. Opt. Soc. Am. B*, 11:1595, 1994.

[41] R. Trebino and D. J. Kane. Using phase retrieval to measure the intensity and phase of ultrashort pulses: frequency-resolved-optical-gating. *J. Opt. Soc. Am. A*, 10:1101, 1993.

[42] X. Zhang, A. Lytle, T. Popmintchev, A. Paul, N. Wagner, M. M. Murnane, and H. C. Kapteyn. Phase matching, quasi-phase matching, and pulse compression in a single waveguide for enhanced high-harmonic generation. *Opt. Lett.*, 30:1971, 2005.

[43] E. A. J. Marcatili and R. A. Scheltzer. Hollow metallic and dielectric waveguides for long distance optical transmission and lasers. *Bell Syst. Tech. Jour.*, 30:1783, 1964.

[44] F. R. Powell, P. W. Vedder, J. F. Lindblom, and S. F. Powell. Al filters. *Optical Engineering*, 29:614, 1990.

[45] McPherson, Inc. *Instruction Manual: Model 248/310G Grazing Incidence Monochromator.*

[46] D. G. Lappas and J. P. Marangos. Orientation dependence of high-order harmonic generation in hydrogen molecular ions. *J. Phys. B*, 33:4679, 2000.

[47] M. Plummer and J. F. McCann. Orientation dependence of field ionization of the hydrogen molecular ion. *J. Phys. B*, 30:L401, 1997.

[48] A. D. Bandrauk and N. H. Shon. Attosecond control of ionization and high-order harmonic generation in molecules. *Phys. Rev. A*, 66:031401, 2002.

[49] V. R. Bhardwaj, P.B. Corkum, and D. M. Rayner. Recollision during high laser intensity ionization of c_{60}. *Phys. Rev. Lett.*, 93:043001, 2004.

[50] A. Flettner, J. Konig, M. B. Mason, T. Pfeifer, U. Weichmann, and G. Gerber. Atomic and molecular high-harmonic generation: A comparison of ellipticity dependence based on the three-step model. *J. Mod. Opt.*, 50:529, 2003.

[51] A. L'Huillier, X. F. Li, and L. A. Lompre. Propagation effects in high-order harmonic generation in rare gases. *J. Opt. Soc. Am. B*, 7:527, 1990.

[52] A. L'Huillier, P. Balcou, and L. A. Lompré. Coherence and resonance effects in high-order harmonic generation. *Phys. Rev. Lett.*, 68:166, 1992.

[53] M. B. Gaarde and K. J. Schafer. Generating single attosecond pulses via spatial filtering. *Opt. Lett.*, 31:3188, 2006.

[54] M. Y. Emelin, M. Y. Ryabikin, A. M. Sergeev, M. D. Chernobrovtseva, T. Pfeifer, D Walter, and G. Gerber. Attosecond burst and high-harmonic generation in molecular ionization by ultrashort laser pulses. *JETP Lett*, 77:212, 2003.

[55] X. Zhou, X. M. Tong, Z. X. Zhao, and C. D. Lin. Role of molecular orbital symmetry on the alignment dependence of high-order harmonic generation with molecules. *Phys. Rev. A*, 71:061801, 2005.

[56] M. J. Frisch, G. W. Trucks, H. B. Schlegel, G. E. Scuseria, M. A. Robb, J. R. Cheeseman, J. A. Montgomery, Jr., T. Vreven, K. N. Kudin, J. C. Burant, J. M. Millam, S. S. Iyengar, J. Tomasi, V. Barone, B. Mennucci, M. Cossi, G. Scalmani, N. Rega, G. A. Petersson, H. Nakatsuji, M. Hada, M. Ehara, K. Toyota, R. Fukuda, J. Hasegawa, M. Ishida, T. Nakajima, Y. Honda, O. Kitao, H. Nakai, M. Klene, X. Li, J. E. Knox, H. P. Hratchian, J. B. Cross, V. Bakken, C. Adamo, J. Jaramillo, R. Gomperts, R. E. Stratmann, O. Yazyev, A. J. Austin, R. Cammi, C. Pomelli, J. W. Ochterski, P. Y. Ayala, K. Morokuma, G. A. Voth, P. Salvador, J. J. Dannenberg, V. G. Zakrzewski, S. Dapprich, A. D. Daniels, M. C. Strain, O. Farkas, D. K. Malick, A. D. Rabuck, K. Raghavachari, J. B. Foresman, J. V. Ortiz, Q. Cui, A. G. Baboul, S. Clifford, J. Cioslowski, B. B. Stefanov, G. Liu, A. Liashenko, P. Piskorz, I. Komaromi, R. L. Martin, D. J. Fox, T. Keith, M. A. Al-Laham, C. Y. Peng, A. Nanayakkara, M. Challacombe, P. M. W. Gill, B. Johnson, W. Chen, M. W. Wong, C. Gonzalez, and J. A. Pople. Gaussian 03, Revision C.02. Gaussian, Inc., Wallingford, CT, 2004.

[57] A. S. Alnaser, C. M. Maharjan, X. M. Tong, B. Ulrich, P. Ranitovic, B. Shan, Z. Chang, C. D. Lin, C. L. Cocke, and I. V. Litvinyuk. Effects of orbital symmetries in dissociative ionization of molecules by few-cycle laser pulses. *Phys. Rev. A*, 71:031403, 2005.

[58] T Kreibich, M. Lein, V. Engel, and E. K. U. Gross. Even-harmonic generation due to beyond-born-oppenheimer dynamics. *Phys. Rev. Lett.*, 87:103901, 2001.

[59] D. Pinkham and R. R. Jones. Intense laser ionization of transiently aligned CO. *Phys. Rev. A*, 72:023418, 2005.

[60] T. Kanai, S. Minemoto, and H. Sakai. Quantum interference during high-order harmonic generation from aligned molecules. *Nature*, 435:470, 2005.

[61] S. Ramakrishna and T. Seideman. Information content of high harmonics generated from aligned molecules. *Phys. Rev. Lett.*, 99:113901, 2007.

[62] D. Pinkham. *Ultrafast Control of the Dynamics of Diatomic Molecules.* PhD thesis, University of Virginia, 2008.

[63] A. Flettner, J. Konig, M. B. Mason, T. Pfeifer, U. Weichmann, R. Duren, and G. Gerber. Ellipticity dependence of atomic and molecular high harmonic generation. *Eur. Phys. J. D*, 21:115, 2002.

[64] T. Kanai, S. Minemoto, and H. Sakai. Ellipticity dependence of high-order harmonic generation from aligned molecules. *Phys. Rev. Lett.*, 98:053002, 2007.

[65] Y. Mairesse, N. Dudovich, J. Levesque, M. Y. Ivanov, P. B. Corkum, and D. M. Villeneuve. Electron wavepacket control with elliptically polarized laser light in high harmonic generation from aligned molecules. *New J. Phys.*, 10:025015, 2008.

[66] A. S. Alnaser, S. Voss, X. M. Tong, C. M. Maharjan, P. Ranitovic, B. Ulrich, T. Osipov, B. Shan, Z. Chang, and C. L. Cocke. Effects of molecular structure on ion disintegration patterns in ionization of $o2$ and $n2$ by short laser pulses. *Phys. Rev. Lett.*, 93:113003, 2004.

[67] T. Pfeifer and M. C. Downer. Direct experimental observation of periodic intensity modulation along a straight hollow-core optical waveguide. *J. Opt. Soc. Am. B*, 24:1025, 2007.

[68] T. Brabec and F. Krausz. Intense few-cycle laser fields: Frontiers of nonlinear optics. *Rev. Mod. Phys.*, 72:545, 2000.

[69] N. Dudovich, O. Smirnova, J. Levesque, Y. Mairesse, M. Y. Ivanov, D. M. Villeneuve, and P. B. Corkum. Measuring and controlling the birth of attosecond xuv pulses. *Nat Phys*, 2:781, 2006.

[70] M. Ivanov, P. B. Corkum, T. Zuo, and A. Bandrauk. Routes to control of intense-field atomic polarizability. *Phys. Rev. Lett.*, 74:2933, 1995.

[71] M. J.J. Vrakking and S. Stolte. Coherent control of molecular orientation. *Chem. Phys. Lett.*, 27:209, 1197.

[72] T. Vogt and R. R. Jones. Personal comunications. 2007.

[73] D. Pinkham, K. E. Mooney, and R. R. Jones. Optimizing dynamic alignment in room temperature co. *Phys. Rev. A*, 75:013422, 2007.

[74] M. Leibscher, I. Sh. Averbukh, and H. Rabitz. Molecular alignment by trains of short laser pulses. *Phys. Rev. Lett.*, 90:213001, 2003.

[75] M. Leibscher, I. Sh. Averbukh, and H. Rabitz. Enhanced molecular alignment by short laser pulses. *Phys. Rev. A*, 69:013402, 2004.

[76] M. Renard, E. Hertz, S. Guerin, H. R. Jauslin, B. Lavorel, and O. Faucher. Control of field-free molecular alignment by phase-shaped laser pulses. *Phys. Rev. A*, 72:25401, 2005.

[77] K. F. Lee, I. V. Litvinyuk, P. W. Dooley, M. Spanner, D. M. Villeneuve, and P. B. Corkum. Two-pulse alignment of molecules. *J. Phys. B*, 37:L43, 2004.

[78] C. Z. Bisgaard, S. S. Viftrup, and H. Stapelfeldt. Alignment enhancement of a symmetric top molecule by two short laser pulses. *Phys. Rev. A*, 73:053410, 2006.

[79] E. Péronne, M. D. Poulsen, C. Z. Bisgaard, H. Stapelfeldt, and T. Seideman. Nonadiabatic alignment of asymmetric top molecules: Field-free alignment of iodobenzene. *Phys. Rev. Lett.*, 91:043003, 2003.

[80] Jakob Juul Larsen, Hirofumi Sakai, C. P. Safvan, Ida Wendt-Larsen, and Henrik Stapelfeldt. Aligning molecules with intense nonresonant laser fields. *J. Chem. Phys.*, 111:7774, 1999.

[81] N. L. Wagner, E. A. Gibson, T. Pompintchev, I. P. Christov, M. M. Murnane, and H. C. Kapteyn. Self-compression of ultrashort pulses through ionization-induced spatiotemporal reshaping. *Phys. Rev. Lett.*, 93:172902, 2004.

[82] Berkeley Lab Center for X-ray Optics. website: www-cxro.lbl.gov.

[83] P. W. Dooley, I. V. Litvinyuk, K. F. Lee, D. M. Rayner, M. Spanner, D. M. Villeneuve, and P. B. Corkum. Direct imaging of rotational wave-packet dynamics of diatomic molecules. *Phys. Rev. A*, 68:023406, 2003.

[84] P. M. Paul, E. S. Toma, P. Breger, G. Mullot, F. Auge, Ph. Balcou, H. G. Muller, and P. Agostini. Quasi-phase-matched generation of coherent extreme-ultraviolet light. *Nature*, 421:51, 2003.

[85] J. Peatross, S. Voronov, and Prokopovich. Selective zoning of high harmonics emission using counter-propagating light. *Opt. Exp.*, 1:114, 1997.

[86] S. L. Voronov, I. Kohl, J. B. Madsen, J. Simmons, N. Terry, J. Titensor, Q. Wang, and J. Peatross. Control of laser high-harmonic generation with counterpropagating light. *Phys. Rev. Lett.*, 87:133902, 2001.

[87] J. Peatross, M. V. Fedorov, and K. C. Kulander. Intensity-dependent phase-matching effects in harmonic generation. *J. Opt. Soc. Am. B*, 12:863, 1996.

[88] A. Paul, E. A. Gibson, X. Zhang, A. Lytle, T. Popmintchev, X. Zhou, M. M. Murnane, I. Christov, and H. C. Kapteyn. Phase-matching techniques for coherent soft x-ray generation. *IEEE Quant. Elec.*, 42:14, 2006.

[89] A. L. Lytle, X. Zhang, J. Peatross, M. M. Murnane, H. C. Kapteyn, and O. Cohen. C probe of high-order harmonic generation in a hollow waveguide geometry using counterpropagating light. *Phys. Rev. Lett.*, 98:123904, 2007.

[90] C.M. Davies and C. B. Lucas. The failure of theory to predict the density distribution of gas flow through a tube under free molecular conditions. *J. Phys. D*, 16:1, 1986.

[91] D. J. Santeler. Exit loss in viscous tube flow. *J. Vac. Sci. Technol. A*, 4:348, 1986.

[92] T. Pfeifer, D. Walter, G. Gerber, M. Yu Emelin, M. Yu Ryabikin M. D. Chernobrovtseva, and A. M. Sergeev. Transient enhancement of high-order harmonic generation in expanding molecules. *Phys. Rev. A*, 70:013805, 2004.

Appendix A

Fiber Waveguide Construction

This appendix presents the procedures used to construct the three piece fiber waveguide [6] along with several vacuum cells utilized in this dissertation. The waveguide is composed of a Polymicro Technologies polyimide coated fused silica hollow-core fiber that is held into place by a Wilmad glass capillary with an outer diameter of 1/4" and an inner diameter of $\sim$ 380 microns (.015"). The capillary is cut to size (which is determined from the sum of the desired interaction length and the 2 differential pump regions) by a diamond tipped glass saw that is located in the Sackett Lab in the Physics Building. As with most applications, the blade speed starts out slow ($\sim$3). Then after a groove is formed, the blade speed can be increased to the maximum value. Finally, the blade speed should be decreased to about half speed for the final quarter width of the capillary to ensure a smoother cut. In the glass saw, the capillary is fastened in place via a v-groove clamp. No extra padding is needed. The blade is cooled by methanol bath instead of water to reduce the sediment formation in the fiber. After the cutting is complete, the inner diameter of the capillary must be cleared out by using compressed air or a section of polyimide fiber to remove the debris.

Next, two holes are drilled into glass capillary to act as the gas inlets and signify the separation between the interaction region and the differential pumping sections, typically
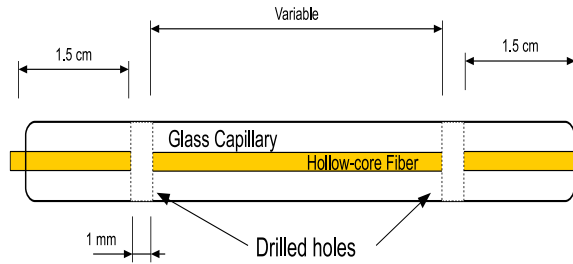
Figure A.1: Diagram of a typical 3-piece fiber.

about 1.5 cm from each end (see Fig. A.1). Before drilling, a file is used to create a level surface area. Be sure that the bit is straight as it drills through the fiber as the bits have a tendency to bend and break if their entry is crooked. The fiber is held in place using a vice that is padded with rubber. The hole is made by using a 1 mm diamond tipped drill bit that is continually cooled manually using water from a squirt bottle. The water is also used to remove the glass debris from the hole. The hole must be cleaned frequently, and thus, the typical drilling process consists of drilling a depth of 1-2 mm then removing the bit from the hole and clearing the area of debris then repeating this process until completion. The last quarter of the hole must be drilled with minimal force to reduce the blow out. Note the drill bits do degrade with use. This degrading is observed by the loss of diamonds from the tip of the bit and a noticeable slowing of the drilling process. If this degradation is noticed, the bit must be changed or diamond particles will be deposited in the hole and effectively block the site.

A diamond scribe is utilized to score a section of polyimide coated fused silica fiber which has OD = 360 microns and ID = 150 microns. This section is separated from the remainder of the fiber supply by gently pulling apart the sections. Do not twist or cut the fiber with the scribe. The fiber should be ~ 1 cm longer than the glass capillary. The fiber is then thinly coated with Torr Seal epoxy and inserted into the drilled glass capillary. After a curing period (typically 16-24 hours), short, intense laser pulses are focused onto

the polyimide coating through the drilled holes. The laser locally heats the coating of the fiber causing it to blacken and flake off. Additionally, the heating alters the properties of the fused silica making it more brittle. A sharp pick, roughly 1 mm in diameter, is then quickly and forcefully sent through the drilled hole cleaving the fused silica fiber. The cleave is far from perfect, in fact the jaggedness of the fiber edges has been observed under a microscope. This does not seem to hurt the coupling of the laser light into the fiber, although it may affect the gas pressure in the differential pumping regions (as discussed in Chapter 5). The typical coupling efficiency is 60% with a maximum observed efficiency of 68%, which is consistent with the efficiency other groups [6]. All of the tools for fiber construction are located in a single location in the CAMOS Lab in the Chemistry Building.

The simplest way to check the quality of the fiber is to shine a flashlight into one side of the fiber and see if the light propagates through to the other side. If the throughput seems low, a simple fix is to remove both ends of the fiber with the diamond scribe procedure described above. The ends of the fibers will blacken slightly with use but this is not necessarily a sign of damage. However, if the throughput is low and the blackened area of the polyimide fiber extends more than a few millimeters into the capillary, then the laser light has damaged the fiber and the entire fiber/capillary needs to be replaced. This type of damage was only observed when pulse energies greater than 800 mW were coupled into the fiber or in cases where the alignment was extremely bad.

A.1 Vacuum Cell Designs

Experiments were conducted using four different vacuum cell designs to back-fill the hollow-core fiber with the target gas. Three different incarnations were used for room temperature experiments while the fourth was utilized to reduce the gas temperature via liquid nitrogen cooling. This section will focus on the design and construction of the cells in addition to the step used to incorporate the fiber into the chambers.
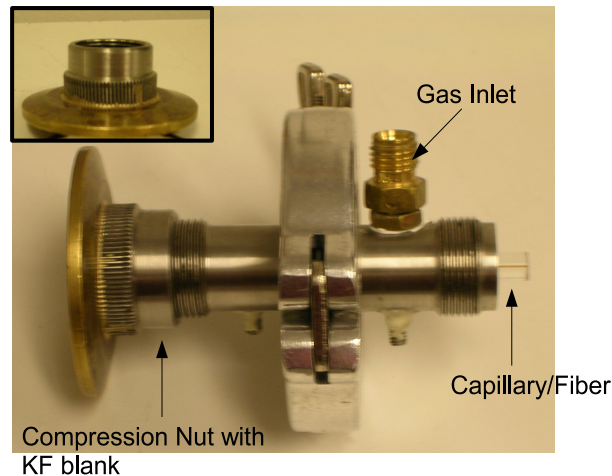
Figure A.2: Photo of the first version of fiber vacuum cell. The compression ports combine to form the gas supply cell and the gas enters the fiber through the holes between the sections of the fiber.

A.1.1 Room Temperature Vacuum Cell Designs

(A) The first version utilizes two 1/4" KF-40 compression ports, see Fig. A.2. The compression ports were modified to allow both fiber sections, inside and outside of the compression port, to be held under vacuum. This modification consists of welding a KF-40 brass blank, in which a 1/2" hole was drilled in the center, to each compression nut via an acetylene torch. Gas is fed into the cell by a Swagelok connection. The fibers are easily changed but are limited to lengths of 9-11 cm with a maximum interaction region length of ∼7 cm. Although this cell design gives the best fiber protection and allows for quick fiber changes without damaging the capillary, this version is not currently in use due to its high weight and the small range of fiber lengths that the cell can support.

(B) Blown glass cells are used as the vacuum cells in the second version (Fig. A.3). The cell was made in the now closed Glass Lab in the Chemistry Department. Torr Seal epoxy is used to affix the fiber/capillary inside the glass cell and create a vacuum seal. Swagelok connections are used to attach the fiber to the rest of the chamber and the cell
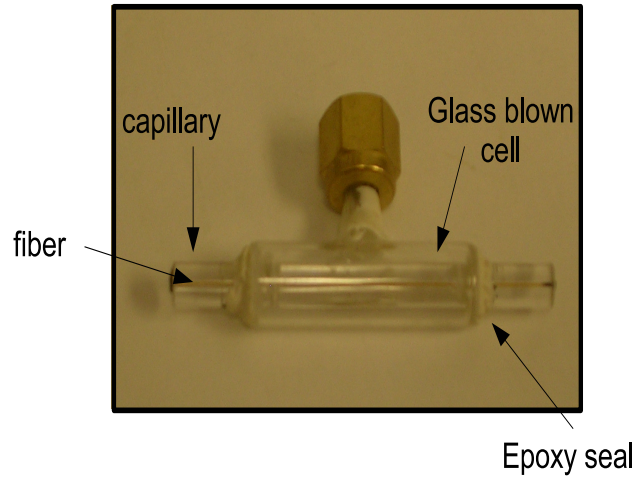
Figure A.3: Photo of a blown gas vacuum cell.

to the gas source. Teflon or nylon ferrules must be used to prevent damage to the glass cell or capillary. The gas inlet must be attached to the cell before the capillary is attached to the rest of the vacuum chamber due to the fragile nature of the glass cell. Reversing this order may lead to the breaking of the glass cell. Additionally, the removal of the glass cell from the vacuum chamber must be carried out in reverse order, disconnect capillary then gas inlet. There are currently two working glass cells with lengths of 4.5 cm and 7.3 cm which support 7 cm and 10 cm fibers, respectively. The fiber can be removed from the cell by baking the fiber and cell in a $700°$ F oven or by locally heating the Torr Seal bond with a propane torch. These heating methods cause the Torr Seal epoxy to blacken and flake off releasing the fiber from the cell. When utilizing the propane torch, the Torr Seal may have to be removed in stages. This version of the vacuum cell is light weight but is still limited to only a few different fiber lengths. This design is also extremely brittle in comparison with the other cell designs.

(C) The final version is the most versatile. The gas is fed directly into the capillary/fiber through stainless steel tubes that are Torr Sealed into the separation between the fiber sections (Fig. A.4). On the other end, the steel tubes are soldered to a brass
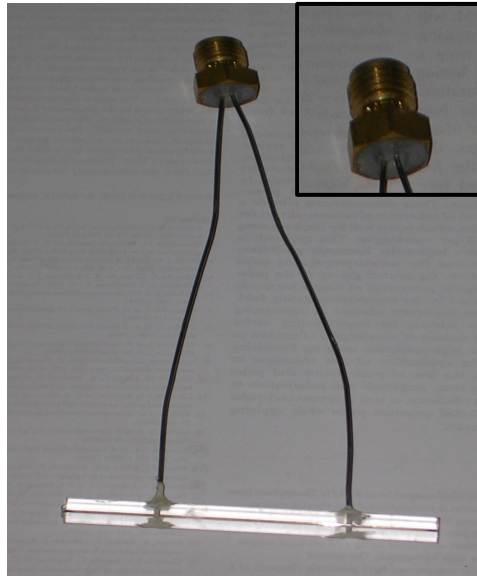
Figure A.4: Photo of the vacuum cell composed of glass capillary and steel tubes as gas inlets. The target gas is fed directly into the fiber via the two steel tubes. Inset: Close-up view of Swagelok cap.

Swagelok cap. The two holes are drilled with a 3/64" bit into a Swagelok 1/4" brass cap, shown in Fig. A.4 inset, through which steel tubes (.0355" OD and .023" ID) are soldered. If the rods become clogged, a #74 drill bit may be used to clean them out. The rods should be inserted only about 2 mm inside the glass capillary so they do not block light propagation through the fiber. This can be checked by shining a flashlight through the fiber. The other end of the hole in the capillary must also be sealed with the epoxy. Allow the epoxy to cure for 16-24 hours before putting under vacuum. Similar to the second version, the fiber/glass capillary is connected to the chamber by 1/4" Swagelok connections with Teflon ferrules. The fiber can be replaced by locally heating the Torr Seal seal between the steel rods and the capillary. This design is lightest of the three and can support any fiber length with the only requirement being that the differential pumping sections must be at least 1.5 cm to allow for the use of Swagelok connectors. Additionally, the laser light can be seen as it propagates along the fiber which can aide in
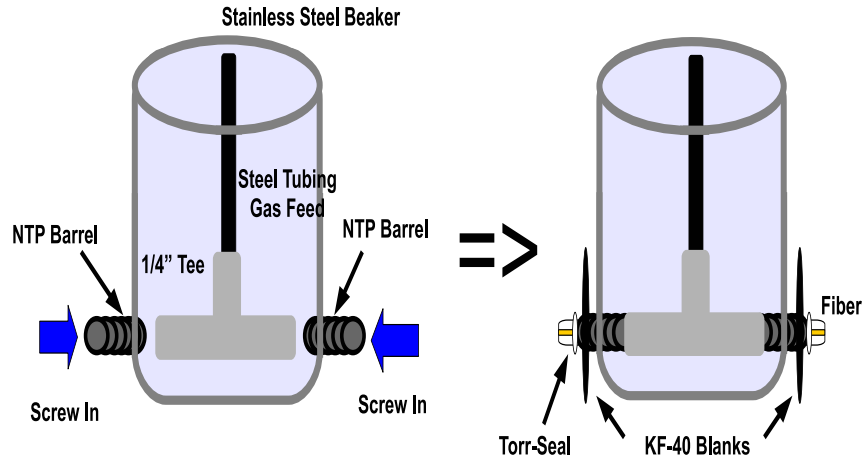
Figure A.5: Diagram of a procedure to construct a LN_2 cooled fiber. The gas inlet is connected to the tee; then the barrels are screwed through the beaker into the tee. Next, KF blanks are connected to the barrels and then the fiber waveguide is Torr Sealed to the barrels making a vacuum tight seal.

beam alignment, discussed further in Appendix B.

A.1.2 Liquid Nitrogen Cooled Fiber Vacuum Cell

In this section, the construction of the liquid nitrogen (LN_2) cooled fiber is detailed along with the procedure used to achieve and maintain the reduced temperature. First, the LN_2 bath is made from a 1-liter stainless steel beaker in which two 3/16" NPT threaded hole centered about 1.5 cm from the bottom of the beaker are tapped directly across from each other. The base for the fiber is a 3/16" NPT tee. First, the gas inlet is connected to the tee followed by NPT barrels that are wrapped in Teflon tape. The barrels are first screwed into the beaker then into the tee, as shown in Fig. A.5. Brass KF-40 blanks which are drilled and tapped with a 3/16" NPT holes are then screwed into the barrels on the outside of the beaker to connect the bath/cell to the rest of the vacuum chamber. Now the tee and its parts should be tight and should not move easily. If the parts do move, reconstruct the unit until it is tight. The fiber/capillary waveguide is placed gently into

Figure A.6: Photo of the liquid nitrogen cooled fiber housing. Note the styrofoam used from insulation.

the tee through the barrels. The capillary length must be at least 10.5 cm so that about 5 mm hangs over the barrel on each side. The fiber is then Torr Sealed to the barrels. Remember to make a smooth seal around the fiber and the barrels, as the Torr Seal bond needs to be vacuum tight. The fiber/cell is fairly sturdy, but torquing of the gas inlet can snap the fiber. Additionally, the exposed fiber ends are fragile and can be damaged.

The cell must be insulated during cooling. Stryofoam is wrapped around the outside of the beaker to reduce heat flow from the environment, Fig. A.6. Additionally, a hard stryofoam container can be placed over the beaker for additional insulation. Heating wire is wrapped around each of the KF-blanks and any of the exposed barrels outside the beaker. The heating wire is soldered to a 120 V plug. The voltage across the wire is controlled by a Variable Autotransformer (Variac). Typically, the Variac is set to 5-8% of the maximum output. Setting the output voltage any higher will burn out the wire. The heating wire transfers heat to the chamber walls outside the LN_2 bath to reduce condensation on the input windows. For cooling, the beaker is filled with LN_2. Once equilibrium is reached, the

beaker will only need to be refilled about once every 20 minutes to maintain temperature. The initial cooling causes a shift in the position of the fiber and thus some realignment of the laser beams are necessary. After this realignment, no additional alignment (outside of mis-alignment due to laser drift) is needed while maintaining the temperature.

Unfortunately, due to the design of this cell, the only way to change the fiber requires physically breaking the capillary. Removal is accomplished by unscrewing the barrels from the tee. The fiber will be damaged beyond repair and, thus, it is recommended that fiber changes only be done in the event of fiber damage.

Appendix B

Fiber Alignment

This section will address the technical aspects regarding the alignment of the beams through the fiber. Both configurations, collinear and counter-propagating, will be addressed along with some general information.

All alignment is first done with the harmonic generating beam. The basic optical components used in the beam alignment are a lens (typically with a focal length of 400 mm) on a 3-D translation stage and two mirrors (M1 and M2), seen in Fig. B.1. The initial alignment is conducted with the amplified spontaneous emission (ASE) from the laser amplifier which eliminates the potential for fiber damage due to high laser intensities. M1 and M2 are used to center the beam through the center of the lens and on the face of the fiber. The face of the fiber can be observed by the reflection off a mirror placed after the lens just outside the window to the chamber. The image is captured by a video camera. Do not look directly at the reflection as there is potential for eye injury even with the low intensity beam. The focus of the beam is evident in the video camera display as a bright white light. Then using M1 and the lens, the beam is coupled into the fiber. When the beam enters the fiber the intensity of the spot in the video image is decreased significantly. In either the glass cell or steel rod vacuum cell design, this coupling is also signified by a red glow illuminating the length of the fiber.
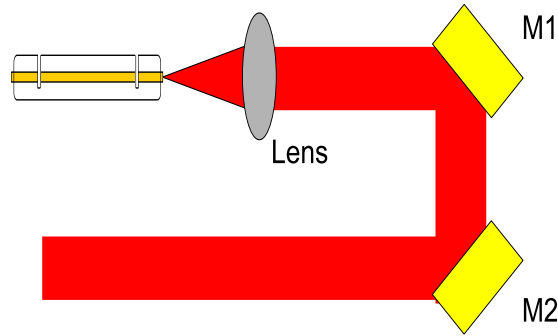
Figure B.1: Diagram of optical components used in beam alignment. M1 and the lens are primarily used for beam alignment while M2 is utilized in combination with M1 to center the beam on the lens.

Additionally, this initial coupling is seen on the exit of fiber. In the collinear configuration, the exit beam is picked off by a mirror on a manipulator that sends the beam out of the chamber through a glass window. At this stage, the exit beam is typically too weak to be measured by a power meter and must be imaged on a white card. The exit beam is faint and has a speckled structure. The beam alignment is improved by alternating between M1 and the lens until the beam image is a bright, uniform round spot.

A power meter can now be used to measure the coupling efficiency. Using the same M1/lens alignment scheme, the beam is walked to maximize the output beam energy. Adjustments to the lens position include movement along all three axes. The output energy is highly dependent on the distance between the lens and the face of the fiber (translational position of the focus). When the throughput energy is maximized, the location of the beam on the lens must be checked. It is desirable to have the beam pass through the middle of the lens to reduce aberrations. M2, the lens, and M1 can be walked alternatively to move the position of the beam on the lens while maintaining most of the throughput power. Additionally, the angle of the lens relative to the beam propagation direction should be adjusted at this time. The retro-reflection off the lens should propagate
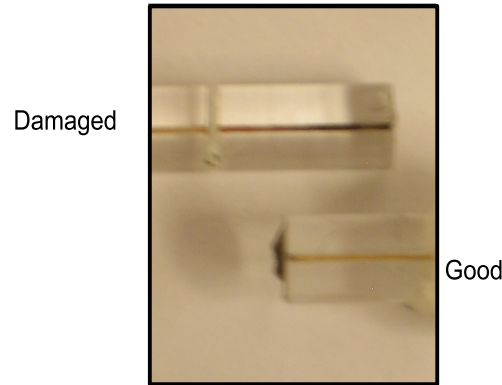
Figure B.2: Photo of damaged fiber. The damage is evident in the black fiber inside the differential pumping region (top fiber).

back along itself.

Afterward, repeat the M1/lens alignment to maximize output. The centering of the beam on the lens and the power alignment may need to be repeated several times until the maximum throughput is achieved when the beam is basically centered on the lens. At this point, the maximum coupling efficiency of the ASE is typically 65-75% and the output beam mode is circular.

Next, the laser is seeded and amplified light is sent into the fiber. The pulse energy should be no more than 300 mW at this stage. Typically, only slight adjustments to the lens position are needed to achieve maximum throughput, but the M1/lens alignment procedure may need to be implemented if the conversion efficiency is lower than 60-65%. If the coupling efficiency is low (< 50 %) and all of the alignment procedures have been implemented to no avail, the fiber may be damaged. If possible, remove capillary from vacuum chamber and analyze at the fiber ends. Damaged to the fiber is typically characterized by a blackening of the fiber that extends ∼2-4 mm inside the capillary (see Fig. B.2). Some blackening of the fiber end at the entrance and exit of the fiber will always exist, but the black fiber section does not appear inside the capillary unless the fiber is damaged. The rest of the alignment is done utilizing the lens and the harmonic signal.
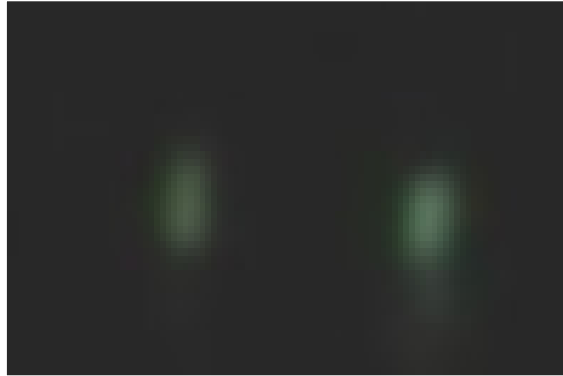
Figure B.3: Video image gives real time feedback of the harmonic signal.

There is an imaging system in the beam tube that connects the spectrometer to the CCD camera and images the phosphor screen onto the CCD camera. In addition, a small mirror may be inserted into a hole in the beam tube. This mirror is used for real-time monitoring of the harmonic emission with a video camera. The output of the camera is sent to a computer which can capture still images or stream the live video feed. A typical video image is shown in Figure B.3. At lower pulse energies, <100 mW in the fiber, the best experimental results were obtained when the beam was aligned to maximize the highest order harmonic visible on the real-time video image. This alignment is done by adjusting all three of the axes of the lens position. At higher pulse energies, spatial mode is more important due to the excitation of multiple fiber modes which can lead to a splitting of the harmonic intensities from a central circular mode into two vertically separated, high flux regions (seen in Fig. B.4 (a)). This splitting can also be seen in the video image. For the experiments discussed in this dissertation, the optimum results were obtained when the spatial mode was a single intense spot, resembling the EH_{11} mode, centered in the upper portion of the detector, Fig. B.4 (b).

While the previous portion of this appendix focused on the beam alignment of the harmonic generating pulse, the rest will discuss the procedures used to align the pump
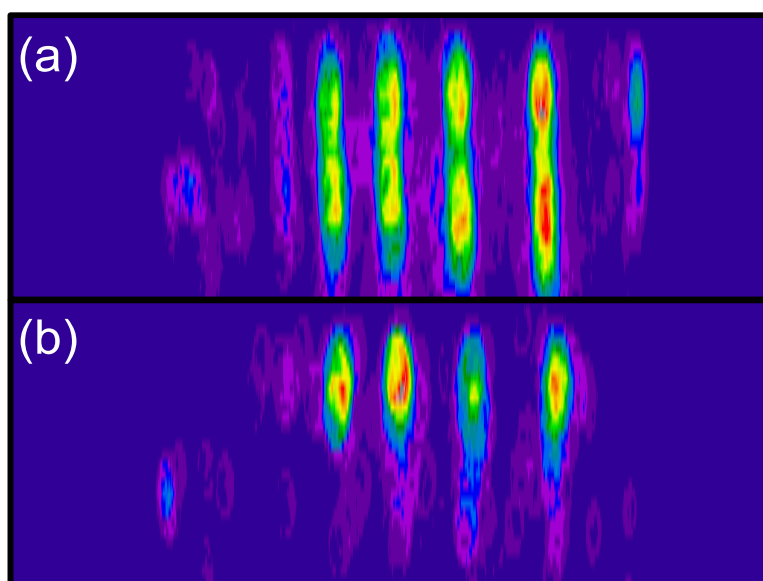
Figure B.4: CCD image of harmonic signal utilized for final beam alignment. (a) Harmonic image when the laser beam is slightly mis-alignment resulting in the excitation of multiple fiber modes. In this alignment, most molecular dynamics were not observed. (b) The harmonic signal produced by an optimally aligned beam.

beams. In a collinear configuration (see Fig. 3.1), even though the pump beam travels along the same path after the interferometer, slight mis-alignment can reduce or eliminate the degree of transient molecular alignment observed. To spatially overlap the pump and harmonic beams, set the relative delay to zero so that the interference fringes are visible. The pump arm of the interferometer should be adjusted until the interference pattern is mostly centered and, as the delay between the pulse is adjusted, the interference pattern resembles circles expanding outward (or contracting inward) from the center of the beam. The two beams should now both be optimally aligned.

The counter-propagating configuration contains two fundamentally identical sets of optical components, one for each beam. Therefore, the same procedure that is illustrated above for aligning the harmonic generating beam is used for the counter-propagating beam. Alternatively, the initial alignment may be aided by setting up apertures in the output harmonic beam. The initial alignment of the pump beam is then accomplished by overlapping the two beams through these apertures via adjustments to the optical components in the pump beam path. Since the beam does not produce harmonics, the final alignment is done using the coupling efficiency of the CP pulse and the output spatial mode of the harmonic pulse as guides. The coupling efficiency of the pump beam is maximized while matching its output spatial mode to the output mode of the harmonic generating beam. This procedure is imprecise and may require multiple iterations.